Maher Barkallah ·
Jean-Yves Choley · Jamel Louati ·
Omar Ayadi · Fakher Chaari ·
Mohamed Haddar *Editors*

Mechatronics 4.0

Proceedings of the First International
Workshop on Mechatronics 4.0, June
8–9, 2019, Mahdia, Tunisia

🌣 Springer

Lecture Notes in Mechanical Engineering

Lecture Notes in Mechanical Engineering (LNME) publishes the latest developments in Mechanical Engineering—quickly, informally and with high quality. Original research reported in proceedings and post-proceedings represents the core of LNME. Volumes published in LNME embrace all aspects, subfields and new challenges of mechanical engineering. Topics in the series include:

- Engineering Design
- Machinery and Machine Elements
- Mechanical Structures and Stress Analysis
- Automotive Engineering
- Engine Technology
- Aerospace Technology and Astronautics
- Nanotechnology and Microengineering
- Control, Robotics, Mechatronics
- MEMS
- Theoretical and Applied Mechanics
- Dynamical Systems, Control
- Fluid Mechanics
- Engineering Thermodynamics, Heat and Mass Transfer
- Manufacturing
- Precision Engineering, Instrumentation, Measurement
- Materials Engineering
- Tribology and Surface Technology

To submit a proposal or request further information, please contact the Springer Editor in your country:

China: Dr. Mengchu Huang at mengchu.huang@springer.com
India: Priya Vyas at priya.vyas@springer.com
Rest of Asia, Australia, New Zealand: Swati Meherishi at swati.meherishi@springer.com
All other countries: Dr. Leontina Di Cecco at Leontina.dicecco@springer.com

To submit a proposal for a monograph, please check our Springer Tracts in Mechanical Engineering at http://www.springer.com/series/11693 or contact Leontina.dicecco@springer.com

Indexed by SCOPUS. The books of the series are submitted for indexing to Web of Science.

More information about this series at http://www.springer.com/series/11236

Maher Barkallah · Jean-Yves Choley ·
Jamel Louati · Omar Ayadi ·
Fakher Chaari · Mohamed Haddar
Editors

Mechatronics 4.0

Proceedings of the First International
Workshop on Mechatronics 4.0, June 8–9,
2019, Mahdia, Tunisia

Editors
Maher Barkallah
National School of Engineers of Sfax
Sfax, Tunisia

Jamel Louati
National School of Engineers of Sfax
Sfax, Tunisia

Fakher Chaari
National School of Engineers of Sfax
Sfax, Tunisia

Jean-Yves Choley
Institut Supérieur de
Mécanique–SUPMECA
Saint-Ouen, France

Omar Ayadi
National School of Engineers of Sfax
Sfax, Tunisia

Mohamed Haddar
National School of Engineers of Sfax
Sfax, Tunisia

Preface

Mechatronics is a dual concept referring both to an integrative and innovative technology and a synergetic and collaborative design methodology merging multiple engineering domains. This, mechatronics, is also a key interface between physical, cyber and human spaces.

For all these reasons, mechatronics is at the heart of Industry 4.0 concepts. Indeed, this discipline provides scientific and industrial actors with means to design, produce, integrate and operate autonomous robots, cyber-physical production systems (CPPS) with relevant industrial Internet-of-Things (IoT), smart actuators and sensors, monitoring and control systems with diagnostic capacities, etc.

It also provides designers with methodologies and modeling tools and languages for a consistent and efficient model-based engineering of all those key technologies needed for the Industry 4.0 concepts implementation.

This book is a compilation of 15 selected peer-reviewed papers from the International Workshop on Mechatronics 4.0 in its first edition held from June 8 to 9, 2019, in Mahdia, Tunisia. It was organized jointly by the Laboratory of Mechanics, Modelling and Production (LA2MP) of the National School of Engineers of Sfax (ENIS), Tunisia, and the QUARTZ Laboratory from Higher Institute of Mechanics in Paris, SUPMECA, France.

The International Workshop was focused on the latest advances in mechatronics and multiphysics systems design and modeling in the era of Industry 4.0. It was the occasion to discuss and exchange new ideas and present the results of current research activities in the field. The topics that were discussed and have been covered by chapters selected for this book include: theoretical foundations of mechatronics; mechatronics for Industry 4.0 and cyber-physical systems; and design, modeling and diagnostics of mechatronics systems.

The editors would like to thank Springer for the opportunity to publish the proceedings of this workshop.

Mahdia, Tunisia   Maher Barkallah
June 2019   Jean-Yves Choley
                                                                     Jamel Louati
                                                                     Omar Ayadi
                                                                   Fakher Chaari
                                                                Mohamed Haddar

Contents

Maintenance 4.0 of Wind Turbine

Ahmed Hammami, Fathi Djemal, Atef Hmida, Fakher Chaari, and Mohamed Haddar

Abstract Energy production through Wind turbine installations is increasing fast. In fact, wind turbines become bigger in size and power, what incurs that a simple unit defect causes huge energy losses. They are running in severe conditions of speed and load due to the variation of the wind speed. In addition, Wind turbines are subject to the environmental conditions such as wind shear, turbulence, gusts, rain, snow, sand and sea for offshore wind turbines. For this, their diagnoses and their follow-up is a priority to avoid the stops of production. In, developing techniques for prognostic and remaining useful life estimation is a very urgent necessity in wind turbine maintenance. Maintenance 4.0 is smart maintenance which refers to the last industrial revolution "Industry 4.0": It proposes strategies to meet these expectations by implementing advanced monitoring techniques through highly developed instruments and real-time signal processing techniques and by building models based on algorithm that will ensure a self- improvement and optimize the failure prediction. In this paper, a process of the predictive maintenance 4.0 is proposed and applied to a wind turbine in order to optimize operating costs and improve the energy efficiency of this system. In fact, dynamic, thermal and material information which are extracted from sensors are combined and characterized in the real time for a global process monitoring.

A. Hammami (✉) · F. Djemal · A. Hmida · F. Chaari · M. Haddar
Laboratory of Mechanics, Modeling and Production (LA2MP), National School of Engineers of Sfax, BP1173, 3038 Sfax, Tunisia
e-mail: ahmed.hammami2109@gmail.com

F. Djemal
e-mail: fathidjemal@yahoo.fr

A. Hmida
e-mail: abdallahatef@yahoo.fr

F. Chaari
e-mail: fakher.chaari@gmail.com

M. Haddar
e-mail: mohamed.haddar@enis.rnu.tn

A. Hammami
Department of Mechanical Engineering, National School of Engineers of Gabes, Omar ibn el Khattab Road, 6029 Gabès, Tunisia

1 Introduction

The wind turbines are frequently built as wind farm. They can have several faults that can cause failures with different levels of severity (Ziane 2017). Since their maintenance work is very hard task, many researchers focused on wind turbine in order to understand its dynamic behavior (Srikanth and Sekhar 2016; Tounsi et al. 2016), to improve their reliability (Musial et al. 2007) and efficiency, to develop their maintenance, to reduce their operating costs and to improve their running life. In fact, Marquez et al. (2012) achieved a state of the art of the strategies of maintenance and they presented the different used methods and techniques in the condition monitoring and signal processing of wind turbines. In addition, Marquez et al. (2016) used a quantitative method called Fault Tree Analysis (FTA) to identify the critical components of wind turbines. This method is computed through the Binary Decision Diagram (BDD) in order to reduce the computational costs. They applied the FTA method on four groups of elements of wind turbine: the tower, the blade system, the electrical components and the power drive train which is very sensitive to the variable speed and load running conditions (Hammami et al. 2015a). So, it is essential to identify the modal properties (Hammami et al. 2015b; Mbarek et al. 2018; Hmida et al. 2019) of the drive train especially in the non stationary conditions (Mbarek et al. 2019). The drive train can present inevitable defects and its diagnostic is not evident since the wind turbine is running in non-stationary conditions (Zhang et al. 2012; Dempsey and Sheng 2013; Sawalhi et al. 2014 Yang et al. 2016; Hammami et al. 2019). Wind turbine drive train is the most critical and expensive group of components of wind turbine (Leite et al. 2018) and it is also sensitive to the implementation conditions such as the offshore floating plate form (Viadero et al. 2014). Recently, many researchers focused on the prognostic and performance degradation of rotary machinery systems (Lee et al. 2014; Fourati et al. 2017; Derbel et al. 2019) and specially the drive train of wind turbines: Pan et al. (2019) used an approach the empirical Mode Decomposition called CEEMDAN and the Kernal Principal Component Analysis in order to evaluate the performance degradation of WT gearbox and to predict the Remaining Use Life which is computed through the Extreme Learning Machine.

Research on wind turbine blade is also very attractive. Not only design, exploring and performance of blade system receive an increasing amount of attention (Hayat et al. 2019; Hua et al. 2019; Ansari et al. 2019), but also many studies on fatigue and failure of blades are carried out (Jensen et al. 2006; van Leeuwen et al. 2002; Griffin and Zuteck 2001): Mishnaevsky (2019) summarized the repairing techniques of wind turbine blade and developed new ideas for maintenance blades.

According to the cited research studies, wind turbine is a very complex system and it needs an intelligent maintenance. For this purpose, we call on maintenance

4.0 which refers to the last industrial revolution "Industry 4.0". In this paper, the maintenance 4.0 is defined in Sect. 2 where the implementation approach is described. In Sect. 3, maintenance 4.0 approach is applied on the case of wind turbine.

2 Definition of Maintenance 4.0

Maintenance 4.0 refers to the last industrial revolution "Industry 4.0" where smart companies, which operate through lean manufacturing strategies and which enable humans and robots to communicate more easily, are equipped with the smart machines and tools in order to take advantage of better decisions and self-development.

2.1 Maintenance Evolution

The predictive maintenance is always evolving. Four levels of predictive maintenance can be found (Fig. 1).

It has been years since we applied the first level of predictive maintenance by carrying out the visual inspection in the daily rounds.

In the second level, instrumentation and advanced techniques such as thermography, vibration analyses are used and we can make the comparison with the old measurements.
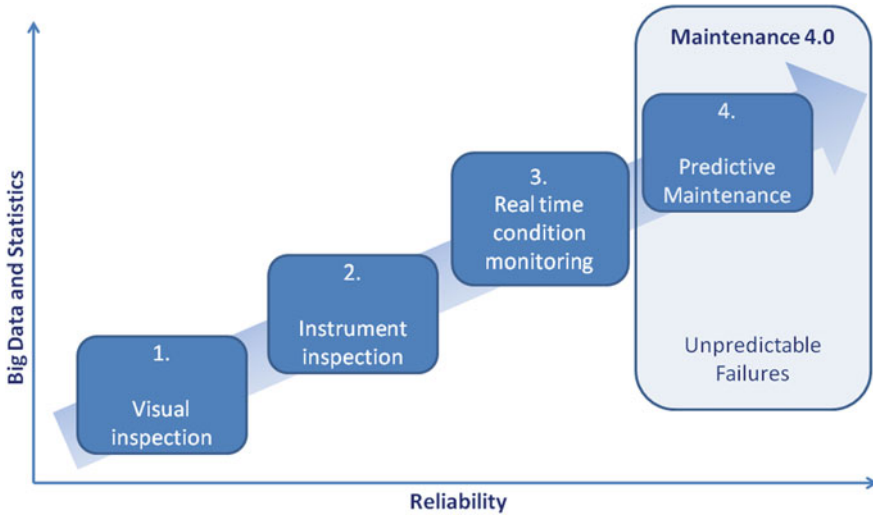
Fig. 1 Predictive maintenance evolution (Haarman et al 2017)

In the 3rd level, the measurements are permanent. So, we have finer means in monitoring the state of the machine and its degradation.

The 4th level corresponds to the maintenance 4.0, it is the proactive or predictive maintenance where we will work with the big data and the more sophisticated analysis techniques of the statistics type and the Learning machines. So, we will build models based on algorithm that will ensure a self-improvement.

2.2 *Predictive Maintenance 4.0*

The predictive maintenance 4.0 can be defined by the ability to predict potential failures or failures of an installation and describe the preventive actions of corrections using data analysis techniques. These data are of several orders and of several sources such as the technical state of the installations, operating machine condition, the evolution of the environment of the installation (dust, temperature, humidity …).

The maintenance history can also be used using Computerized Maintenance Management System software (maintenance tasks and preventive maintenance). We can use big data especially when it comes to installations that are similar (for example wind turbine farm) where can compare and increase the volume of data. And more than we have to give more than the algorithms will be optimized.

2.3 *Implementation Approach of Maintenance 4.0*

The implementation of this approach is proposed by Haarman et al. (2017) and it is shown in Fig. 2.

Maintenance 4.0 requires seven steps: the first and the second steps which are *Asset value ranking and feasibility study* and *Asset selection* can be done together and at the same time. Maintenance 4.0 approach is based on the creation of value. So, it is necessary to understand the functioning of machine and the parts of installation more penalizing and not necessarily those which have the most information. Reliability study is carried out on third step "*Reliability modeling*" and the fourth step "*Algorithm design*" through the proposal of a mathematical model and the creation of a corresponding algorithm. Then, tests are carried out on the fifth step "*Real time performance monitoring*", the saved data are integrated into the model to refine and link with the preventive ranges on the sixth step "*Failure prediction*" and seventh step "*Preventive task prescription*".

To do this, we need a whole series of data. So, we need to make our selection of conventional indicators. Some data is structured in the CMMS and some that are not structured.

It is important to optimize regularly the algorithm through Machine Learning and to have links with what we know and what we observe in order to predict the default and prescribe actions before suffering the effects of failure.
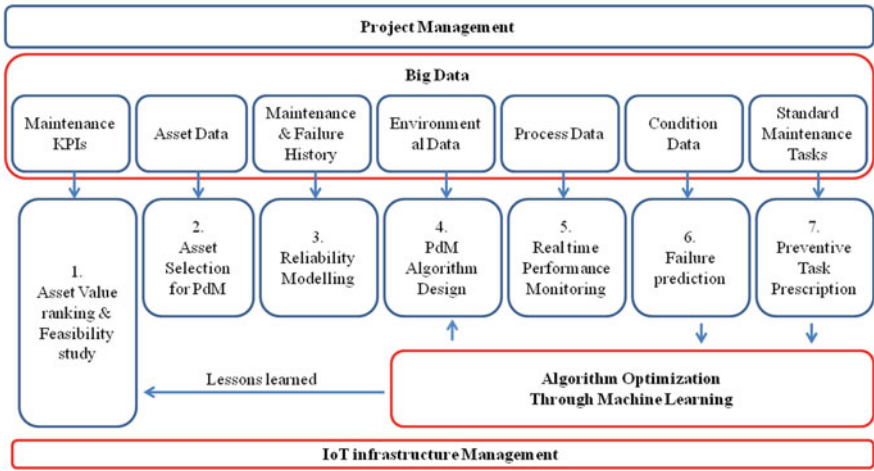
Fig. 2 Implementation approach of maintenance 4.0 (Haarman et al. 2017)

So, we have to manage this approach in order to arrive on the one hand to set up infrastructure IOT (Internet Of Things) and on the other hand up date of organization.

3 Case Study: Maintenance 4.0 of Wind Turbine

The case of wind turbines is selected to illustrate the implementation approach of maintenance 4.0 since they are building as wind farm and their maintenance is hard.

3.1 Identification of Critical Components of Wind Turbine

The first two steps of maintenance 4.0 which are *Asset value ranking and feasibility study* and *Asset selection* are applied in this subsection.

In fact, the wind turbine can be divided into four groups of components: the foundation and tower, blades system, electrical components and the power train including shafts, bearings and gearbox.

The Fault Tree Analysis can be applied on each group in order to identify the critical components (Marquez et al. 2016).

3.2 Instrumentation and Condition Monitoring of Wind Turbine

Instrumentation of wind turbine is preparing to the fifth step of maintenance 4.0 "*Real time performance monitoring*". Many techniques of condition monitoring can be used in the case of wind turbines. Vibration analysis is the most used techniques especially for rotating components. In fact, monitoring of gearbox and bearings through this technique is very common. In addition, vibration analysis can be adapted to the monitoring of rotor, blades and tower. Nerveless, these components can be protecting against the high stress through the strain measurement. The control of generator can be performed like other electrical equipment through voltage and current analysis (Feki et al. 2012, 2013). We can found other techniques of condition monitoring such as acoustic emission, radiographic inspection and thermography of blades, oil analysis of gearbox. Since the condition monitoring should be performing and in real time, it is better to use the vibration analysis for the gearbox, bearings and the tower, the stator current analysis for the generator and the strain measurement for the blades (Schröder et al. 2005). To carry out test, accelerometers are mounted on the bearing, gearbox and the tower; strain gauges are mounted on the blades and current sensors are mounted to measure the stator current (Fig. 3).

3.3 Prognostic and Health Management of Wind Turbine

This subsection covers four steps which are on the one hand the third and the fourth steps "*Reliability modeling*" and "*Algorithm design*" and on the other hand the sixth and the seventh steps "*Failure prediction*" and "*Preventive task prescription*".

In fact, steps "*Reliability modeling*" and "*Algorithm design*" are carried out together. As an example, Pan et al. (2019) applied these two steps on vibratory signals of wind turbine gearbox to predict its Remaining Use Life (RUL). They performed a highly accelerated life test and they employed the Extreme Learning Machine (ELM) and fruit Fly Of Algorithm (FOA) which is proposed by Ye et al. (2015). This algorithm is applied after de-noising the vibratory signals and extracting the health indicator through an approach of Empirical Mode Decomposition (EMD) called Complete Ensemble EMD with Adaptive Noise (CEEMDAN) and Kernel Principal Component Analysis (KPCA). In fact, the evolution of the health indicator as shown in Fig. 4 can be divided into three time-periods: run in, stable and wear.

The comparison between the real RUL and the predicted RUL at the wear period (Fig. 5) proves the supremacy of the used algorithm.

In addition, this algorithm allows the seventh step "*Failure prediction*" because they (Pan et al. 2019) predict debris damage happened to the low-speed stage bearing, the ring gear and the oil filter.
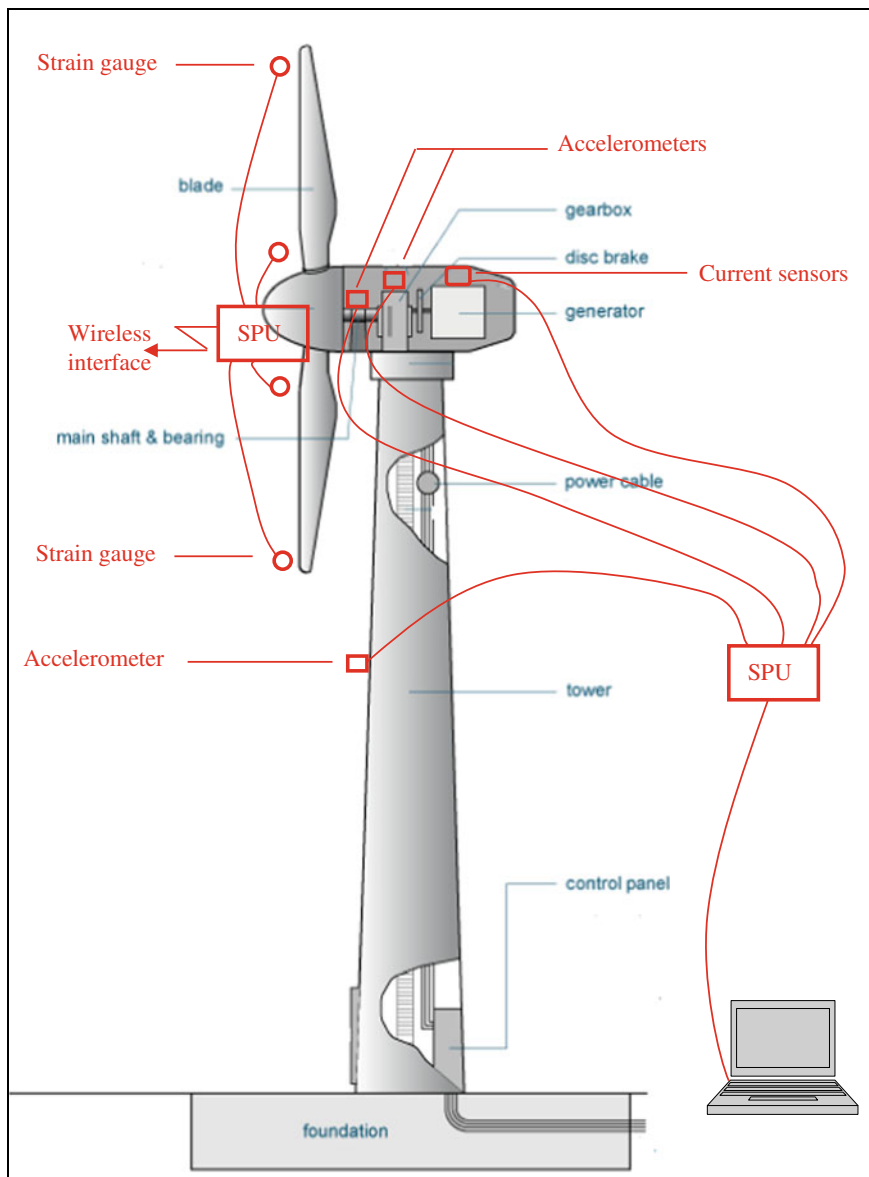
Fig. 3 Instrumentation of wind turbine
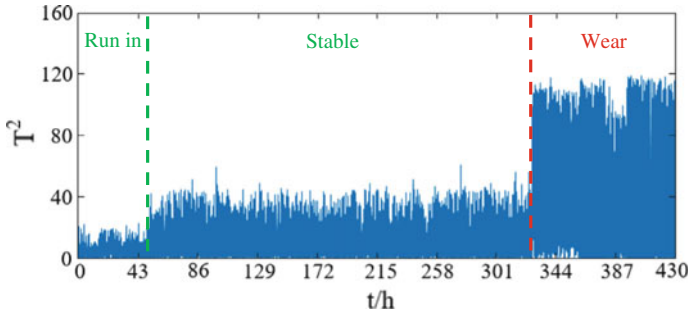
Fig. 4 Health indicator (Pan et al. 2019)

Fig. 5 RUL prediction model based on FOA-ELM algorithm (Pan et al. 2019)
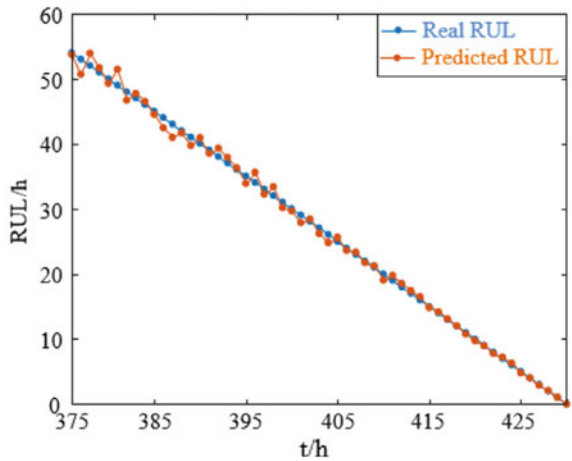
4   Conclusion

Maintenance 4.0 is a smart maintenance and it can be applied on wind farm where wind turbines are comparable installations and they are running in the same conditions. So, Big data can be used to predict failure by applying Learning Machine Algorithm to predict failure. Extreme learning machine (ELM) optimized by fruit fly of algorithm (FOA) is an effective algorithm for RUL prediction.

To carry out this, strain gauges, current sensors and accelerometers should be mounted respectively on the blades, alternator and rotating components (gearbox, bearing and tower). The measurements should be in real time and the extracted signals are processed to be used by a learning machine for failure prediction.

References

Ansari M, Nobari MRH, Amani E (2019) Determination of pitch angles and wind speeds ranges to improve wind turbine performance when using blade tip plates. Renew Energy 140:957–969

Dempsey PJ, Sheng S (2013) Investigation of data fusion applied to health monitoring of wind turbine drivetrain components. Wind Energy 16:479–489

Derbel S, Feki N, Barbot JP, Nicolau F, Abbes MS, Haddar M (2019) Electro-mechanical system control based on observers, in advances in acoustics and vibration II. Appl Condition Monit 13:101–110

Feki N, Clerc G, Velex P (2012) An integrated electro-mechanical model of motor-gear units—applications to tooth fault detection by electric measurements. Mech Syst Signal Process 29:377–390

Feki N, Clerc G, Velex P (2013) Gear and motor fault modeling and detection based on motor current analysis. Electr Power Syst Res 95:28–37

Fourati A, Bourdon A, Feki N, Rémond D, Chaari F, Haddar M (2017) Angular-based modeling of induction motors for monitoring. J Sound Vib 395:371–392

Griffin DA, Zuteck MD (2001) Scaling of composite wind turbine blades for rotors of 80 to 120 m diameter. J Sol Energy Eng 123(4):310–318

Hammami A, Fernandez A, Viadero F, Chaari F, Haddar M (2015a) Modal analysis of back-to-back planetary gear: experiments and correlation against lumped-parameter model. J Theor Appl Mech 53(1):125–138

Hammami A, Fernandez A, Viadero F, Chaari F, Haddar M (2015b) Dynamic behaviour of back to back planetary gear in run up and run down transient regimes. J Mech 31(4):481–491

Hammami A, Hmida A, Chaari F, Khabou MT, Haddar M (2019) Effect of cracked tooth on the dynamic response of simple gearbox with flexible coupling for acyclism operation. J Theor Appl Mech 53(3):591–603

Haarman M, Mulders M, Vassiliadis C (2017) Predictive maintenance 4.0, Mainnovation

Hayat I, Chatterjee T, Liu H, Peet YT, Chamorro LP (2019) Exploring wind farms with alternating two- and three-bladed wind turbines. Renew Energy 138:764–774

Hmida A, Hammami A, Khabou MT, Chaari F, Haddar M (2019) Effect of elastic coupling on the modal characteristics of spur gearbox system. Appl Acoust 144:71–84

Hua X, Zhang C, Wei J, Hu X, Wei H (2019) Wind turbine bionic blade design and performance analysis. J Vis Commun Image Represent 60:258–265

Jensen FM, Falzon BG, Ankersen J, Stang H (2006) Structural testing and numerical simulation of a 34 m composite wind turbine blade. Compos Struct 76:52–61

Lee J, Wu F, Zhao W, Ghaffari M, Siegel D, Liao L (2014) Prognostics and health management design for rotary machinery systems—Reviews, methodology and applications. Mech Syst Signal Process 42:314–334

Leite GNP, Araújo AM, Rosas PAC (2018) Prognostic techniques applied to maintenance of wind turbines: a concise and specific review. Renew Sustain Energy Rev 81:1917–1925

Marquez FPG, Tobias AM, Perez JMP, Papaelias M (2012) Condition monitoring of wind turbines: techniques and methods. Renew Energy 46:169–178

Marquez FPG, Perez JMP, Zarugan AP, Papaelias M (2016) Identification of critical components of wind turbines using FTA over the time. Renew Energy 87:869–883

Mbarek A, Fernandez A, Hammami A, Iglesias M, Chaari F, Viadero F, Haddar M (2018) Comparison of experimental and operational modal analysis on a back to back planetary gear. Mech Mach Theory 124:226–247

Mbarek A, Hammami A, Fernandez A, Chaari F, Viadero F, Haddar M (2019) Effect of load and meshing stiffness variation on modal properties of planetary gear. Appl Acoust 147:32–43

Mishnaevsky JL (2019) Repair of wind turbine blades: Review of methods and related computational mechanics problems. Renew Energy 140:828–839

Musial W, Butterfield S, McNiff B (2007) Improving wind turbine gearbox reliability. In: European wind energy conference Milan, Italy

Pan Y, Hong R, Chen J, Singh J, Jia X (2019) Performance degradation assessment of a wind turbine gearbox based on multi-sensor data fusion. Mech Mach Theory 137:509–526

Sawalhi N, Randall RB, Forrester D (2014) Separation and enhancement of gear and bearing signals for the diagnosis of wind turbine transmission systems. Wind Energy 17:729–743

Schröder K, Apitz J, Ecke W, Lembke E, Lenschow G (2005) Fibre Bragg grating sensor system monitors operational load in a wind turbine rotor blade. Proc SPIE 5855:270–273

Srikanth P, Sekhar AS (2016) Wind turbine drive train dynamic characterization using vibration and torque signals. Mech Mach Theory 98:2–20

Tounsi M, Beyaoui M, Abboudi K, Feki N, Walha L, Haddar M (2016) Influence of uncertainty in aerodynamic performance on the dynamic response of a two stage gear system. J Theor Appl Mech 54(2):601–612

van Leeuwen H, van Delft D, Heijdra J, Braam H, Jorgensen ER, Lekou D, Vionis P (2002) Comparing fatigue strength from full scale blade tests with coupon-based predictions. J Sol Energy Eng Trans ASME 124:404–411

Viadero F, Fernández A, Iglesias M, de-Juan A, Liaño E, Serna MA (2014) Non-stationary dynamic analysis of a wind turbine power drivetrain: Offshore considerations. Appl Acoust 77:204–211

Yang D, Li H, Hu Y, Zhao J, Xiao H, Lan Y (2016) Vibration condition monitoring system for wind turbine bearings based on noise suppression with multi-point data fusion. Renew Energy 92:104–116

Ye Q, Pan H, Liu C (2015) Enhancement of ELM by clustering discrimination manifold regularization and multiobjective FOA FOR semisupervised classification. Comput Intell Neurosci, ID 731494:1–9

Zhang Z, Verma A, Kusiak A (2012) Fault analysis and condition monitoring of the wind turbine gearbox. IEEE Trans Energy Convers 27(2):526–535

Ziane K (2017) Analysis, assessment and risk reduction of a wind farm. Dissertation, University of Oran 2, Algeria

An Analytical Approach to Model-Based Parametric Design of Mechatronic Systems with Modelica: A Case Study

Ghazoi Hamza, Maher Barkallah, Moncef Hammadi, Jean-Yves Choley, Jamel Louati, Alain Riviere, and Mohamed Haddar

Abstract Parametric study is a crucial step in the design process of a mechatronic system. In fact, it helps designers to describe the model parameters, the physical phenomena and to modify the design parameters to reach more satisfactory results in the predesign phase. The main idea of this paper is to develop a novel pre-designing approach to perform parametric studies concerning complex interactions among the different internal components of a system. In this paper, we are interested only in the vibration constraint between the different components embedded in a mechatronic system. To illustrate our approach, we used a specific case study: the vibration interaction between a dynamic excitation and a flexible beam as a support structure, having simply supported boundary conditions is investigated. The position of the perturbation source over the beam is parametrized and the feedback effect between components is taken into consideration. Our methodology is based on a pure analytical approach with Modelica/Dymola as an object oriented modeling language. This model can help designers to perform a parametric study and to examine the

G. Hamza (✉) · M. Barkallah · J. Louati · M. Haddar
Mechanics Modeling and Production Research Laboratory (LA2MP), National School of
Engineers of Sfax (ENIS), B.P. 1173, 3038 Sfax, Tunisia
e-mail: hamza.ghazoi@gmail.com

M. Barkallah
e-mail: bark_maher@yahoo.fr

J. Louati
e-mail: louati.ttg@gnet.tn

M. Haddar
e-mail: mohamed.haddar@enis.rnu.tn

M. Hammadi · J.-Y. Choley · A. Riviere
QUARTZ EA 7393, SUPMECA, 3 rue Fernand Hainaut, 93407 Saint-Ouen Cedex, France
e-mail: moncef.hammadi@supmeca.fr

J.-Y. Choley
e-mail: jean-yves.choley@supmeca.fr

A. Riviere
e-mail: alain.riviere@supmeca.fr

impact of the design variables on the mechatronic system response at an early stage of design. Object-oriented approach is used to produce a reusable component-based architecture.

1   Introduction

Mechatronic system is based on the close interaction of mechanical and electronic components. It exhibits both discrete and continuous dynamic behaviors, which can all be defined by systems of differential algebraic equations representing the exchange of signals, energy or other continuous entities between system devices (Zheng et al. 2016; Hammadi and Choley 2015; Hamza et al. 2015).

Mechatronic systems are facing several physical constraints like vibration and temperature, thus interaction phenomena between components becomes emergent at the system level.

Disturbance may cause several problems induced by vibration like as structural degradation and failure, malfunction of components, noise transmission, human dis-comfort and different other problems (Hamza et al. 2017). Therefore, it might be of important to decrease vibration from a certain part of the structure more than the other. Furthermore, the vibration existence in some structures which contain sen-sitive elements such as electronics cards may weaken their performance (Buchacz 2008; Veprik 2003).

A novel pre-dimensioning approach to investigate the vibrational aspects of a multibody system has been proposed in the previous works (Hamza et al. 2015b). In fact, the vibration interaction between electronic cards and motors has been studied. The location of these components is on a flexible continuous structure. Components positions over the support structure are parametrized. We assumed that motor creates perturbation over a well-defined rectangular area of the plate. To model the electronic card, a rigid mass mounted fixed on the plate is considered.

The influence of boundary conditions on the system's response is investigated in (Hamza et al. 2018b). In this research work, clamped–clamped (C-C) and sim-ply supported–simply supported (S-S) configurations are investigated. to build a reusable component-based architecture, object-oriented approach is implemented. This methodology supports system designers to define concepts and solutions.

Beam type structures are often used in machinery industries and steel construction. Several engineering problems can be modelled as simple degree of freedom system (sdof)-beam copled system, like as the case of an engine or electric motor mounted elastically on a structure (a beam or a plate). The literature concerned is abundant (Tang et al. 2008; Wu and Chen 2000; Inceao and Gürgöze 2001). There are many approaches which are used in order to study this kind of problems such as the assumed mode methods, Laplace transform, Lagrange's multipliers, numerical and analytical combined method and even a pure analytical solution for simple cases. For example,

Tang et al. (2008) studied the vibration transmission in a coupled system including of a sdof system and a beam using on the recurrence equation approach. The parametric analysis of this system was discussed in this work.

In this paper, new mechatronic system predesign methodology is presented. To achieve this, parametric models are developed in Modelica/Dymola. The organization of this paper is as follows. A short presentation of the analytical development of the problem is shown in Sect. 2. Section 3 describes the modeling of the system. Some results are presented in Sect. 4. The last section summarizes and concludes the paper.

2 Analytic Formulation of the Beam Vibration

This section presents the theory of determining the "steady" response amplitude of a beam carrying a concentrated element, considering the feedback effect based on an analytical method.

The system Fig. 1 consists of a spring–damper–mass system. Simply mounted on beam at position x = a.

The mass block is subjected to a harmonic excitation $Fe^{-j\omega t}$ is applied to the mass block, where m, k and c are the mass, stiffness and damping coefficient of the sdof system. The beam has a uniform structure with a constant rectangular cross-section (Tang et al. 2008).

The vibration equation governing the beam transverse motion is the following (Tang et al. 2008):

$$EJ \frac{\partial^4 w(x,t)}{\partial x^4} + \rho S \frac{\partial^2 w(x,t)}{\partial t^2} = Fe^{-j\omega t} \delta(x-a) \tag{1}$$
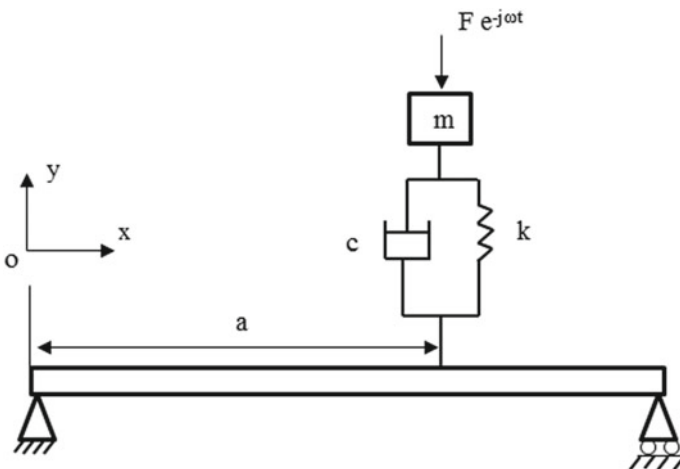
Fig. 1 Schematic representation of a coupled beam-sdof system

In this equation E, S, ρ and J are respectively, the Young's modulus, the beam cross-sectional area, constant density of the beam material and the moment of inertia. x is the spatial coordinate t is the time and δ represents the Dirac–delta function.

$W(x, t)$ denotes the beam transverse deflection (displacement), L is the beam length. The Euler–Bernoulli beam model was assumed which the effects of rotary inertia and shear deformation are neglected.

The natural frequency of the beam without the sdof system is:

$$\omega_n = n^2 \pi^2 / L^2 \sqrt{EJ/\rho S} \tag{2}$$

The beam boundary conditions are the following:

$$w(0, t) = w(L, t) = 0, \; \frac{\partial^2 w(0, t)}{\partial^2 x} = \frac{\partial^2 w(L, t)}{\partial^2 x} = 0 \tag{3}$$

Assuming,

$$w(x, t) = w(x)e^{-j\omega t} \tag{4}$$

The analytical solution of transverse amplitude for a simply supported beam carrying a sdof system, in the steady–state situation, is (Tang et al. 2008):

$$w(x) = \frac{FH/(1 - GD)}{c^2\omega^2 + (k - m\omega^2)^2} \frac{-2}{\rho SL} \sum_{n=1}^{\infty} \frac{\sin(n\pi a/L)\sin(n\pi x/L)}{\omega^2 - \omega_n^2} \tag{5}$$

where,

$$D = \frac{1}{c^2\omega^2 + \left(k - m\omega^2\right)^2} \frac{-2}{\rho AL} \sum_{n=1}^{\infty} \frac{\sin^2(n\pi a/L)}{\omega^2 - \omega_n^2} \tag{6}$$

$$G = k^2 m\omega^2 + c^2 m\omega^4 - km^2\omega^4 + jcm^2\omega^5 \tag{7}$$

and,

$$H = k^2 + c^2\omega^2 - km\omega^2 + jcm\omega^3 \tag{8}$$

3 Modelica System Modeling

Modelica as an object oriented free language has been considered to implement the analytical models developed above. The system is composed of a set of particular connected entities Fig. 2. We have developed in Modelica a new component called "*flexible beam*". The component has been implemented with a connector which is of *Flange* type; makes the element compatible with components, belong to the Modelica translational library (Modelica library to model one dimensional mechanical system).

The perturbation source is represented by a sdof system linked to the beam. to model the excitation source, Modelica Components library are used (the linear 1D model composed of a damper and spring in parallel and a sliding mass). The mass is subjected to a harmonic force. A sensor is used to measure the motion of the mass with respect the beam structure.

The position of the dynamic exciter over the beam is parametrized. Thus, the user can select the location as well as the model characteristics (mass of the sliding mass, dumping coefficient and spring constant).
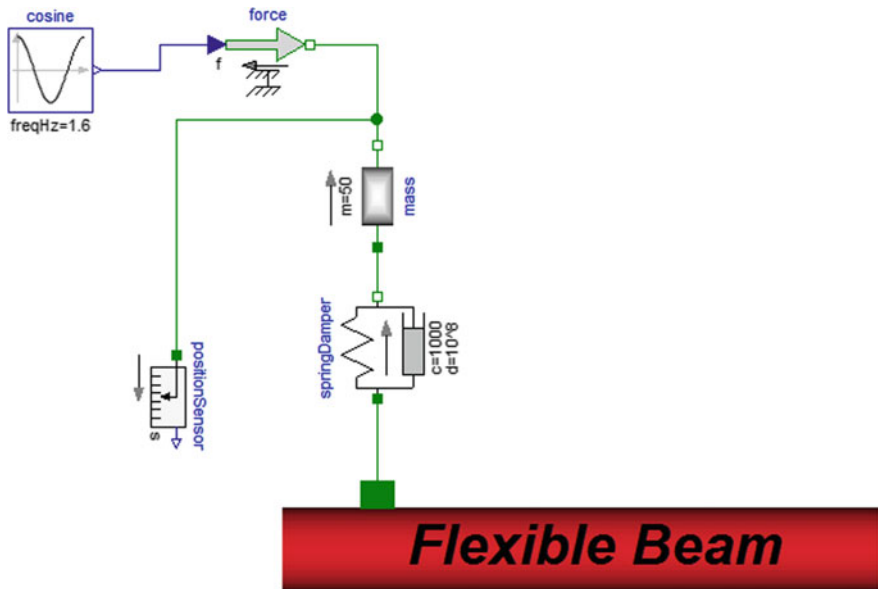
Fig. 2 Model of the system developed in Modelica/Dymola

4   Results and Discussion

After the multibody system modeling in Modelica, an analysis has been performed. The system design parameters have been listed in Table 1. Some simulation tests were carried out.

Figure 3 displays the displacements for two different points are plotted against time t where as the perturbation source is located at the mid span of the support

Table 1 Simulation parameters

Parameters	Value
Beam length	$l = 5$ m
Density of the beam material	$\rho = 7850$ kg/m^3
Young's modulus	$E = 2{,}10{,}000$ MPa
Force amplitude	$F = 10^6$ N
Damping coefficient	$c = 10^3$ N s/m
Stiffness coefficient	$k = 10^8$ N/m
Applied excitation frequency	$\omega = 10$ rad/s
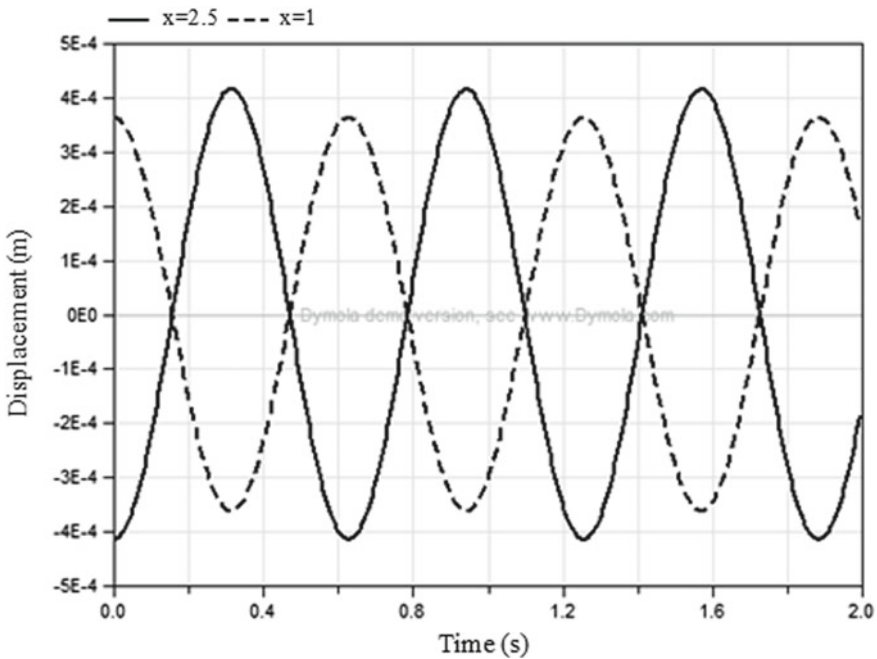
Fig. 3 Response of the simply supported beam under the excitation source
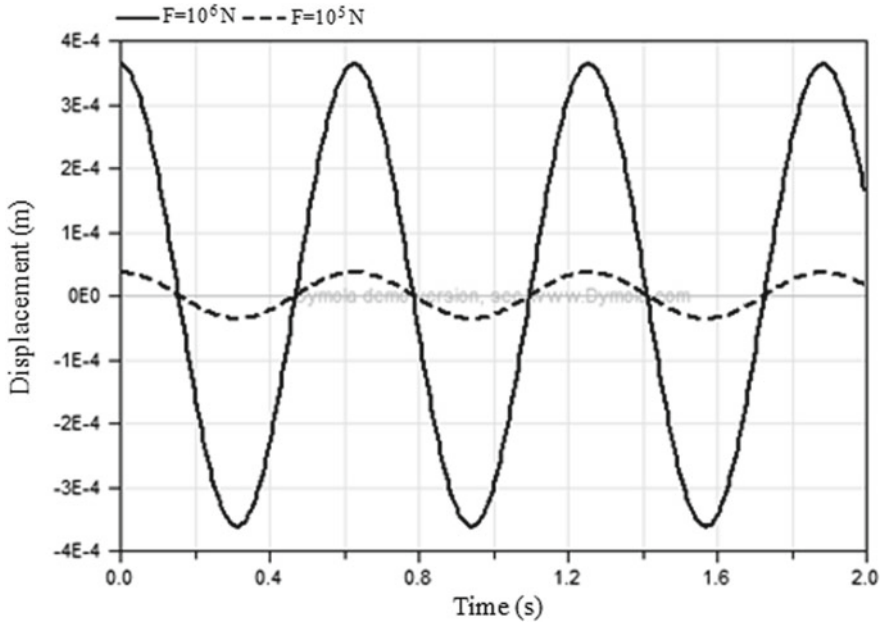
Fig. 4 Response of the simply supported beam for diverse values of the load amplitude

structure. It can be noted that the motion is depending on the point position. The two curves have the same oscillation frequency which corresponds to the excitation of the external force.

Figure 4 shows the motion in the mid span of the beam for diverse amplitudes values of the external load. It can be depicted that the motion amplitude increases with the growth of the load amplitude.

5 Conclusion

We have presented in this paper, a new pre-designing method to model-based parametric design of mechatronic system. Our study is based on the object oriented modeling language Modelica/Dymola to establish models. A case study is considered in our investigation. In fact, the vibration interaction between a dynamic excitation and a beam as a support structure is studied, where the excitation source position is parametrized. The preliminary results presented in this paper are quite encouraging. In fact, the aptitude to modify the parameters and to evaluate the possible missions represents a strong positive point for this new approach. This method requires less time and resources and permits for greater repeatability.

References

Buchacz A (2008) Characteristics of discrete-continuous flexibly vibrating mechatronic system. J Achievements Mater Manuf Eng 28(1):43–46

Hammadi M, Choley JY (2015) Parametric compact modeling of dynamical systems using meshfree method with multi-port technique. Int J Dyn Syst Differ Equ 5:206–219

Hamza G, Choley JY, Hammadi M, Barkallah M, Louati J, Riviere A, Haddar M (2015) Pre dimensioning of the dynamic properties of the wind turbine system using analytical approach. In: Design and modeling of mechanical systems II (CMSM' 2015). Springer, pp 179–188

Hamza G, Choley JY, Hammadi M, Barkallah M, Louati J, Riviere A, Haddar M (2015b) Pre-designing of a mechatronic system using an analytical approach with Dymola. J Theor Appl Mech 53:697–710

Hamza G, Hammadi M, Barkallah M, Choley JY, Riviere A, Louati J, Haddar M (2017) Conceptual design methodology for the preliminary study of a mechatronic system: application to wind turbine system. Mech Ind 18(4):413

Hamza G, Hammadi M, Barkallah M, Choley JY, Riviere A, Louati J, Haddar M (2018) Conceptual design decision support of a mechatronic system using analytical approach with Modelica. Mech Ind 19(1):103

Inceo Ĝ S, Gürgöze M (2001) Bending vibrations of beams coupled by several double spring-mass systems. J Sound Vibr 243(2):370–379

Tang HB, Wu CJ, Huang XQ (2008) Vibration analysis for a coupled beam-sdof system by using the recurrence equation method. J Sound Vibr 311(3–5):912–923

Veprik AM (2003) Vibration protection of critical components of electronic equipment in harsh environmental conditions. J Sound Vibr 259(1):161–175

Wu JS, Chen DW (2000) Dynamic analysis of a uniform cantilever beam carrying a number of elastically mounted point masses with dampers. J Sound Vibr 229(3):549–578

Zheng C, Le Duigou J, Bricogne M, Dupont E, Eynard B (2016) Interface model enabling decomposition method for architecture definition of mechatronic systems. Mechatronics 40:194–207

A Unified Topological Approach for the Modeling: Application to a 2D Beams Structure

Mariem Miladi Chaabane, Régis Plateaux, Jean-Yves Choley, Chafik Karra, Alain Riviere, and Mohamed Haddar

Abstract In this paper, a unified topological approach for the modeling of complex systems is presented. This approach is based on topological notions such as the topological collections and the transformations. These two topological notions allow the separation between the topological structure (interconnection laws) and the physics (behavioral laws) of the studied system. In fact, regardless of the complexity of the system, interconnection laws are declared through the topological collections and behavioral laws through the transformations. Therefore, a system is considered as local elements linked by neighbor relations to which local behavioral laws are associated. In order to show that the topological modeling approach is independent of the physical nature or the number of elementary components, a 2D beams structure with topological modification is taken as an example. In fact, a beams structure is a well-structured set of beams. Classical modeling consists in considering such structure as a global system and the resolution necessities the computation of the global stiffness matrix and therefore a modification of the beams structure involves the actualization of this matrix. Contrary to the classical approach, the application of the topological collections allow to consider a beams structure as local elements with no assembling terms as it is demonstrated through this paper.

Keywords Topological collections · Transformations · Local laws · Topological structures

M. Miladi Chaabane (✉) · C. Karra · M. Haddar
Mechanics, Modeling and Production Laboratory, National Engineering
School of Sfax (ENIS), Sfax, Tunisia
e-mail: mariam.mi@hotmail.fr

R. Plateaux · J.-Y. Choley · A. Riviere
QUARTZ Laboratory High, Institute of Mechanic of Paris (SUPMECA),
Saint-Ouen Cedex, France

1 Introduction

Technological development, consumer demand and industrial competition are leading to the emergence of more and more complex systems. These systems have a high level of integration of electronics, mechanics, automation and computing technologies, which necessitates an advanced modeling (Plateaux 2011). Since, the various domains of mechatronics can be represented by their topological structures and behavioral laws, a topological approach for modeling is taken up (Plateaux et al. 2007; Chaabane 2014). This approach permits to separate the topology and the physics of the studied system in order to have a standard model of characterization of all the physics of a complex system (Chaabane et al. 2013a, 2014a, b; Abdeljabbar Kharrat et al. 2017a, b, 2018).

The MGS (General System Model) language is applied to assure topological modeling. Indeed, this language is a research activity of he IBISC of the University of Evry allowing the study and the development of the contribution of notions of topological nature in programming languages as well as the application of these notions to the design of new data and control structures (Giavitto et al. 2002; Spicher and Michel 2007). Therefore, to assure the computation, in addition to its fundamental elements, MGS includes new types of values named topological collections, which composed, of a set of cells whose organization is captured by local relationships and affected by values. MGS applies transformations which are a series of rewriting rules to manipulate its data.

The main transformations are the case defined functions, the patches that are designed to change the cell structure and the path transformations that renew the values allied with the cells.

To ensure a topological modeling approach, collections are applied to present the system topology and transformations to identify the local behavior laws of its different components. Thus, a complex system will be described as a set of local elements.

In what follows, a short presentation of topological collections and transformations is presented. The topological approach is applied to a 2D beams structure and two particular cases of topological modification are taken to show the flexibility of the topological modeling.

2 Topological Collections and Transformations

In this section, collections and transformations are presented (Cohen 2004; Spicher 2006).

2.1 Topological Collections

There are several types of topological collections that can be classified into two categories:

- Leibnizian collection: space is defined from the elements it contains and their relative positions with respect to each other;
- Newtonian collection: Space is defined as an object having a proper existence on which other objects are placed and moved. For these type of collections, positions exist regardless of their decoration. The special value ⟨undef⟩ is associated with undecorated positions.

In this paper we are interested in the application of Newtonian collections for modeling and more precisely, we are interested in the application of topological collections of type abstract chain. Figure 1 shows an example of an abstract chain and the associated MGS code. For this type of topological collection, the topology is explicitly defined by the creation of new cells. These cells are then decorated using sum and product operators. To browse the cells of an abstract string denoted c, the following functions are used:

- faces (c): provides the list of faces of c;
- cofaces (c): provides the list of cofaces of c;
- icells (c): provides the list of cells incident to c;
- pcells (c, p): provides the list of p-neighbors of c.
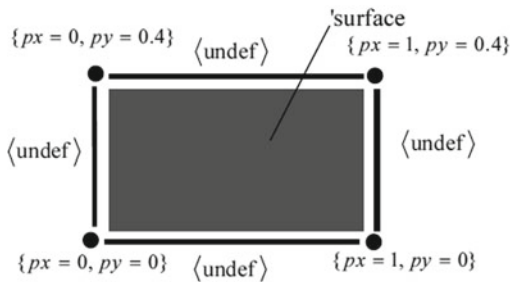
$V_1 := add\_acell(0,seq:(),seq:());;$
$V_2 := add\_acell(0,seq:(),seq:());;$
$V_3 := add\_acell(0,seq:(),seq:());;$
$V_4 := add\_acell(0,seq:(),seq:());;$
$e_1 := add\_acell(1,(V_1,V_2),seq:());;$
$e_2 := add\_acell(1,(V_2,V_3),seq:());;$
$e_3 := add\_acell(1,(V_3,V_4),seq:());;$
$e_4 := add\_acell(1,(V_4,V_1),seq:());;$
$f := add\_acell(2,(e_1,e_2,e_3,e_4),seq:());;$
$\{px = 0, py = 0\}^\bullet V_1$
$+ \{px = 0, py = 0.4\}^\bullet V_2$
$+ \{px = 1, py = 0.4\}^\bullet V_3$
$+ \{px = 1, py = 0\}^\bullet V_4$
$+ \,'surface^\bullet f;;$

Fig. 1 Example of abstract chain and associated MGS code

2.2 Transformations

Transformations are described as a series of rewriting rules $\{m_1 \Rightarrow e_1; m_2 \Rightarrow e_2, \ldots\}$. When a rule is applied for a topological collection, sub-collections respecting that pattern m_i are substituted by the topological collection calculated according the expression e_i (e_i is the expression that substitutes the occurrences of m_i). Thus, the procedure for applying a transformation to a topological collection can be summed up in three stages. Let C be a topological collection. First, sub-collections A of C are chosen according to the pattern; second, for each chosen sub-collection A, a new sub-collection A_0 is evaluated from A. Third, the evaluated sub-collections A_0 substitute the selected sub-collections A and so on.

3 Topological Modeling of a 2D Beams Structure

The generic topological approach for the modeling of beams structures is to represent the structure by an abstract cellular complex to which the variables of interest are assigned. Once the system has been written as a topological collection, local behavior laws of the main components (beam, frame, force and node) of beams structures are specified through transformations.

The studied beams structure is presented in Fig. 2.

Fig. 2 Studied 2D beams structure
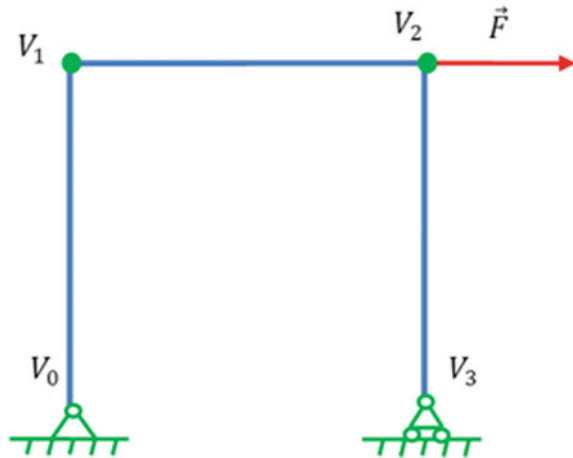
3.1 Topological Structure

The main components of a beams structure are beam, frame, force and node. Therefore to represent a beam structure as a cellular complex: 0-cells represent nodes, 1 cells represent beams frames or forces such as 1-cells ended with two 0-cells represent beams and 1-cells ended with one 0- cells represent forces or frames. Figure 3 represents the studied 2D beams structure as a cellular complex.

The topological structure of the 2D beams structure is connected by locals relationships: the cofaces of P_2 are $\{e_2, e_3, e_f\}$, the face of e_{b1} is $\{P_0\}$ and the faces of e_2 are $\{P_1, P_2\}$.

Once a beams structure is presented in the form of a cellular complex, this structure is then decorated with variables.

Figure 4 represents the studied 2D beams structure as a topological collection. Variables are associated to each cells (length L, displacement U, V, Θ, modulus young E, force F, moment M …). For example:

$$P_1 = \{U_1, V_1, \Theta_1\};$$
$$\{e_{b1}\} = \{F_{i\_b1}, F_{j\_b1}, M_{i\_b1}, M_{j\_b1}\};$$
$$\{e_2\} = \{F_{i\_12}, F_{j\_12}, M_{i\_12}, M_{j\_12}, L_{12}\ldots\}$$

Fig. 3 Presentation as a cellular complex of the studied 2D beams structure

$$P_1 = \{U_1, V_1, \Theta_1, ...\}$$

$$e_2 = \begin{Bmatrix} F_{i\_12}, F_{j\_12}, M_{i\_12}, \\ M_{j\_12}, L_{\_12}, ... \end{Bmatrix} \quad e_f = \{F_{i\_f}, F_{j\_f}, M_{i\_f}, M_{j\_f}\}$$

$$P_2 = \{U_2, V_2, \Theta_2, ...\}$$

$$e_1 = \begin{Bmatrix} F_{i\_01}, F_{j\_01}, M_{i\_01}, \\ M_{j\_01}, L_{\_01}, ... \end{Bmatrix}$$

$$e_3 = \begin{Bmatrix} F_{i\_23}, F_{j\_23}, M_{i\_23}, \\ M_{j\_23}, L_{\_23}, ... \end{Bmatrix}$$

$$P_0 = \{U_0, V_0, \Theta_0, ...\}$$

$$P_3 = \{U_3, V_3, \Theta_3, ...\}$$

$$e_{b1} = \{F_{i\_b1}, F_{j\_b1}, M_{i\_b1}, M_{j\_b1}\}$$

$$e_{b2} = \{F_{i\_b2}, F_{j\_b2}, M_{i\_b2}, M_{j\_b2}\}$$
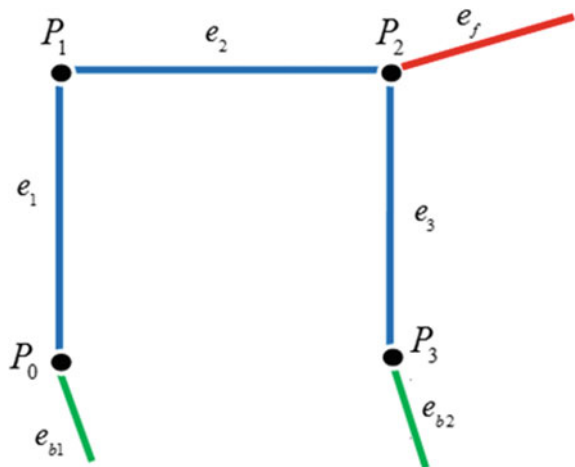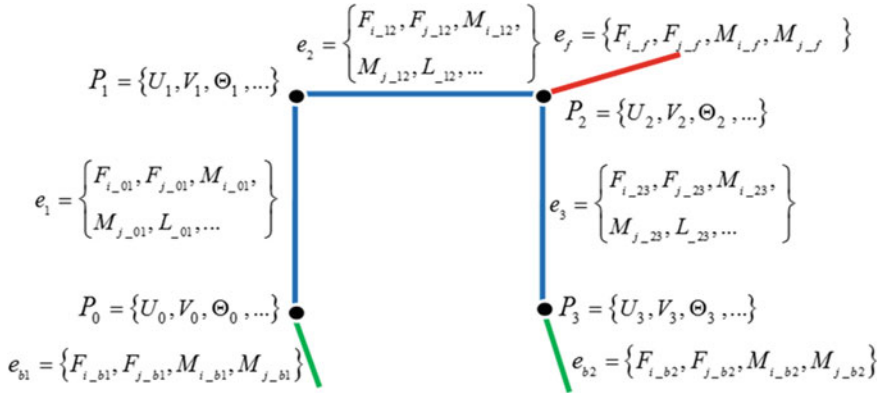
Fig. 4 Presentation as a topological collections of the studied 2D beams structure

3.2 Local Behavior Laws

Transformations are applied to identify local behavior laws of nodes, beams, forces and frames. The creation of system's equations is done by swiping all cells describing the beams structure.

Table 1 presents local laws for 0-cells.

For nodes P_0, P_1, P_2 and P_3 the local equations (equilibrium equations) are respectively given by Eqs. 1, 2, 3 and 4.

$$\begin{cases} \overrightarrow{F_{i\_01}} + \overrightarrow{F_{j\_b1}} = \overrightarrow{0} \\ \overrightarrow{M_{i\_01}} + \overrightarrow{M_{j\_b1}} = \overrightarrow{0} \end{cases} \tag{1}$$

$$\begin{cases} \overrightarrow{F_{j\_01}} + \overrightarrow{F_{i\_12}} = \overrightarrow{0} \\ \overrightarrow{M_{j\_01}} + \overrightarrow{M_{i\_12}} = \overrightarrow{0} \end{cases} \tag{2}$$

$$\begin{cases} \overrightarrow{F_{j\_12}} + \overrightarrow{F_{i\_23}} + \overrightarrow{F_{i\_f}} = \overrightarrow{0} \\ \overrightarrow{M_{j\_12}} + \overrightarrow{M_{i\_23}} + \overrightarrow{M_{i\_f}} = \overrightarrow{0} \end{cases} \tag{3}$$

Table 1 Local laws for nodes (0-cells)

Topological structure	Physical structure (local behavior laws and/or equilibrium equations)
Node P, arc1, arc j, arc N	$\begin{cases} \sum_{j=1}^{N} \overrightarrow{F_j} = \overrightarrow{0} \\ \sum_{j=1}^{N} \overrightarrow{M_j} = \overrightarrow{0} \end{cases}$ N the number of concurrent arcs e to the node P

$$\begin{cases} \overrightarrow{F_{j\_23}} + \overrightarrow{F_{i\_b2}} = \overrightarrow{0} \\ \overrightarrow{M_{j\_23}} + \overrightarrow{M_{i\_b2}} = \overrightarrow{0} \end{cases} \tag{4}$$

Table 2 presents local laws for 1-cells ended with 1 0-cell (forces or frames).

For force e_f, frame e_{b1} and frame e_{b2}, the local equations (equilibrium equation) are respectively given by Eqs. 5, 6 and 7.
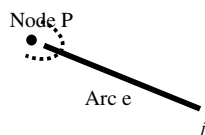
$$\begin{cases} \overrightarrow{F_{j\_f}} + \overrightarrow{F_{i\_f}} = \overrightarrow{0} \\ \overrightarrow{M_{j\_f}} + \overrightarrow{M_{i\_f}} = \overrightarrow{0} \end{cases} \tag{5}$$

$$\begin{cases} \overrightarrow{F_{j\_b1}} + \overrightarrow{F_{i\_b1}} = \overrightarrow{0} \\ \overrightarrow{M_{j\_b1}} + \overrightarrow{M_{i\_b1}} = \overrightarrow{0} \end{cases} \tag{6}$$
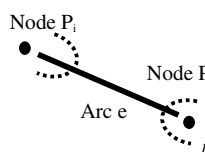
$$\begin{cases} \overrightarrow{F_{j\_b2}} + \overrightarrow{F_{i\_b2}} = \overrightarrow{0} \\ \overrightarrow{M_{j\_b2}} + \overrightarrow{M_{i\_b2}} = \overrightarrow{0} \end{cases} \tag{7}$$

Table 3 presents local laws for 1-cells ended with by two 0-cells.

Table 2 Local laws for forces or frames (1-cells bounded by 1 0-cell)

Topological structure	Physical structure (local behavior laws and/or equilibrium equations)
Node P Arc e j	$\begin{cases} \overrightarrow{F_i} + \overrightarrow{F_j} = \overrightarrow{0} \\ \overrightarrow{M_i} + \overrightarrow{M_j} = \overrightarrow{0} \end{cases}$ i and j denote the ends of the arc

Table 3 Local laws for 2D beams (1-cells bounded by 2 0-cells)

Topological structure	Physical structure (local behavior laws and/or equilibrium equations)
Node P_i Node P_j Arc e j	$\begin{cases} \overrightarrow{F_i} + \overrightarrow{F_j} = \overrightarrow{0} \\ \overrightarrow{M_i} + \overrightarrow{M_j} + \overrightarrow{F_j} \wedge \overrightarrow{L_{ij}} = \overrightarrow{0} \\ \{\tau\} = [K]\{\Delta P\} \end{cases}$ where: i and j denote the ends of the arc $\{\overrightarrow{\tau}\} = \left\{ F_{X_i} \ F_{Y_i} \ M_i \ F_{X_j} \ F_{Y_j} \ M_j \right\}^T$ is the force vector in the global coordinate system $\{\overrightarrow{\Delta P}\} = \left\{ U_i \ V_i \ \Theta_i \ U_j \ V_j \ \Theta_j \right\}^T$ is the displacement vector in the global coordinate system $[K]$ is the local stiffness matrix of a beam element in the global coordinate system (Chaabane et al. 2014c)

For beams e_1, e_2 and e_3 the local equations (equilibrium equations and local behavior laws) are respectively given by Eqs. 8, 9 and 10.

$$\begin{cases} \overrightarrow{F_{i\_01}} + \overrightarrow{F_{j\_01}} = \vec{0} \\ \overrightarrow{M_{i\_01}} + \overrightarrow{M_{j\_01}} + \overrightarrow{F_{j\_01}} \wedge \overrightarrow{L\_01} = 0 \\ \left\{ \begin{array}{c} \overrightarrow{F_{i\_01}} \\ \overrightarrow{M_{i\_01}} \end{array} \right\} = \begin{bmatrix} K\_01 \end{bmatrix} \left\{ U_0 \ V_0 \ \Theta_0 \ U_1 \ V_1 \ \Theta_1 \right\}^t \end{cases} \tag{8}$$

$$\begin{cases} \overrightarrow{F_{i\_12}} + \overrightarrow{F_{j\_12}} = \vec{0} \\ \overrightarrow{M_{i\_12}} + \overrightarrow{M_{j\_12}} + \overrightarrow{F_{j\_12}} \wedge \overrightarrow{L\_12} = 0 \\ \left\{ \begin{array}{c} \overrightarrow{F_{i\_12}} \\ \overrightarrow{M_{i\_12}} \end{array} \right\} = \begin{bmatrix} K\_12 \end{bmatrix} \left\{ U_1 \ V_1 \ \Theta_1 \ U_2 \ V_2 \ \Theta_2 \right\}^t \end{cases} \tag{9}$$

$$\begin{cases} \overrightarrow{F_{i\_23}} + \overrightarrow{F_{j\_23}} = \vec{0} \\ \overrightarrow{M_{i\_23}} + \overrightarrow{M_{j\_23}} + \overrightarrow{F_{j\_23}} \wedge \overrightarrow{L\_23} = 0 \\ \left\{ \begin{array}{c} \overrightarrow{F_{i\_23}} \\ \overrightarrow{M_{i\_23}} \end{array} \right\} = \begin{bmatrix} K\_23 \end{bmatrix} \left\{ U_2 \ V_2 \ \Theta_2 \ U_3 \ V_3 \ \Theta_3 \right\}^t \end{cases} \tag{10}$$

For beam 3 the local rigidity matrix is given by Eq. 11.

$$[K_{23}] = \begin{bmatrix} k_{2,23} & 0 & k_{4,23} & -k_{2,23} & 0 & k_{4,23} \\ 0 & k_{1,23} & 0 & 0 & -k_{1,23} & 0 \\ k_{4,23} & 0 & k_{3,23} & -k_{4,23} & 0 & \frac{k_{3,23}}{2} \end{bmatrix} \tag{11}$$

where $k_1 = \frac{EA}{L}$; $k_2 = \frac{12EI}{L^3}$; $k_3 = \frac{4EI}{L}$ and $k_4 = \frac{6EI}{L^2}$ (E, A, L and I respectively represent young's modulus, cross sectional area, length and inertia of the beam).

We can notice from the equations generated by the MGS language for the different cells representing the system (Eqs. 1–11) that local laws of elementary components are considered instead of the global behavior law of the structure. The assembly is indirectly done from neighborhood relationships.

3.3 Advantages of Topological Modeling

Contrary to the classical approach based on the displacement method(Liu and Quesk 2003), the advantage of the topological modeling for beams structure (Chaabane et al. 2012, 2013b) is that local behavior laws of beams are independently declared of their number and the way in which they are connected. Therefore the topological approach allows the simplification of the modeling of the beams structures: only topological structure is required. Then all the modifications (such as the addition/deletion of one or more beams, modification at the level of connections or efforts) are only realized through the topological structure. Local laws are the same (Tables 1, 2 and 3).

Fig. 5 Topological modification: addition of a beam
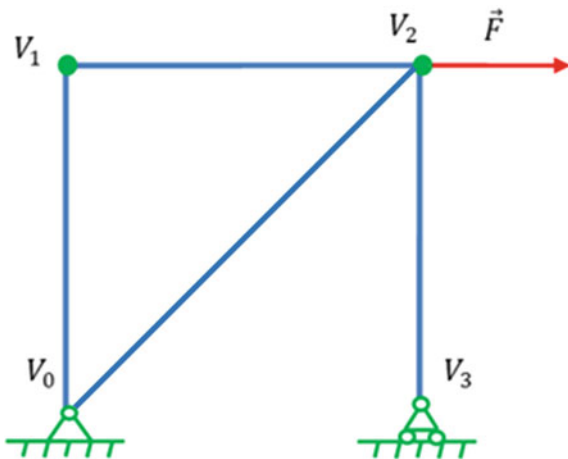
For example, if a fourth beam is added (Fig. 5), it suffices to change the topological structure by adding the cells related to the addition of the fourth beam (e_4).

The neighborhood relationships change for the nodes P_0 and P_2 (cofaces of P_0 are $\{e_1, e_4, e_{b1}\}$, cofaces of P_2 are $\{e_2, e_3, e_4, e_f\}$). Also, the relationship of neighborhood associated to the bar 4 is added (the faces of e_4 are $\{P_0, \ P_2\}$).

The equations generated by the MGS languages automatically change according to the topological structure. Therefore equilibrium equations of node P_0 and P_2 are changed and the local equation of beam 4 is added.

For P_0, P_2 and e_4 the local equations are respectively given by Eqs. 12, 13 and 14.

$$\begin{cases} \overrightarrow{F_{i\_01}} + \overrightarrow{F_{i\_04}} + \overrightarrow{F_{j\_b1}} = \overrightarrow{0} \\ \overrightarrow{M_{i\_01}} + \overrightarrow{M_{i\_04}} + \overrightarrow{M_{j\_b1}} = \overrightarrow{0} \end{cases} \tag{12}$$

$$\begin{cases} \overrightarrow{F_{j\_12}} + \overrightarrow{F_{i\_23}} + \overrightarrow{F_{j\_04}} + \overrightarrow{F_{i\_f}} = \overrightarrow{0} \\ \overrightarrow{M_{j\_12}} + \overrightarrow{M_{i\_23}} + \overrightarrow{M_{j\_04}} + \overrightarrow{M_{i\_f}} = \overrightarrow{0} \end{cases} \tag{13}$$

$$\begin{cases} \overrightarrow{F_{i\_04}} + \overrightarrow{F_{j\_04}} = \overrightarrow{0} \\ \overrightarrow{M_{i\_04}} + \overrightarrow{M_{j\_04}} + \overrightarrow{F_{j\_04}} \wedge \overrightarrow{L\_04} = 0 \\ \left\{ \begin{matrix} \overrightarrow{F_{i\_04}} \\ \overrightarrow{M_{i\_04}} \end{matrix} \right\} = \left[K\_04 \right] \left\{ U_0 \ V_0 \ \Theta_0 \ U_4 \ V_4 \ \Theta_4 \right\}^T \end{cases} \tag{14}$$

Also if we consider the case where the force is applied at the node P_1 instead of P_2 compared with the structure presented in Fig. 5. The equations generated by the MGS languages automatically change according to the new topological structure. Therefore only the equilibrium equations of the node P_1 and P_2 changed.

For P_1 and P_2 the local equations are respectively given by Eqs. 15 and 16.

$$\begin{cases} \overrightarrow{F_{j\_01}} + \overrightarrow{F_{i\_12}} + \overrightarrow{F_{i\_f}} = \overrightarrow{0} \\ \overrightarrow{M_{j\_01}} + \overrightarrow{M_{i\_12}} + \overrightarrow{M_{i\_f}} = \overrightarrow{0} \end{cases} \qquad (15)$$

$$\begin{cases} \overrightarrow{F_{j\_12}} + \overrightarrow{F_{i\_23}} + \overrightarrow{F_{j\_04}} = \overrightarrow{0} \\ \overrightarrow{M_{j\_12}} + \overrightarrow{M_{i\_23}} + \overrightarrow{M_{j\_04}} = \overrightarrow{0} \end{cases} \qquad (16)$$

4 Conclusion

In this paper, a topological approach based on topological collections and transformations is used as a unified approach for the modeling. This approach makes it possible to distinguish between structure and behavior. Systems are considered as a set of local elements linked by neighborhood relationships that facilitate the modeling of complex systems. The example of a 2D beams structure is studied. Two cases of topological modification are considered to approve the generic approach of topological modeling. Indeed, only the topological structure is modified and the local behavior and equilibrium equations of the different elements of a beams structure are independently declared of the studied beam structure.

References

Abdeljabbar Kharrat N, Plateaux R, Chaabane MM, Choley J-Y, Karra C, Hadda M (2017a) Topological modeling of 2D piezoelectric truss structure using the MGS language. In: International conference design and modeling of mechanical systems. Springer, Cham

Abdeljabbar Kharrat N, Plateaux R, Chaabane MM, Karra C, Choley J-Y, Haddar M (2017b) Topological modeling of a wind turbine. In: IEEE international systems engineering symposium, pp 1–6

Abdeljabbar Kharrat N, Plateaux R, Chaabane MM, Karra C, Choley J-Y, Haddar M (2018) Integration of topological modification within the modeling of multi-physics systems: application to a Pogo-stick. Comptes Rendus Mécanique 346(5):351–365

Chaabane MM, Plateaux R, Choley J-Y, Karra C, Rivière A, Haddar M (2012) Topological approach to solve 2D truss structure using MGS language. In: 9th France–Japan and 7th Europe–Asia congress on mechatronics (MECATRONICS)/research and education in mechatronics, REM, Paris, IEEE

Chaabane MM, Plateaux R, Choley J-Y, Karra C, Riviere A, Haddar M (2013a) New topological approach for the modelling of mecatronic systems: application for piezoelectric structures. Eur J Comput Mech (Revue Européenne de Mécanique Numérique) 22(2–4):209–227

Chaabane MM, Plateaux R, Choley J-Y, Karra C, Riviere A, Haddar M (2013b) New approach to solve dynamic truss structure using topological collections and transformations. Int J Mech Syst Eng IJMSE 3(4):162–169

Chaabane MM (2014) Modélisation géométrique et mécanique pour les systèmes mécatroniques. Ph.D. thesis, National School of engineers of Sfax and Ecole Centrale Paris

Chaabane MM, Plateaux R, Choley J-Y, Karra C, Riviere A, Haddar M (2014a) Topological approach for the modeling of complex and mechatronic systems. In; Mechatronic systems: theory and applications. Springer, Cham, pp 15–21

Chaabane MM, Plateaux R, Choley J-Y, Karra C, Riviere A, Haddar M (2014b) Topological modeling of a one stage spur gear transmission. Chin J Mech Eng 27(5):900–908

Chaabane MM, Plateaux R, Choley J-Y, Karra C, Rivière A, Haddar M (2014c) Topological approach to solve frame structures using topological collections and transformations. CR Mec 342(8):466–477

Cohen J (2004) Intégration des collections topologiques et des transformations dans un langage fonctionnel. Ph.D. thesis, University of Evry Val d'Essonne

Giavitto J-L, Godin C, Michel O, Prusinkiewicz P (2002) Computational models for integrative and developmental biology. In: Modelling and simulation of biological processes in the context of genomics, Hermès, Paris

Liu GR, Quek S (2003) The finite element method: a practical course. Butterworth-Heinemann, Oxford, Boston

Plateaux R, Penas O, Rivière A, Choley J-Y (2007) A need for the definition of a topological structure for the complex systems modelling. In: Conception et Production Intégrées CPI'2007, Rabat, Maroc

Plateaux R (2011) Continuité et cohérence d'une modélisation des systèmes mécatroniques basée (s) sur une structure topologique. Ph.D. thesis, Superior Engineering Institute of Paris SUPMECA

Spicher A, Michel O (2007) Declarative modeling of a neurulation-like process. BioSystems 87(2–3):281–288

Spicher A (2006) Transformation de collections topologiques de dimension arbitraire. Application à la modélisation de systèmes dynamiques. Ph.D. thesis, University of Evry Val d'Essonne

Micro Electro Mechanical Systems Modeling by VHDL-AMS: Application to a Piezoresistive Pressure Sensor

Radouane Otmani and Nasreddine Benmoussa

Abstract Micro Electro-Mechanical Systems (MEMS) are highly integrated devices, including sensors and actuators with their interface of signal processing. MEMS are hybrid systems that may include various electrical (digital and analogical) and non-electrical (mechanical, thermal, etc.) phenomena. This nature of MEMS and their phenomenal development, making them more and more complex, is not going along with the only one level of abstraction! Indeed, such complex systems, with multi-physical and multi-technological characteristics, require new tools for their simulation. Since the late 90s, which has known the appearance of MEMS and their rapid development, the scientific community faces a major challenge. At that time, MEMSs were already brought to replace ordinary microelectronic components. So they had to find a new modeling tool for them. To address this problem, the scientific community has started to develop new tools for multi-domain description of MEMS at multiple levels of abstraction simulation. New hardware description languages such as Verilog-AMS and VHDL-AMS have been developed for the description and simulation of such complex systems. In this paper, we tried to give multi levels of abstraction description of a micro machined piezoresistive pressure sensor. Such sensor combines mechanical, electrical and thermal phenomena which will be described and simulated at different levels of abstraction.

Keywords MEMS · VHDL-AMS · Multi-level of abstraction · Piezoresistivity · Sensors · Electronic mobility

1 Introduction

Modeling a MEMS need to study it at all levels (domains). The use of traditional multi-physics simulation for MEMS wasted a lot of computing time. Indeed, these simulators are at one level of abstraction, and they do not offer the possibility of

R. Otmani (✉) · N. Benmoussa
Unit of Research on Materials and Renewable Energies, University of Tiaret, Tiaret, Algeria
e-mail: radouane.otmani@univ-tiaret.dz

N. Benmoussa
e-mail: nasreddinebenmoussa@yahoo.fr

modeling different parts of the component with different degrees of complexity to optimize the computation time without affecting the degree of resolution.

In this article we will show the interest of the VHDL-AMS simulation tool in the study of Micro Electro-Mechanical Systems by providing a simple and didactic example. We will model and simulate a micro piezoresistive pressure sensor.

2   Description of VHDL-AMS

This type of modeling is not only used to model hybrid electric systems (analogical and digital), but also non-electrical ones (thermal, magnetic, mechanical …). VHDL-AMS is one of the most languages used for multi domain modeling and simulation. It is an extension of the VHDL description language designed for continuous and mixed systems. The VHDL-AMS allows the description and simulation of multi-technological systems through terminals with associated physical quantities who obey the law of conservation when they are interconnected.

Writing a model in VHDL-AMS is direct and the difficulty of solving the equations is transparent to the programmer. Indeed, the writing of a complex physics equation (non-linear differential equation with possible discontinuity) requires a single simultaneous instruction (a single line of code in VHDL-AMS).

Two additional benefits of VHDL-AMS serve the interests of the industry:

- The language is standard (IEEE 1076.1 1999). Models are independent of simulation tools and are portable. This facilitates their reuse.
- The VHDL-AMS allows multi-abstraction models. It means that more or less detailed models (functional, behavioral, or physical) can be described, mixed and simulated. This facilitates hierarchical design of complex systems and optimizes the accuracy and the resolution time of the modeled system.

A VHDL-AMS program consists of one or more entities. An entity is a declarative block of the system with inputs and outputs called terminals, which can be of any physical nature. The interior and the organization of the entity is described in another block called architecture (an entity can contain one or multiple architectures).

3   The Multi-Physical Model of the Micro Pressure Sensor

3.1   Mechanical Modeling of the Membrane

A piezoresistive pressure sensor is composed of a square membrane, of few millimeters side and a few tens of microns thick. Under the effect of a differential pressure, this membrane is deformed in one direction or the other depending on the sign of

this pressure. Piezoresistive gauges located at the surface to detect the deformation by a change in their resistance value. This membrane is the mechanical part of the sensor (Fig. 1).

The deformation of the membrane and it relation with the applied pressure is given by partial differential equation called Lagrange equation (Olszacki et al. 2008; Timoshenko and Woinowsky-Krieger 1982). In this section, we will model the principle effects of a homogenous pressure on the membrane that are the flex of the membrane and stress induced on its surface. This will allow a good positioning of gauges on the membrane to get a maximum sensitivity of the sensor.

$$\frac{\partial^4 W(x,y)}{\partial x^4} + 2\alpha_{Si}\frac{\partial^4 W(x,y)}{\partial y^2 . \partial x^2} + \frac{\partial^4 W(x,y)}{\partial y^4} = \frac{P}{D} \tag{1}$$

The numerical resolution of this equation gives us the deflexion W(x, y) (Fig. 2). We remark that the flex is maximum in the membrane center and null on the perfectly clamped boards.
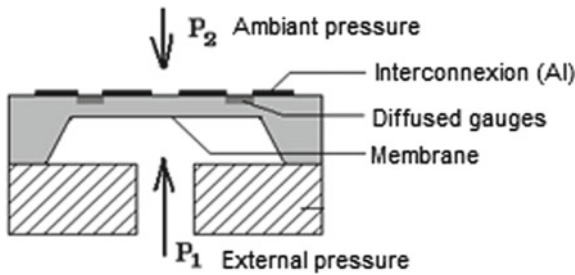
Fig. 1 Structure of a micro-pressure sensor
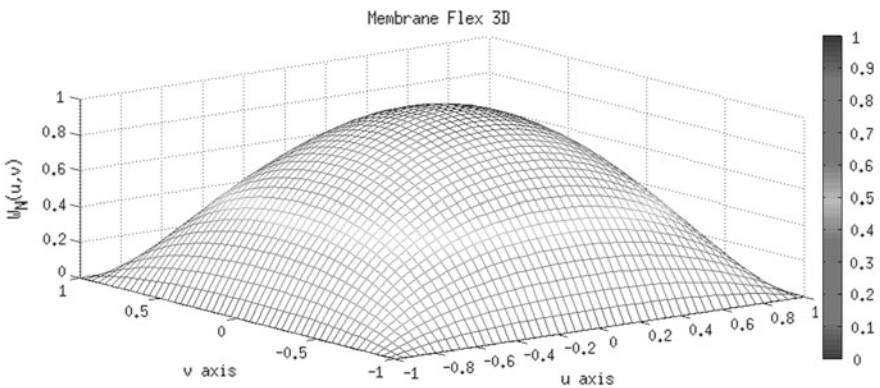
Fig. 2 Flex of the membrane

The relation between stress created en the membrane and its deflexion is given in Eq. (2).

$$
\begin{cases}
\sigma_x = -\dfrac{3}{2}\left(\dfrac{\partial^2 W(x, y)}{\partial x^2} + \upsilon_1 \dfrac{\partial^2 W(x, y)}{\partial yy^2}\right) \\[3mm]
\sigma_y = -\dfrac{3}{2}\left(\dfrac{\partial^2 W(x, y)}{\partial y^2} + \upsilon_1 \dfrac{\partial^2 W(x, y)}{\partial x^2}\right) \\[3mm]
\sigma_{xy} = -3\dfrac{G}{E}(1 - \vartheta^2)\left(\dfrac{\partial^2 W(x, y)}{\partial x.\partial y}\right)
\end{cases}
\tag{2}
$$

σ_x is the longitudinal stress (according x axis), σ_y is the transversal stress (according y axis), and σ_{xy} is the shear stress. By plotting results we can know the total stress distribution on the membrane surface (Fig. 3), and then, localize where the stress is maximum to place there the piezoresistive gauges.

From these results, we localize the longitudinal and transversal maximum stress on the edges of the membrane. Exactly at $\pm 92\%$ of the half membrane side calculated from its centre. The value of the shear stress σ_{xy} is ten times smaller than σ_x and σ_y (Benmoussa et al. 2014).
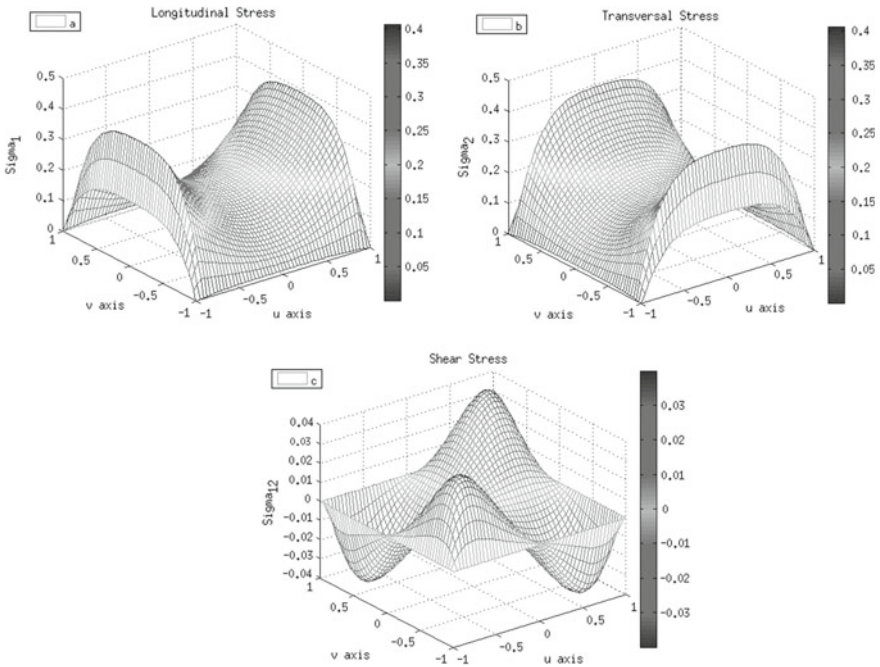
Fig. 3 Stress distribution on the membrane surface **a** Longitudinal stress, **b** Transversal stress, **c** Shear stress

3.2 Electrical Modeling of the Transduction Circuit

For passive sensors, especially resistive and piezoresistive transduction techniques, the Wheatstone bridge (Fig. 4) is by far the most used circuit. It allows offset tension rejection, and permit thermal drift compensation.

Submitted to pressure, the resistivity of Silicon gauges changes according to the following general equation, given by (Smith 1954).

$$\frac{\Delta\rho}{\rho} = \sigma\pi \tag{3}$$

where σ is the stress tensor and π is the piezoresistive coefficient tensor. In case of semiconductors, where geometric deformations are negligible, this equation is approached to (Eq. 4).

$$\frac{\Delta\rho}{\rho} = \frac{\Delta R}{R} = \sigma\pi \tag{4}$$

For each diffused gauge on the membrane surface, the resistance variation is given by (Eq. 5):

$$\frac{\Delta R}{R} = \sigma_x \pi_{11} + \sigma_y \pi_{12} + \sigma_{xy} \pi_{44} \tag{5}$$

By considering σ_{xy} negligible, the equation above is simplified to (Eq. 6):

Fig. 4 Transduction circuit integration on the membrane surface
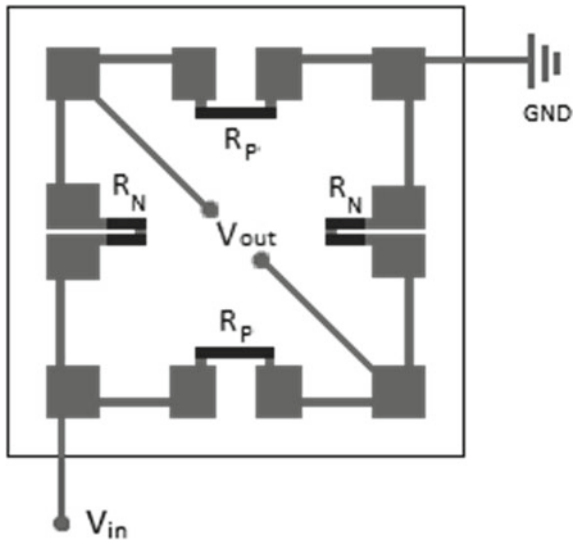
$$\frac{\Delta R}{R} = \sigma_x \pi_{11} + \sigma_y \pi_{12} \tag{6}$$

The diffused gauges (Fig. 4) on the membrane edges are submitted to σ_x and σ_y. R_P are called parallel gauges and they are submitted to σ_{ymax} and σ_{xmin}. R_N are called normal gauges and they are submitted to σ_{xmax} and σ_{ymin}.

By that, parallel and normal gauges can be written as follow:

$$\frac{\Delta R}{R}|_P = \sigma_{min} \pi_{11} + \sigma_{max} \pi_{12} \tag{7}$$

$$\frac{\Delta R}{R}|_N = \sigma_{max} \pi_{11} + \sigma_{min} \pi_{12} \tag{8}$$

On the other hand, the output voltage of a Wheatstone bridge constituted by two parallel and two normal gauges is given by the following equation:

$$V_{out} = \left(\frac{(R_N + \Delta R_N) - (R_P + \Delta R_P)}{(R_N + \Delta R_N) + (R_P + \Delta R_P)} \right) . V_{in} \tag{9}$$

3.3   Thermal Modeling of the Piezoresistive Gauges

In semiconductor devices, temperature effect is more important than in all other conductor materials. Electrons and holes mobility in semiconductors are highly depending on temperature variations, which will affect the resistivity values of the gauges (Arora et al. 1982; Dorckel and Leturcq 1981). Otherwise, piezoresistive coefficients, which depend on doping concentration, are also depending on temperature (Kanda 1991). Therefore, we need to model the temperature and doping concentration effect on both piezoresistive coefficient and holes mobility since we are using P-type gauges for our sensor.

Holes mobility is highly depending on temperature and doping concentration. We used two models, Arora model and Dorkel model, to demonstrate this dependence. Using these models, we plotted the relative resistance variation of gauges against temperature and doping concentration (Fig. 5).

We can detect a slight parabolicity of the curves for both models. The relation between resistivity and temperature should be modelled at least by a second order polynomial equation (Eq. 10).

$$R(T) = R_0 \left(1 + \alpha T + \beta T^2 \right) \tag{10}$$

α and β are the first and second order temperature coefficients respectively. There values can be extrapolated from curves on (Fig. 5). We plotted the results of this extrapolation on (Fig. 6).
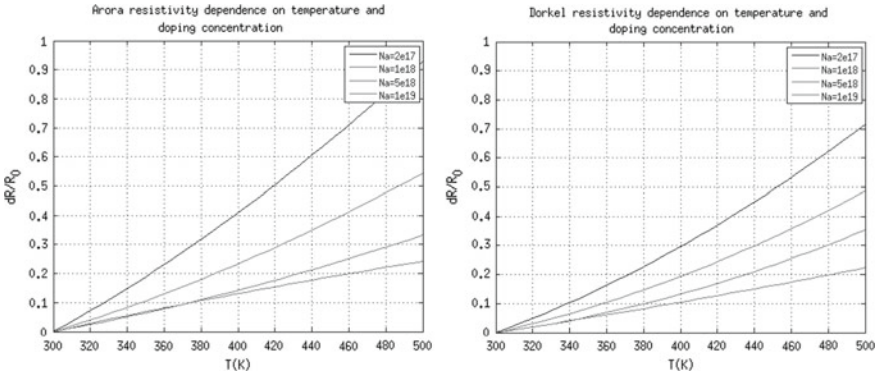
Fig. 5 Piezoresistive coefficients dependence on temperature and doping concentration
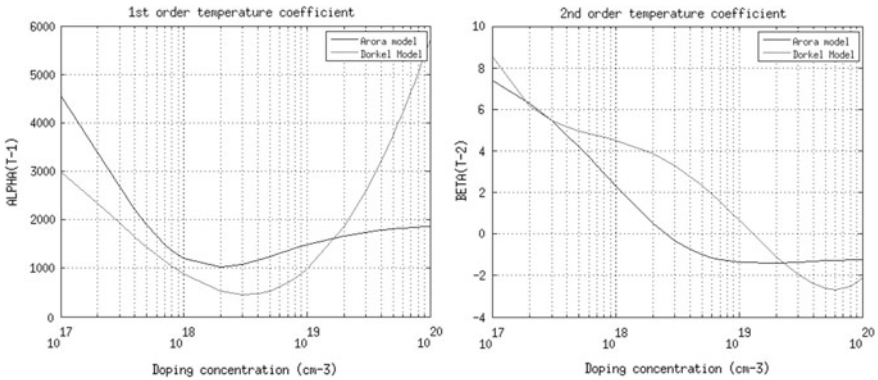
Fig. 6 The first and second order temperature coefficient depending on doping concentration (Otmani et al. 2011)

The comparison of these results with experimental ones (Boukabache 1993) is given in (Table 1). It shows that Dorkel model give better description of the temperature effect on gauges resistivity. Therefore, it will be adopted to model the thermal behaviour of the piezoresistive gauges.

The minimum value of the most significant temperature coefficient α is obtained at a doping concentration of about 2×10^{18} cm^{-3}. This information will be taken in account to minimize temperature effect on the sensor.

4 Micro Pressure Sensor Simulation by VHDL-AMS

Since our system (sensor) is divided into two domains (parts), we will simulate it by dividing into two main entities:

Table 1 Theoretical temperature coefficients comparison with experimental results

	2×10^{18} (cm^{-3})		5×10^{18} (cm^{-3})		10^{19} (cm^{-3})	
	Alpha (ppm/°C)	Beta (ppm/°C)	Alpha (ppm/°C)	Beta (ppm/°C)	Alpha (ppm/°C)	Beta (ppm/°C)
Otmani et al. (2011)	1000	0.51	1200	−099	1500	−1.36
Otmani et al. (2011)	522	3.86	532	2.32	983	0.67
Boukabache (1993)	516	3.6	400	3.2	905	1.2

1st Entity "the membrane": This is a block that contains three mains terminals (interconnecting nodes) and two intermediates terminals. The five terminals are:

- "T_Pin" An input fluidic type terminal: to this terminal will be applied to the mechanical pressure.
- Two intermediate terminals "T_sigma_l" and "T_sigma_t" of fluidic nature.
- Two output terminals "T_dRn" and "T_dRp" of electrical nature. These terminals receive the resistance variation of gauges induced by normal and parallel strain in the membrane.

2nd Entity "the wheatstone_Bridge": This entity has three main terminals:

- An input "T_Pin" terminal: it will be connected to the terminal of the previous entity with the same name.
- Two electrical terminals "T_V1" and "T_V2": they will provide the potential difference at the output of the Wheatstone bridge.

Other internal terminals are also needed for architecting this entity.

5   VHDL-AMS Code

```
---VHDL-AMS      MODELLING      OF      A
PIEZORESISTIVE PRESSURE SENSOR--
   -- ENTITY : PRESSION APPLIQUEE --
   library ieee;
   library disciplines;
   library work;
   use ieee.math_real.all;
   use disciplines.fluidic_system.all;
   use disciplines.kinematic_system.all;
   use disciplines.physical_constants.all;
   use disciplines.electromagnetic_system.all;

   entity press_app is
          generic (amp , sigmal_norm , sig-
mat_norm , a , h , pi_44 : real);
          port (terminal T_Pin : fluidic;
                    terminal    T_sigmal    ,
T_sigmat : fluidic;
                    terminal T_dRn , T_dRp :
electrical);
   end entity press_app;

   architecture behav of press_app is
          quantity Pin across flow1 through T_Pin to
fluidic_ground;
          quantity  sigmal  across  flow2  through
T_sigmal to fluidic_ground;
          quantity  sigmat  across  flow3  through
T_sigmat to fluidic_ground;
          quantity  dRn  across  currentn  through
T_dRn to electrical_ground;
          quantity  dRp  across  currentp  through
T_dRp to electrical_ground;
                    begin
                             Pin           ==
amp*sin(2.0*3.14*500.0*now);
                             sigmal == sig-
mal_norm*((a/h)**2)*Pin;
                             sigmat == sig-
mat_norm*((a/h)**2)*Pin;
                             dRn           ==
7.5*pi_44*sigmal;
                             dRp      ==      -
0.46875*pi_44*sigmat;
   end architecture;

   -- ENTITY : PONT DE WHEATSTON --
   library ieee;
   library disciplines;

   use ieee.math_real.all;
   use disciplines.fluidic_system.all;
   use disciplines.kinematic_system.all;
   use disciplines.electromagnetic_system.all;
   use disciplines.physical_constants.all;
   use work.all;

   entity Wheatston is
```

```
        generic (R0 : real := 2000.0);                          quantity dRp across T_dRp to electri-
        port (terminal T_Pin : fluidic ; terminal       cal_ground;
T_V1 , T_V2 : electrical);                                              begin
    end Wheatston;                                                                Pression    :
                                                         entity press_app (behav)    generic map (1000.0 ,
    architecture interne of Wheatston is                 0.0148 , 0.2308 , 0.002 , 0.00003 , 0.0000000014529)
        terminal T_Vin : electrical;
        terminal T_dRn , T_dRp : electrical;                     port map (T_Pin , T_sigmal , T_sigmat ,
        terminal T_sigmal , T_sigmat : fluidic;          T_dRn , T_dRp);
        quantity Vin across i_in through T_Vin to
electrical_ground;                                                       Vin == 2.5;
        quantity Vout across T_V2 to T_V1;                       V1          ==
        quantity V1 across i1 through T_Vin to           i1*(R0*(1.0+dRn));
T_V1;                                                                    V2          ==
        quantity V2 across i2 through T_Vin to           i2*(R0*(1.0+dRp));
T_V2;                                                                    V3          ==
        quantity V3 across i3 through T_V1 to            i3*(R0*(1.0+dRp));
electrical_ground;                                                       V4          ==
        quantity V4 across i4 through T_V2 to            i4*(R0*(1.0+dRn));
electrical_ground;                                           end architecture interne;
        quantity dRn across T_dRn to electri-
cal_ground;
```

6 Conclusions

We were able to show, through this article, the means and the interest in modelling Micro Electro-Mechanical Systems. In this work, we first introduced the VHDL-AMS language with its main advantage, multi-domain simulation with multiple levels of abstraction. This means that the VHDL-AMS provides the ability to model and simulate hybrids components containing electrical parts (analogical or digital) and non-electrical parts (mechanical, thermal, hydraulic, etc.) and all this in a one and single program.

We took as an example, the simulation of a micro-pressure piezoresistive sensor. The sensor collects the mechanical part responsible of the pressure variation detection, and the electrical part responsible of the electronic signal processing. We have simulated MEMS containing two physical domains with different levels of abstraction, and we have achieved very satisfactory results in comparison with other works using multi-domain modelling, but with only one level of abstraction.

Simulation of MEMS by VHDL-AMS saves an enormous computation time since it offers the possibility of using, in one program, models with partial differential equations, analytical models or simple functional models.

References

Arora ND, Hauser JR, Roulston DJ (1982) Electron and hole mobilities in Silicon as a function of concentration and temperature. IEEE Trans Electron Devices 29(2):292

Benmoussa N, Otmani R, Benyoucef B (2014) Mechanical response of a micro silicon membrane: model validation by finite element method. Phys Procedia 55:113–118

Boukabache A (1993) Conception, Modélisation Et Réalisation d'un Capteur de Pression Piézorésistif à faible dérive thermique. Thèse de doctorat, Laboratoire d'analyse et d'architecture des systèmes du CNRS

Dorckel JM, Leturcq P (1981) Carrier mobilities in Silicon semi-empirically related to temperature doping and injection level. Solid State Electron 24:821

Kanda Y (1991) Piezoresistance effect of Silicon. Sens Actuators, p 83

Olszacki M, Maj C, Al Bahri M, Peyrou D, Kerrour F, Pons P, Napieralski A (2008) A multi-domain piezoresistive pressure sensor design tool based on analytical models. In: IEEE 9th International conference on thermal, mechanical and multiphysics simulation and experiments in micro-electronics and micro-systems

Otmani R, Benmoussa N, Benyoucef B (2011) The thermal drift characteristics of piezoresistive pressure sensor. Phys Procedia 21:47–52

Smith CS (1954) Piezoresistance effect in germanium and silicon. Phys Rev 94(1):42–49

Timoshenko SP, Woinowsky-Krieger S (1982) Theory of plates and shells. McGraw Hill, New York

Diagnosis Methods for Mechatronic Systems

Syrine Derbel, Nabih Feki, Florentina Nicolau, Jean Pierre Barbot, Mohamed Slim Abbes, and Mohamed Haddar

Abstract Mechatronic systems are widely used in many industrial applications for their capacity to improve the production performances. However, due to the complexity of these systems, several defects may occur and disrupt the operating of the system. Among these faults, two types can be distinguished: operating faults (e.g., electrical, mechanical, thermal, design defects, . . .) and sensor faults (e.g., bias, gain or drift defects). In this paper, we present a classification of the most frequently used diagnosis methods based on the type of the redundancy: the hardware or the analytical redundancy. Secondly, we propose a new diagnosis technique, called sparse recovery method. This method is based on a dynamical sparse recovery algorithm in order to detect, locate and isolate several faults which can affect the considered system. More precisely, sparse recovery method can be applied to estimate a sparse vector of possible faults based on few system measurements. This diagnosis method is based on system modeling presented in healthy and faulty cases. The good performances of the proposed method are illustrated via an example which can represent a simplified case of mechatronic systems (e.g., gearbox system, asynchronous motor, . . .). The simulation results are obtained via Matlab/Simulink.

Keywords Diagnosis methods · Sparse recovery · Mechatronic systems · Faults detection

1 Introduction

The diagnostic process is an important issue for industries. It consists firstly, to decide a malfunction is present or everything is working properly, and secondly, to

S. Derbel (✉) · F. Nicolau · J. P. Barbot
Quartz Laboratory, ENSEA, Cergy 95014, France
e-mail: syrina.derbel@hotmail.fr

S. Derbel · N. Feki · M. S. Abbes · M. Haddar
Université de Sfax, ENIS, LA2MP, 3038 Sfax, Tunisie

N. Feki
Université de Sousse, ISSATSo, 4003 Sousse, Tunisie

determine, in the former case, the nature as well as the location of the faults. Fault diagnosis can be divided into three areas: fault detection, fault isolation and fault identification. Fault detection is the first and the basic task of the fault diagnosis and is used to check whether there is a malfunction or fault in the system and to determine the time of the fault appearance. Fault isolation consists in identifying the location of faulty components, while fault identification is last step of the fault diagnosis and allows to determine the type, shape and size of the fault (Gao et al. 2015). In order to verify these three tasks, different diagnosis methods either for stationary or non-stationary signals are developed (see, for example Gong and Qiao 2015; Hwang et al. 2010). In this paper, we first give a classification of the most frequently used methods for the diagnostic of mechatronic systems. Then, we present the sparse recovery method which is a novel diagnosis technique used to diagnosis faults in mechatronic systems. The paper is organized as following: Sect. 2 presents the problem statement for the diagnostic of mechatronic systems and gives a general state-space representation for mechatronic systems that will be used when describing the sparse recovery method in Sect. 3. Classification of some diagnosis methods are given in Sect. 3. Section 4 illustrates the good performances of the sparse recovery technique applied for a particular example. Conclusions are given in Sect. 5.

2 Problem Statement

In general, mechatronic systems are complex, composed of at least two interconnected subsystems and can be described by a non linear state-space representation of the form:

$$\begin{cases} \dot{x} = f(x,t) + g(x,t)u, \\ y = h(x), \end{cases} \tag{1}$$

where $x \in \mathbb{R}^n$ is the state vector of the system, $u \in \mathbb{R}^p$ is the input vector and $y \in \mathbb{R}^m$ is the output vector, the vector field f and g, and the function h_i, $1 \leq i \leq m$ are assumed sufficiently smooth. In mechatronic applications, the state vector x includes all states system of all subsystems that are coupled and form the global mechatronic system. For instance, in e.g., Derbel et al. (2019), Fourati et al. (2016, 2017), the global mechatronic system is obtained by interconnecting a mechanical subsystem and an electrical one, thus leading to a global state vector x composed by the degree of freedom of the mechanical subsystem and the currents, fluxes and rotational speed variables associated to the electrical one. Each mechatronic systems can be affected by several defects that can be modeled as following:

$$\begin{cases} \dot{x} = f(x,t) + g(x,t)u + D_1(x,t)w(t), \\ y = h(x) + D_2(t)w(t), \end{cases} \tag{2}$$

where $D_1(x,t)$, $D_2(t)$ are the fault matrices related to, respectively, the operating system and the sensor faults, $w(t)$ represents the possible fault vector. Diagnostic of these faults is a difficult issue for industries and any fault modeled in (2) needs to be

successfully and efficiently detected, localized and identified using a limited set of sensor signals available.

3 Diagnosis Methods

Different classifications of diagnostic methods are proposed in the literature depending on the specific branch that researchers are focused (see, e.g., Hwang et al. 2010; Mouzakitis 2013). In this paper, we distinguish two main areas: the hardware redundancy and the analytical redundancy (see, Fig. 1). The basic concept of the hardware redundancy is to use multiple hardware, as the sensors measurements (for instance, use two or three sensors to measure the same quantity), in order to analysis the same information and to diagnose faults. No mathematical model is needed for the hardware redundancy. On the other hand, the analytical redundancy requires the knowledge of specific information given from a mathematical model, signals (frequency, wavelet) information or from a historic system data. Each category is discussed briefly in the following subsections.

3.1 Hardware Redundancy

The key idea of the hardware redundancy is to use several materials in order to measure the same signals. The hardware redundancy deals with the comparison of duplicative signals generated by more than one sensor using algebraic relation between different system variables (see, for example Hwang et al. 2010). The advantage of this method appears in its reliability and its simplicity. On the other hand, this
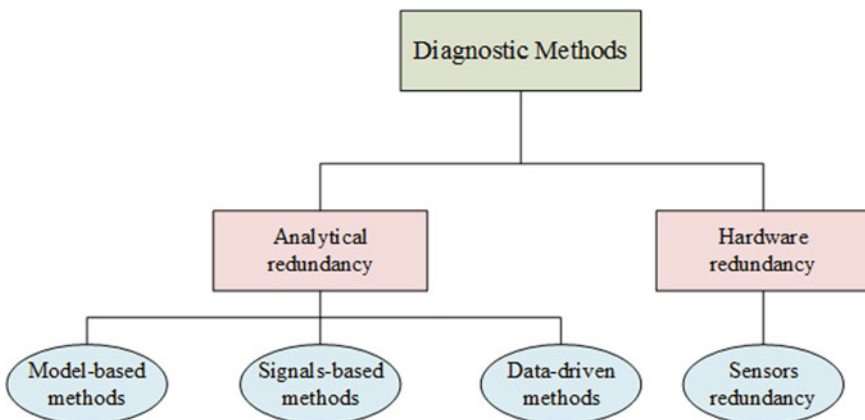

Fig. 1 Classification of diagnostic methods

diagnosis method presents a major setback which is the expensive cost of maintenance due to the extra equipment. An additional space is required to place the extra equipment, hence adding another limit to the use of this method.

3.2 Analytical Redundancy

The analytical redundancy is mainly based on specific information given by local or global modeling of the system. In this article, the analytical redundancy is divided into three categories: model-based methods, signals-based methods and data driven methods (see Fig. 1).

3.2.1 Model-Based Methods

Model-based methods are more effective and less costly compared to the hardware redundancy once because they do not require additional hardware and are based on a mathematical description of the system obtained by developing some physical and fundamental principles. In general, model-based methods allow to compare the available measurements of the actual systems and the model predicted outputs. In this section, the principle of some model-based methods (see Fig. 2) is detailed and divided, with respect to the type of the model, into three categories: deterministic and stochastic diagnostic methods and finally, the sparse recovery method which belongs to model-based diagnosis methods since it requires a mathematical model that describes the system behavior.

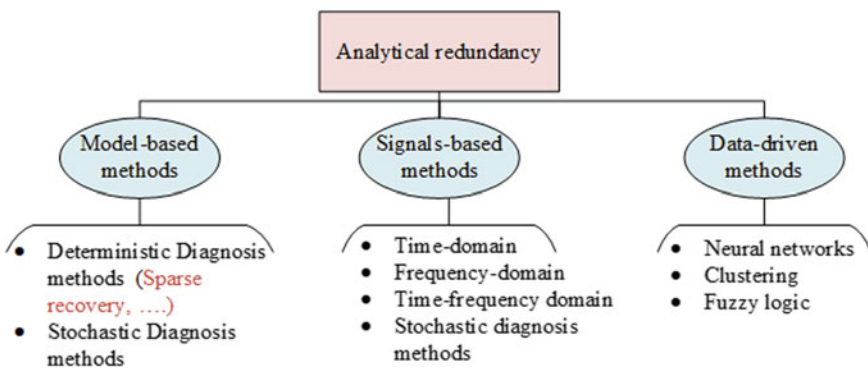(a) *Deterministic diagnosis methods*

Fig. 2 Classification of analytical redundancy methods

The deterministic diagnosis methods are based on a deterministic modeling of the system under consideration. They can be classified in two main areas: parity space and diagnostic based on observers.

- Parity space: The principle of the parity space is to create a residual which is, in general, the difference between the estimated and the actual system outputs. With the help of the residual information, the consistency between this difference is checked: without faults, the residual generated by the party space technique is equal to zero. However, it is non-zero if modeling errors, noises or faults occur in the system. The parity space method can be used either in the time-domain state-space model or in the frequency-domain model. This diagnostic method is applied for many complex model, for example, to estimate faults for a quadrotor unmanned aerial vehicle (Han et al. 2018), for electro-mechanical brake systems (Hwang and Huh 2015), etc. However, in some dynamical systems, due to the lack of the algebraic relations between different system variables, the parity space method becomes unable to diagnosis some specific faults.

- Diagnostic based on observers: Observers play a major role in the deterministic diagnosis methods and, generally, are based on a space-state representation of the system. They can be used to detect, or isolate, or identify the fault. An important issue of the diagnosis methods based on observers is the choice of the observer gain that must render the residual signals sensible to faults and insensible to disturbances (modeling errors, noises and process disturbances). Eigen structure assignment method is the common approach used to give a design of the gain observers by introducing the left and right eigenstructure methods in order to cancel directly the disturbance (see, for more details, Gao et al. 2015; Odofin et al. 2018). Residual generation using unknown input observers is a diagnosis method that gives a state estimation of the system by decoupling the unknown input related to the disturbances. It allows, in particular, to isolate the fault (see, for more details, Edwards et al. (2000) and e.g., Alhelou et al. (2018), Gao et al. (2015) for the application of this method). Concerning the fault identification, many types of observers are developed (for instance, adaptive observers (Rodrigues et al. 2015), sliding mode observers (Barbot et al. 1996), proportional integral observer (Youssef et al. 2017), etc.). The main idea of these observers is that, in the modeling system, the considered faults are implemented as additional states and thus, the global extended state vector (including the fault and original signals) will be estimated. The combination of different observers types has become an important topic of research and is used in order to detect, locate and identify several faults (e.g., Rahme and Meskin 2015; Chen et al. 2016; Derbel et al. 2019).

- Sparse recovery method: Sparse recovery method is a new technique used to detect, isolate and identify faults in dynamical systems. It is based on system modeling, in particular, on the state-space representation. The unknown inputs of the system (faults, disturbances, attacks) are reconstructed under the condition that only restreint number of a long list of possible unknown inputs are detected. Some other theoretical conditions must be verified in order to, effectively, diagnosis faults (see Nateghi et al. 2018). Sparse recovery method is widely applied in image process-

ing and recently, it has been used as a diagnostic methods to diagnosis dynamical systems (for instance, cyber-attack reconstruction via sparse recovery algorithm for electrical power networks application is developed in Nateghi et al. (2018).

The problem of sparse recovery is an optimization program that minimizes a cost function constructed by leveraging the observation error term $(M - Hw(t))$ and the sparsity inducing term λ (verifying the Restricted Isometry Property, the optimization problem is presented with the norm 1):

$$w^* = \min_{w \in \mathbf{R}^l}\{\frac{1}{2}\|M - Hw(t)\|_2^2 + \lambda\|w(t)\|_1\}. \tag{3}$$

where M corresponds to the observed and available measurements, H is a sensing matrix determined from the fault modeling, and w^* is the estimated fault vector and is the solution of the optimization problem. In order to solve this optimization problem, a dynamical algorithm based on sliding mode techniques is proposed by Yu et al. (2017). In this diagnostic method is applied when the dimension of the unknown vector (faults, attacks) is more greater than the available measurements.

(b) *Stochastic diagnosis methods*

Stochastic diagnosis methods are diagnosis method in which the system modeling is inherently random, and uncertain factors are integrated in the model.

- Kalman filter: The most common stochastic diagnosis method is the residual generation using Kalman filter. The faults are diagnosed by statistical testing of the whiteness, co-variance and mean of the residuals. Several statistical tools are developed in order to test the presence of faults such as the maximum likelihood method, the generalized likelihood ration, etc. (see Gao et al. (2015), for more information). Kalman filter has been modified in many research works in order to improve the accuracy of the stochastic approximation [unscented Kalman filter (Sepasi and Sassani 2010)], to consider the nonlinear systems [extended Kalman filter (Foo et al. 2013)].
- Parameter estimation: Parameter estimation is another stochastic diagnosis method which considers that the presence of fault leads to a change in the system parameters (for example, of the space matrix in the space-state representation in case of linear systems). The basic structure in healthy state is known and compared to the estimated parameters methods in order to obtain fault information (see, for example, Bachir et al. 2006).

Model-based methods are effective diagnosis methods that require to have a large knowledge firstly, of the system modeling (the physical laws) in order to obtain accurate model and, secondly, of the system behavior in order to analyze the effect of the fault in the system operating. Complementary to model-based methods, taking into account some frequency characteristics (frequency meshing, supply)is also an essential tool to obtain an accurate system knowledge and thus an optimal fault diag-

nosis. Consequently, signals-based methods have been introducing and can include some model-based diagnosis methods (stochastic diagnosis methods).

3.2.2 Signals-Based Methods

Signal-based methods depend on the measured signals which contain the fault characteristics. They are divided into three areas: time-domain methods, frequency-domain methods and time-frequency methods.

- Time-domain methods: Time-domain methods are the basic diagnosis methods based on the extraction of time-domain characteristics of the measured signals. The most common time-domain methods are: root-mean-square, crest factor, absolute value, kutosis, etc. These diagnostic methods are widely used in industrial application in order to detect faults (e.g., Tian et al. 2015).
- Frequency-domain methods: Frequency-domain methods are used to detect the abnormality by using the spectrum analysis tools. The Fast Fourier Transform (FFT) is the most common diagnosis method and aims firstly, to extract the fault indication from the vibration measured on the system and secondly, to analyze the frequency characteristics and the amplitude of the defect using spectrum techniques. Though the FFT is a very important tool for frequency analysis of stationary signals, it cannot illustrate the change in the frequency spectra for a non-stationary signal (Gong and Qiao 2015). Therefore, FFT cannot reveal the hidden fault information in a non-stationary signals. For specific cases, the spectrum is not always clear and does not contain enough information. In those cases, another method, called cepstral analysis, is used. It deals with the identification of the damage in the situation of the combined effects of harmonics. The spectral analysis is used for many industrial applications such as diagnostic and analysis of the behavior of electric motors and electronic systems (Sonavane and Jadhav 2015), as well as of the wind behavior (Gayatri and Sekhar 2018).
- Time-frequency methods: Time-frequency methods are used in general to analyze non-stationary signals. They aim to identify the frequency characteristic of signals and to extract their time variant features which can be an effective tool for diagnostic. The most common time-frequency methods are the short-time-Fourier Transform, wavelet Transform, Hilbert Transform. For instance, In Cao et al. (2016), Burriel-Valencia et al. (2017), the time-frequency methods are applied in order to diagnosis faults in dynamical systems working in transient state.
- Independent component analysis: Recently, many researchers apply independent component analysis in order to diagnose several faults (Taktak et al. 2012; Hassen et al. 2019). It is a on-line diagnostic method that allows to estimate, locate and identify the defects. This diagnostic method is based on knowing of the dynamical signals responses of the studied system which can be collected by sensors (e.g., accelerometers, encoder optical) or are computed numerically. The princi-

ple of the independent component analysis is based on blind source separation. The blind source separation (BSS) technique is an emerging separation technique which allows to recover a finite set of unknown signals (sources) from a finite set of observed signals recorded by sensors (measurements) which receive a combination of source signals without any knowledge about the sources. Thus, independent component analysis gathers the original sources knowing only the observed signals, which contain a mixture of these signals. This method is applied when the number of estimated sources (faults) is equal to the number of the available signals. The independent component analysis is applied in order to estimate the road profile of the full vehicle model in Hassen et al. (2019) and to diagnose faults in the induction motor (Pöyhönen et al. 2003).

Signals-based methods require a large frequency knowledge which is the essential tool for the diagnostic of mechatronic systems, in particular. This category of diagnosis methods allows to analyze the system behavior (with and without faults) when the mathematical modeling is not available. Thus, the frequency characteristics can also be considered as important information for the data-driven methods which do not require a mathematical model, but describe the process behavior based on the available empirical or experiential information given by the systems sensors and/or the human operator.

3.2.3   Data-Driven Methods

Data-driven methods do not require a mathematical modeling. They are based on the residual generation obtained from the measured inputs to the measured outputs of the system. Fuzzy logic, neural networks, and clustering are the most common diagnosis methods among the data driven methods.

- Fuzzy logic: Fuzzy logic is a mathematical method that solves different simulated problems based only on the inputs and the outputs of the system. Fuzzy logic is able to give results in the form of recommendations for a specific interval of the states using a knowledge base including data (Adhikari et al. 2016).
- Neural networks: Neural networks are intelligent systems inspired from biological neural networks and are mostly suited for faults diagnosis in nonlinear systems. Neural networks give a mapping between the inputs and the outputs of the system

and form an associate memory that recovers the appropriate output when presented with an unseen input. For instance, this diagnostic method is applied in Er-raoudi et al. (2016) in order to detect gear faults.

4 Example

In this section, we apply the sparse recovery method to an example affected by six defects with only three sensor measurements. This example is a simplified case of mechatronic systems. In general, mechatronic systems are modeled using some physical and fundamental principles and in the state-space representation, the state vector represents all system variables (for example, currents, displacements, velocities, . . .). The faults modeling depends on the application under consideration and are modeled as disturbances in the system. Consider the following system:

$$
\begin{cases}
\dot{x}_1 = x_2, \\
\dot{x}_2 = -x_1 + d_1 + x_2 d_2 + x_3 d_3 + 1 + d_4, \\
\dot{x}_3 = x_4, \\
\dot{x}_4 = -2x_3 - d_1 + x_4 d_2 + x_3 d_3 + 2, \\
\dot{x}_5 = x_6, \\
\dot{x}_6 = -1.5x_5 + x_6 d_1 + d_2 - d_3 - 1.
\end{cases}
\quad , \quad
\begin{cases}
y_1 = x_1 + d_5, \\
y_2 = x_3 + d_6, \\
y_3 = x_6.
\end{cases}
\quad (4)
$$

where $[x_1, x_2, x_3, x_4, x_5, x_6]^{\mathrm{T}}$ is the state vector, $[y_1, y_2, y_3]^{\mathrm{T}}$ is the measurement vector and $[d_1, d_2, d_3, d_4, d_5, d_6]^{\mathrm{T}}$ is the fault vector including system and sensor faults. Notice that in this example, we respect the condition that the number of faults is more greater than the number of the sensor measurements. In order to verify all theoretical conditions of the sparse recovery method, the sensor faults are assumed constant. Simulation results are carried out via Matlab Simulink (Euler). The introduced faults in this example can represent some mechanical or electrical defects which may affect a mechatronic system (for example, demagnetization, inter-turn short circuit, dip fault voltage, eccentricity, . . .). For this reason, different signals type of possible faults are introduced (constant and variable defects).

Figure 3a represents the case when the system faults are constant and shows that the estimated faults $\hat{d}_1$ and $\hat{d}_2$ given by the sparse recovery method converge accurately to their real values. In Fig. 3b sinusoidal faults, which can represent for example an eccentricity defect for gearbox, are introduced and are detected via the sparse recovery technique. The estimated faults $\hat{d}_3$ and $\hat{d}_4$ coincide with the real fault quantities. Finally, sensor fault $\hat{d}_5$ and $\hat{d}_6$ are detected in Fig. 4. This example illustrates the good performances of the sparse recovery to detect the presence of several faults. Then, since the frequency characteristics of mechantronic systems are often known, we can use them to localize and identify different faults detected by the sparse recovery method.
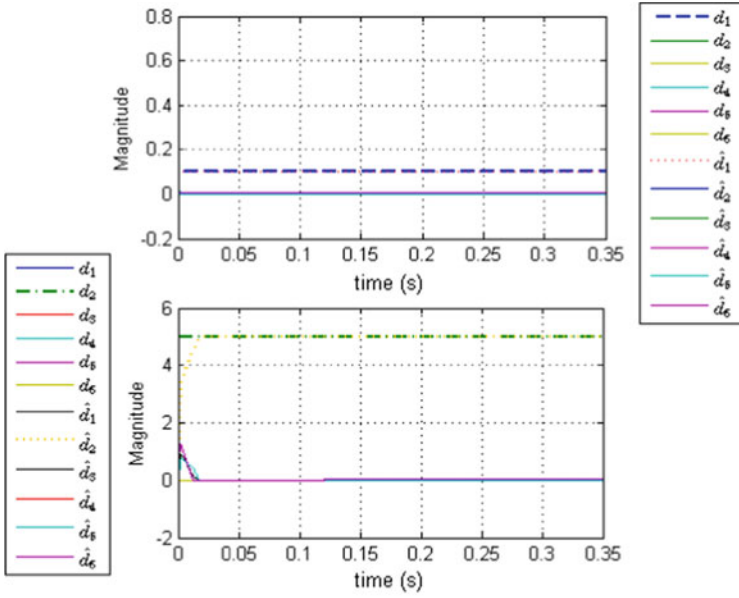
(a) Constant system faults d_1 and d_2
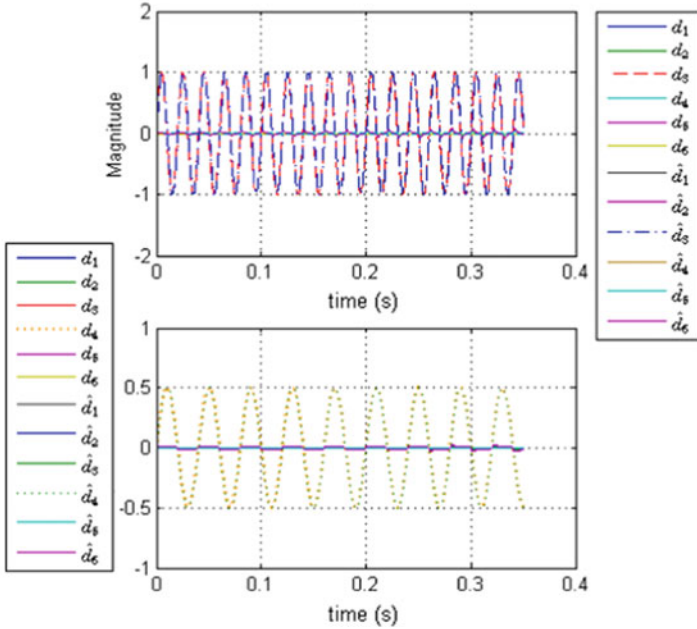
(b) Sinusoidal system faults d_3 and d_4
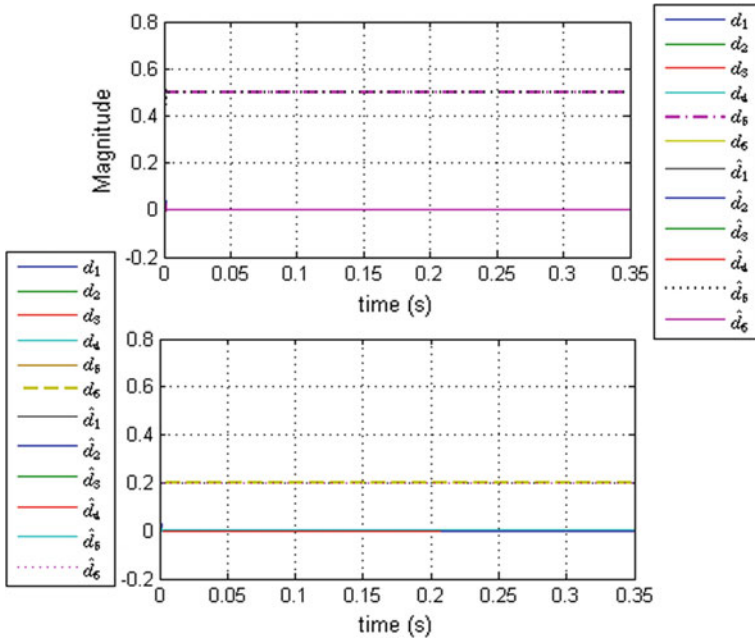
Fig. 3 System faults

Fig. 4 Sensor faults d_5 and d_6

5 Conclusion

In this paper, a classification of some diagnosis methods of mechatronic systems is presented. The introduction of a new diagnosis technique, called sparse recovery, is developed. In order to illustrate the good performances of the proposed method, an example, which can represent a simplified case of mechatronic systems, is studied with presence of different signal faults. Sparse recovery method is applied when the number of possible faults is more greater than the number of sensor measurements and only few of them can occur simultaneously. This point can be considered as a limitation of this method, but, in mechatronic and dynamical systems, the presence of more than one fault disturbs largely the system operating. Thus, it is suitably to combine different diagnosis methods in order to obtain a perfect diagnostic and to take the good decision to the maintenance phase. In our future works, we will apply this diagnosis technique to detect, locate and identify mechanical faults presented in gear power transmission.

References

Adhikari S, Sinha N, Dorendrajit T (2016) Fuzzy logic based on-line fault detection and classification in transmission line. SpringerPlus 5(1):1002

Alhelou HH, Golshan MH, Askari-Marnani J (2018) Robust sensor fault detection and isolation scheme for interconnected smart power systems in presence of RER and EVs using unknown input observer. Int J Electr Power Energy Syst 99:682–694

Bachir S, Tnani S, Trigeassou J-C, Champenois G (2006) Diagnosis by parameter estimation of stator and rotor faults occurring in induction machines. IEEE Trans Industr Electron 53(3):963–973

Barbot J-P, Boukhobza T, Djemai M (1996) Sliding mode observer for triangular input form. In: Proceedings of 35th IEEE conference on decision and control, vol 2, pp 1489–1490

Burriel-Valencia J, Puche-Panadero R, Martinez-Roman J, Sapena-Bano A, Pineda-Sanchez M (2017) Short-frequency fourier transform for fault diagnosis of induction machines working in transient regime. IEEE Trans Instrum Meas 66(3):432–440

Cao H, Fan F, Zhou K, He Z (2016) Wheel-bearing fault diagnosis of trains using empirical wavelet transform. Measurement 82:439–449

Chen F, Zhang K, Jiang B, Wen C (2016) Adaptive sliding mode observer-based robust fault reconstruction for a helicopter with actuator fault. Asian J Control 18(4):1558–1565

Derbel S, Feki N, Barbot JP, Nicolau F, Abbes MS, Haddar M (2019) Application of homogeneous observers with variable exponent to a mechatronic system. Proc Inst Mech Eng Part C J Mech Eng Sci

Derbel S, Feki N, Barbot JP, Nicolau F, Abbes MS, Haddar M (2019b) Electro-mechanical system control based on observers (book chapter). In: Applied condition monitoring, vol 13, pp 101–110

Edwards C, Spurgeon SK, Patton RJ (2000) Sliding mode observers for fault detection and isolation. Automatica 36(4):541–553

Er-raoudi M, Diany M, Aissaoui H, Mabrouki M (2016) Gear fault detection using artificial neural networks with discrete wavelet transform and principal component analysis. J Mech Eng Sci 10:2016–2029

Foo GHB, Zhang X, Vilathgamuwa DM (2013) A sensor fault detection and isolation method in interior permanent-magnet synchronous motor drives based on an extended kalman filter. IEEE Trans Industr Electron 60(8):3485–3495

Fourati A, Bourdon A, Feki N, Rémond D, Chaari F, Haddar M (2017) Angular-based modeling of induction motors for monitoring. J Sound Vibr 395:371–392

Fourati A, Feki N, Bourdon A, Rémond D, Chaari F, Haddar M (2016) Electrical modeling for faults detection based on motor current signal analysis and angular approach (book chapter). In: Applied condition monitoring, vol 4, pp 15–25

Gao Z, Cecati C, Ding SX (2015) A survey of fault diagnosis and fault-tolerant techniques-part I: Fault diagnosis with model-based and signal-based approaches. IEEE Trans Industr Electron 62(6):3757–3767

Gao Z, Liu X, Chen MZ (2015) Unknown input observer-based robust fault estimation for systems corrupted by partially decoupled disturbances. IEEE Trans Industr Electron 63(4):2537–2547

Gayatri C, Sekhar AS (2018) Dynamic analysis and characterization of two stage epicyclic gear box in wind turbine drive train. AIP Conf Proc 2044(1):020018

Gong X, Qiao W (2015) Current-based mechanical fault detection for direct-drive wind turbines via synchronous sampling and impulse detection. IEEE Trans Industr Electron 62(3):1693–1702

Han W, Wang Z, Shen Y (2018) Fault estimation for a quadrotor unmanned aerial vehicle by integrating the parity space approach with recursive least squares. Proc Inst Mech Eng Part G J Aerosp Eng 232(4):783–796

Hassen DB, Miladi M, Abbes MS, Baslamisli SC, Chaari F, Haddar M (2019) Road profile estimation using the dynamic responses of the full vehicle model. Appl Acoust 147:87–99. In: Special issue on design and modelling of mechanical Systems conference CMSM'2017

Hwang I, Kim S, Kim Y, Seah CE (2010) A survey of fault detection, isolation, and reconfiguration methods. IEEE Trans Control Syst Technol 18(3):636–653

Hwang W, Huh K (2015) Fault detection and estimation for electromechanical brake systems using parity space approach. J Dyn Syst Meas Control 137(1):014504

Mouzakitis A (2013) Classification of fault diagnosis methods for control systems. Meas Control 46(10):303–308

Nateghi S, Shtessel Y., Barbot J-P, Zheng G, Yu L (2018), Cyber-attack reconstruction via sliding mode differentiation and sparse recovery algorithm: electrical power networks application. In: 2018 15th International workshop on variable structure systems (VSS), pp 285–290

Odofin S, Bentley E, Aikhuele D (2018) Robust fault estimation for wind turbine energy via hybrid systems. Renew Energy 120:289–299

Pöyhönen S, Jover P, Hyötyniemi H (2003) Independent component analysis of vibrations for fault diagnosis of an induction motor. In: Proceedings of IASTED international conference circuits, signals, and systems, Citeseer, pp 19–21

Rahme S, Meskin N (2015) Adaptive sliding mode observer for sensor fault diagnosis of an industrial gas turbine. Control Eng Pract 38:57–74

Rodrigues M, Hamdi H, Theilliol D, Mechmeche C, BenHadj Braiek N (2015) Actuator fault estimation based adaptive polytopic observer for a class of lpv descriptor systems. Int J Robust Nonlinear Control 25(5):673–688

Sepasi M, Sassani F (2010) On-line fault diagnosis of hydraulic systems using unscented kalman filter. Int J Control Autom Syst 8(1):149–156

Sonavane SR, Jadhav HT (2015) Evolution of wind energy generation system using DFIG and FFT analysis. In: 2015 IEEE 9th International conference on intelligent systems and control (ISCO), pp 1–5

Taktak M, Tounsi D, Akrout A, Abbes MS, Haddar M (2012) One stage spur gear transmission crankcase diagnosis using the independent components method. Int J Veh Noise Vibr 8:387–400

Tian J, Morillo C, Azarian MH, Pecht M (2015) Motor bearing fault detection using spectral kurtosis-based feature extraction coupled with k-nearest neighbor distance analysis. IEEE Trans Industr Electron 63(3):1793–1803

Youssef T, Chadli M, Karimi HR, Wang R (2017) Actuator and sensor faults estimation based on proportional integral observer for ts fuzzy model. J Franklin Inst 354(6):2524–2542

Yu L, Zheng G, Barbot J (2017) Dynamical sparse recovery with finite-time convergence. IEEE Trans Signal Process 65(23):6146–6157

Mechatronics Iterative Design for Robots Multi-agent Integration

Thierry Soriano, Valentin Gies, Anh Hoang Pham, and Ngo Van Hien

Abstract Robot design is a very active part of industrial activity. Mechatronics 4.0 takes its place there. For the realization of complex tasks, one often calls upon the multi-agent design of robots. Several system engineering approaches are possible and the one using rapid prototypes is among the most encountered. Iterative cycles can be used for the design of the software and also the hardware, and they allow to quickly reduce the risks of the project. Two representations of iterative cycles are frequently used. The first is of divergent type and emphasizes the means and the volume of the project. The second is of convergent type, with focus on the technical objective to be achieved. Two examples of experiments will illustrate these points of view. The first concerns a competition for robot soccer players. This experiment highlights the creation of successive software and hardware prototypes for which the emphasis has been placed here on two mechanical sub-systems. The cost of materials in rapid prototyping and the time available before the competition are important on this project. The second experimentation deals with a swarm of autonomous underwater vehicles for surveillance. The scientific and technical objectives as well as the choice of modeling methodology without continuity are essential here for iterative design.

Keywords Mechatronics · Robot · Iterative engineering cycle · Prototyping · ROS

T. Soriano (✉)
Seatech Engineering School, Toulon University, Toulon, France
e-mail: thierry.soriano@univ-tln.fr

V. Gies
Laboratory IM2NP, Toulon University, Toulon, France

A. H. Pham
Laboratory COSMER, Toulon University, Toulon, France

N. Van Hien
Hanoi University of Technology, Hanoi, Vietnam

1 Introduction

Multi-agent robotics projects in an open source environment use rapidly evolving emerging mechatronic technologies that must be integrated into a methodological engineering framework. Classical V cycle is not always the best appropriate approach because it is necessary to have early means to validate preconception or architectural choices, and then iterative cycle approaches are frequently encountered.

When we decide to adopt an iterative approach to progressively validate the solutions, we can use two types of cycles in the iterative methods. In one side, an convergent cycle focuses with the objective of the main requirement of the specifications through successive virtual prototypes and in the other side, a divergent cycle reveals an increasing implementation of means and time towards the final product through virtual prototypes but also real prototype.

1.1 Convergent Spiral Type

A popular first way of representing the iterative design process is a convergent spiral design towards a center (Fig. 1). The distance to the center indicates that the project is gradually approaching a goal through successive prototypes. This supposes that a large number of prototypes can be envisaged and therefore that the time period of realization and the material cost of a prototype is not an essential problem in the current project.

This also assumes when the goal is clearly marked; if the main function of the system under development could be identified as unique and quantifiable, then we are in the ideal context of application of this scheme.

Fig. 1 Convergent spiral engineering cycle (Douglass 2002)
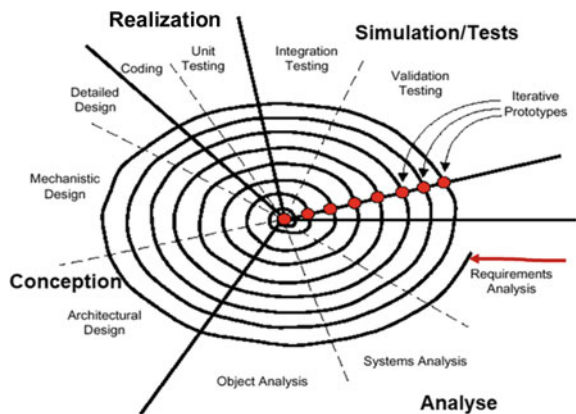
A typical case of context can be a system, or a subsystem in the case of SoS (Systems of Systems) essentially software, with a known metric (response time, accuracy).

The experiment developed further on the submarine robot collaboration program falls into this category.

1.2 Divergent Spiral Type

If we adopt an iterative cyclic engineering method, a second basic representation scheme of activity and process representation is the divergent spiral (Fig. 2).

This diagram shows the production of successive prototypes. It highlights the cumulative costs of the developing system, time and material costs. The objectives coming from the specifications can be multiple.

If several main functions are contained in the specifications, as is often the case for mechatronic systems that achieve a high level of integration of functions thanks to the programmed intelligence, the prototype suite can follow a progressive list of functions from the most critical in terms of industrial or technical risk in innovative design to the functions of a routine design.

This schema is not exclusive of the first model represented previously. In the case of a single function suitably quantified, and in innovative design, the realization of which will use particularly innovative models and algorithms, several prototypes are
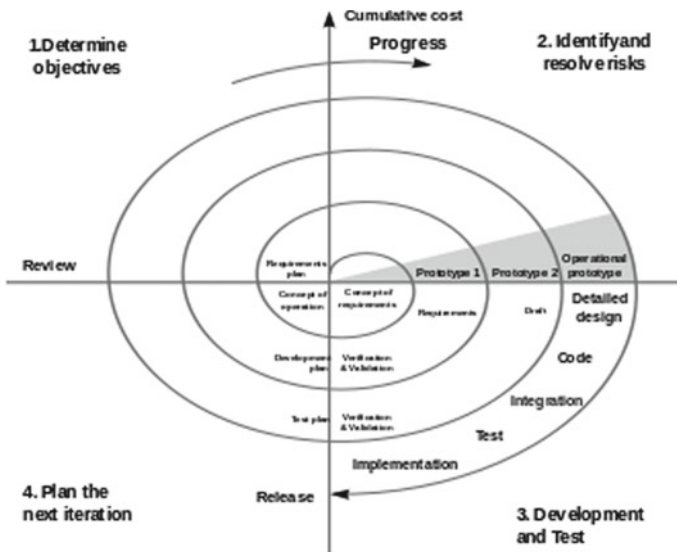

Fig. 2 Divergent spiral engineering cycle (Vickoff 2019; Boehm 1988)

necessary to approach performance objectives, and an accumulation of costs is also useful for the project and risk management.

1.3 Robot Multi-agent Experiments

Subsequently, two engineering experiments using iterative approaches will be described. The type of application concerns multi-agent collaborative robotics in proof of concept context i.e. unitary laboratory series. This type of project often cannot rely on heavy investments in machinery or software licenses. It is therefore in an open source environment for the software, and in manufacturing by addition of material processing, where a significant part of the realization takes place.

The first experiment concerns the design of a group of robots for Robocup (Gies and Soriano 2019) football player's competition. It was adopted a bottom-up approach by first designing a robot and its software and then return to the software related to the training.

The second experiment concerns the design of a group of autonomous submarine robots. The primary goal was in this case to design the training control algorithm.

2 Iterative Design of Prototype Robots

The University of Toulon participated successfully for years in the competition of robotics. The ambition is to participate in middle size league at Robocup global robotics competition whose events are based on a football match on a large field.

A great deal of experience and many innovations in the mechanical design and software of prototype robots have been accumulated in recent years. These robots have as common characteristics to be designed in a limited time, with a cost under control and specifications each time different. The production of these unique competition robots systematically uses mechanical, electronic and software technologies and in this set, the most recent technological advances are included.

In the same way for the choice of speed or imaging sensors, it is a question every year to turn oneself towards the most powerful sensors on the market while remaining at an acceptable cost, whether to put LIDAR laser detectors or a high-resolution fast camera. Electronic design and manufacturing primarily uses open source Arduino and Raspberry boards, which are configured and programmed in C, C#, Java.

In cases where the assembly of electronic cards of the market is not enough, and it is frequently the case at this level of innovation, the cards are designed and manufactured on site thanks to the skills research platform of Toulon University. From the point of view of embedded intelligence, all the most advanced models and algorithms are implemented (multi-variable servo-control, robust control by extended Kalmann filters, advanced decision algorithms from artificial intelligence (genetic

algorithms, neurons networks) and collective intelligence since the robots compete in teams of three in this ball game (Fig. 3).

From the point of view of system engineering, it can be seen that each year a development cycle is implemented, with a non-explicit method of mechanical design and software of prototype robots with constraints of limited time (specifications in September for a prototype in May following), a cost under control and specifications each time different, precise and not subject to evolutions. Many tasks are done in parallel, project milestones and deliverable definitions are rare. If we cannot speak here of industrial risk we see that the risks of failure are important, often appear during the competition and are poorly mastered.

In this highly constrained environment, the university team has accumulated a great deal of untrammeled expertise in a rigorous and transmissible way.

Two developed subsystem are presented here

Subsystem 1:

Objective: design of shooting sub system for shooting function.
Context: no experience of this task, innovative design, no possibility of global simulation of refined models.
Approach: general design under Solidworks, simulation of electrical model under Simulink, FE analysis and optimization under FEMM and then intensive rapid prototyping, several prototypes with 3D printer.
Cumulative cost for several virtual prototypes and several real prototypes: plastic materials, coil, and metal parts (Fig. 4).

Subsystem 2:

Objective: Design of sub system for goal function.
Context: no experience of this task, innovative design, no possibility of global simulation of refined models.
Approach: general design under Solidworks, simulation and FE analysis and then intensive rapid prototyping, several prototypes with 3D printer.

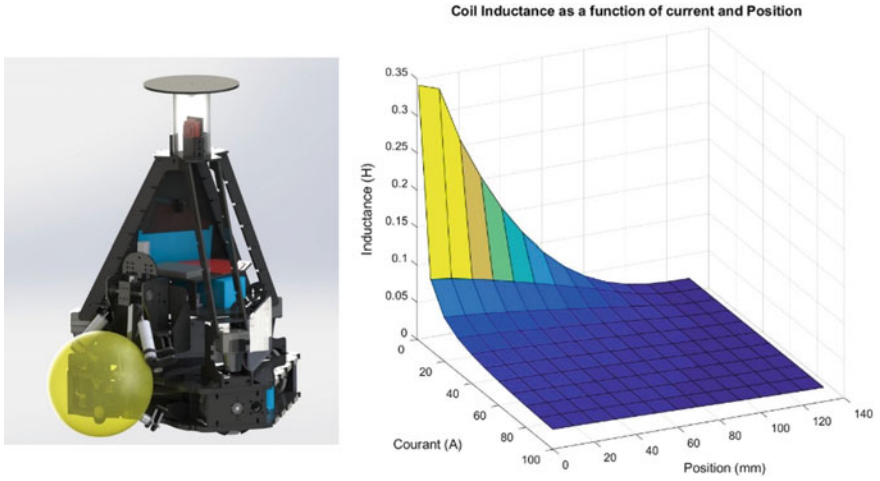**Fig. 3** Robocup robots competition (Robocup https://2019.robocup.org)

Fig. 4   Shooting subsystem prototype and coil analysis (Gies and Soriano 2019)
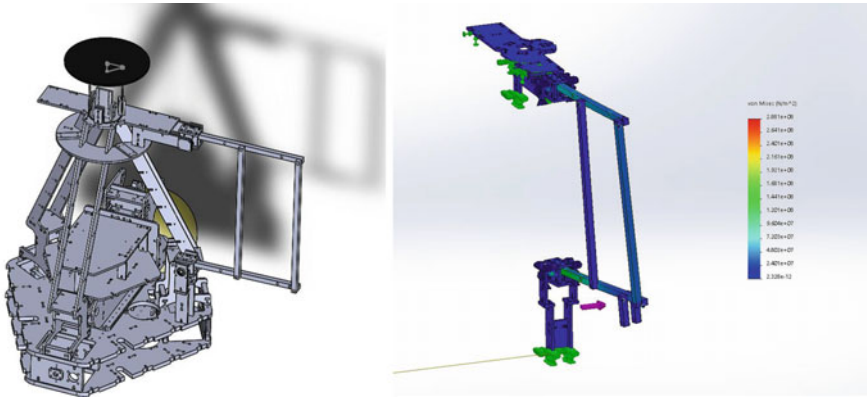

Fig. 5   Goal sub system and FE analysis

Cumulative costs for several virtual prototypes and several real prototypes: time, plastic materials, coil, and metal parts (Fig. 5).

3 Iterative Design of Formation Control of Underwater Robots

The BlueROV[1] (Fig. 6) is the open source and low-cost platform used. Figure 7 shows out the components of BlueROV-1 with the control architecture. The BlueROV frame and thrusters were included in a package from Blue Robotics. In addition to the BlueROV frame, a Raspberry Pi was used as an on-board computer (high-level control) and an HKPilot Mega 2.7 was used as an input/output unit (low-level control).The BlueROV's I/O consists of an HKPilot Mega 2.7 which is based on Ardupilot Mega. The HKPilot Mega 2.7 has the following on chip sensors: Magnetometer—HMC5883L, Barometer—MS5611-01BA, inertial measurement unit (IMU)—MPU6000. An external pressure sensor MS5837-30BA which was encased in a
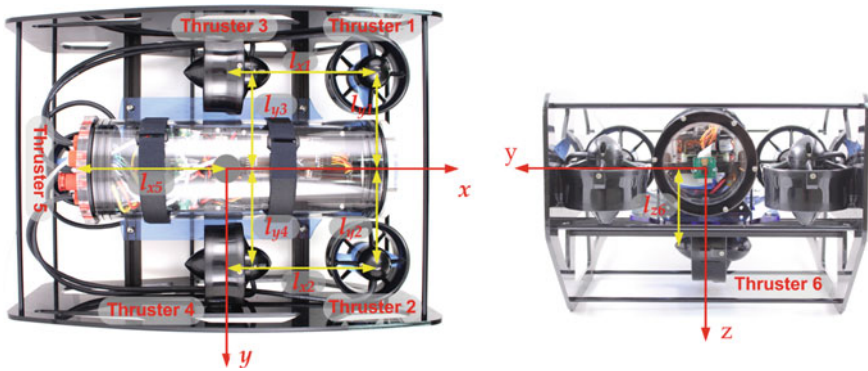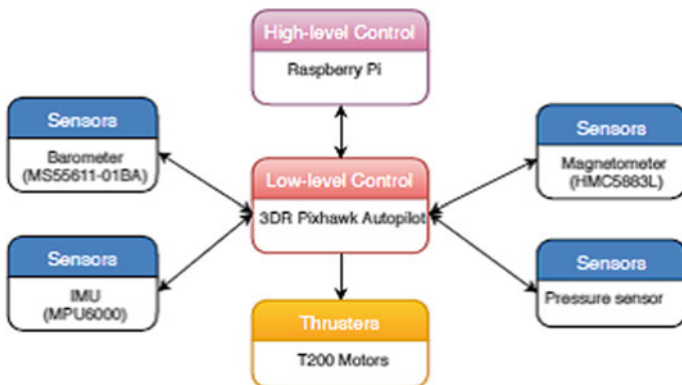

Fig. 6 Bluerove underwater robot

Fig. 7 Physical structure of the existing system

---

[1]Bluerove2 https://bluerobotics.com/store/rov/bluerov/bluerov2.

watertight case by Blue Robotics was connected to the HKPilot Mega 2.7 by I2C. The HKPilot Mega2.7 also controls the six ESCs.

The key points of the software project are:

System: Group of autonomous submarine vehicles AUV.
Context: There are three existing Bluerove autonomous systems with Raspberry embedded card under ROS environment.[2] No experience and innovative design.
Objective: Design of consensus control programs for the group, in order to track a trajectory and avoid obstacles (Fig. 8).
Approach: Design of algorithms more and more complex from linear cases (Pham et al. 2018) to nonlinear real robust models, test neuronal network (Fig. 9), intensive 3D virtual prototyping under ROS/ Gazebo.
Cost: Cumulative costs for several virtual prototypes, essentially time consumption.
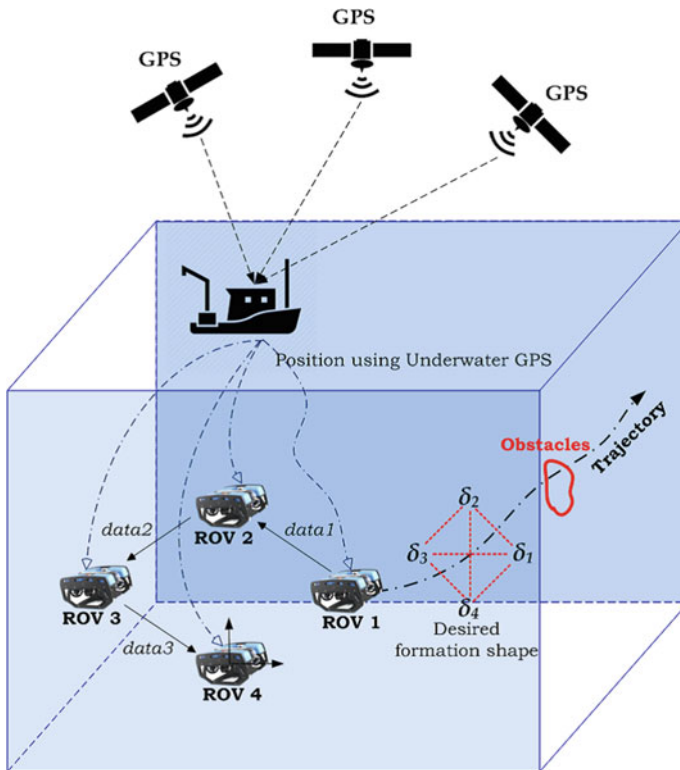
Fig. 8 Formation of underwater robot

[2]ROS Robot Operating System https://www.ros.org/.

Fig. 9 Four successive software prototypes with discontinuities in technology

4 Conclusion

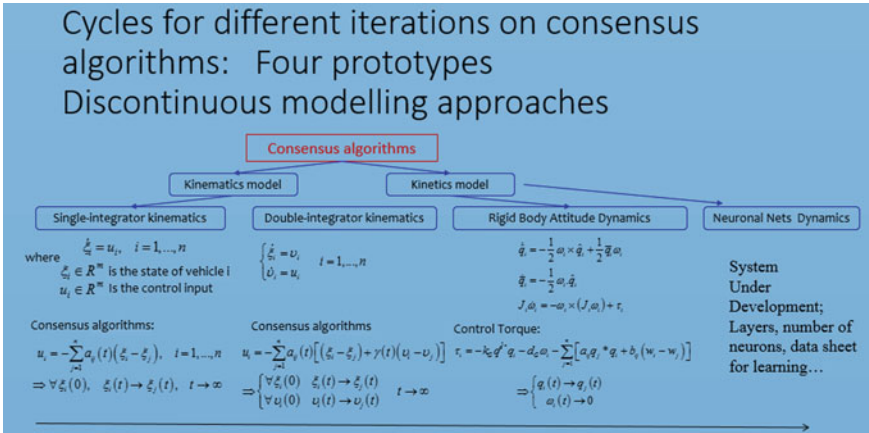The interest of iterative prototyping in the design of mechatronic systems in the software part or the hardware part, was discussed. At the same time as the objectives are getting closer, the costs are increasing and there is an interest in a graphic representation of these evolutions. Iterative prototyping in road design sees costs evolve steadily as new main functions of the specifications are integrated, as in the case of robots from the Robocup competition.

In the case of a single main function as in the case for the formation of submarine robots with a discontinuity of technology, and with the change of technology from an algebraic model to a neural network model the cumulative cost could suffer a strong non-linearity. This type of nonlinear quantification does not yet appear in the proposed representations (Fig. 10). Despite the existence of certain results (Warniez 2015), the metrics associated with cycles and prototypes should be developed.
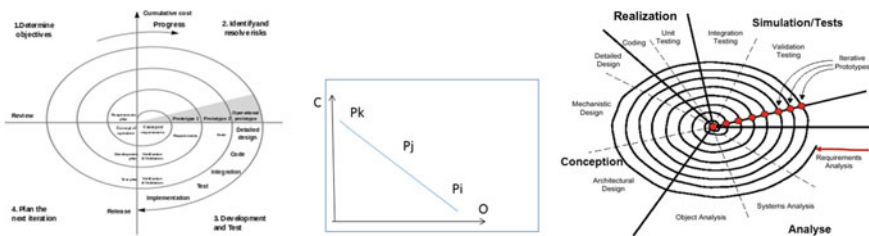

Fig. 10 Iterative cycles and linear representation objective/cost

References

Boehm BW (1988) A spiral model of software development and enhancement. Computer 21(5)

Douglass BP (2002) Real time design patterns. Addison-Wesley

Gies V, Soriano T (2019) Modeling and optimization of an indirect coil gun for launching non-magnetic projectiles. Actuators 8:39. https://doi.org/10.3390/act8020039

Liu Y, Huang P, Zhang F, Zhao Y (2018) Distributed formation control using artificial potentials and neural network for constrained multiagent systems. IEEE Trans Control Syst Technol 1–8. https://doi.org/10.1109/tcst.2018.2884226

Pham HA, Soriano T, Ngo VH (2018) Integrated scenarios of formation tracking and collision avoidance of multi-vehicles. In: 13th annual conference on system of systems engineering (SoSE), Paris, France. https://doi.org/10.1109/sysose.2018.8428730

Vickoff JP (2019) Méthode Agile. Agile-entreprise.com

Warniez A (2015) Identification de métriques pour la conception de systèmes mécatroniques. Thèse de l'Ecole Centrale de Paris

Dimensioning of an Electromagnetic Spindle with Interval Computation Technique

A. Guizani, H. Trabelsi, M. Barkallah, M. Hammadi, J. Y. Choley, and M. Haddar

Abstract High Speed Machining (HSM) is a new technology used to reduce the time and cost of producing parts in several sectors. Among the main components of the HSM is the spindle. It is usually supported by Active Magnetic Bearings (AMBs), in order to achieve high speeds without affecting the dynamic characteristics of the machine. In this paper, an electromagnetic spindle supported by two AMBs is modeled and simulated using the interval calculation technique in order to assure successfully the preliminary design process. The behavior of the system is evaluated and studied with the consideration of uncertainty. The uncertainties are taken into account for the different design parameters that define the dynamic model of the spindle.

Keywords Electro-spindle · Interval computation technique · Dynamic behavior

A. Guizani (✉) · H. Trabelsi · M. Barkallah · M. Haddar
Mechanics, Modeling and Production Research Laboratory,
National Engineering School of Sfax, 3038 Sfax, Tunisia
e-mail: amir.guizani@live.fr

H. Trabelsi
e-mail: hassen.trabelsi@outlook.fr

M. Barkallah
e-mail: bark_maher@yahoo.fr

M. Haddar
e-mail: mohamed.haddar@enis.rnu.tn

M. Hammadi · J. Y. Choley
QUARTZ EA7393, SUPMECA-Paris, 3 rue Fernand Hainaut, 93407 Saint-Ouen, France
e-mail: moncef.hammadi@supmeca.fr

J. Y. Choley
e-mail: jean-yves.choley@supmeca.fr

1   Introduction

In recent years, HSM is considered one of the most popular in the industry of producing of molds and mechanical components. It allows obtaining a variety of complex forms thanks to the wide variety of cutting tools driven by a rotational movement and composed of several cutting edges. Several parameters affect the forces acting on the cutter. Their forecasts and knowledge become necessary in order to adapt the conditions of cutting tools.

The last researches have focused on studying the behavior of the milling spindle with various types of bearings, more particularly AMB, since they have many advantages (Chiba et al. 2005; Knospe 2007; Schweitzer et al. 2009; Tsai and Lee 2011).

Indeed, compared to rolling bearings, Knospe (2007) deduced that AMBs are characterized by a high rotation speed with minimal energy dissipation, a high resistance to shock generated by accidental forces and especially a long life.

Furthermore, Kimman et al. (2010) proposed new techniques of modeling and control of a spindle of a miniature-milling machine supported by two AMBs. They deduced that with higher rotational speeds around 1,50,000 rpm, the machine's operation could improve. To achieve these velocities, it is necessary to optimize the choice of the diameter and the length of the spindle.

Moreover, those results are verified and confirmed by the research work developed in Sawicki et al. (2007) and Gourc et al. (2011). Sawicki et al. (2007) modeled an electromagnetic spindle using the finite element method. Gourc et al. (2011) modeled and studied a spindle rotating at 40,000 rpm and supported by original AMBs.

In addition to the advantages described above, the measurement of force and position can be done using feedback currents and displacement sensors. For example, Auchet et al. (2004) proposed a new technique to determine the values of cutting force by analyzing the AMB command voltage. In order to maximize damping, Knospe and Chen recommend using an additional AMB on the spindle, which offer the possibility to control vibrations of the cutting tool (Knospe 2007; Chen and Knospe 2007). Kyung and Lee (2003) presented, only for conventional machining (low speeds), a spindle stability study with AMB.

In this paper, we have studied the dynamic behavior of an electro-spindle based on the interval calculation method to obtain a set of values for the different design parameters, to avoid making several simulations that can make the system costly or ineffective and to achieve a guaranteed design process.

2   Dimensioning of an Electromagnetic Spindle

In this part, the study of the dynamic behavior of the spindle is based on a new approach considering the two movements of the indeformable and flexible solids.

As shown in Fig. 1, the electro-spindle studied consists of:

Fig. 1 Model of the
electromagnetic spindle
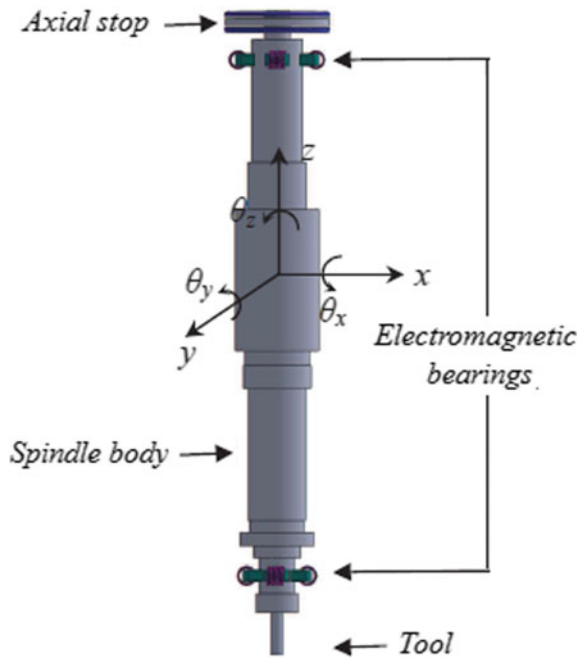
- A spindle body (shaft or rotor),
- Two electromagnetic bearings placed at the top and at the bottom,
- An axial stop.

2.1 Shaft Modeling Approach

The modeling of the shaft is based on the coupling between the small deformations of the elastic movement and those of the rigid movement. The determination of the equation of motion requires the computation of the kinetic energy of a rigid beam as well as the kinetic and potential energies when this one is considered deformable.

Kinetic energy is written in the following form (Trabelsi et al. 2019; Hentati et al. 2013):

$$E_c = \frac{1}{2}\rho A \int_0^L \left[(\dot{X}_A^2 + \dot{Y}_A^2 + \dot{Z}_A^2) + (\dot{U}^2 + \dot{V}^2 + \dot{W}^2) + 2(\dot{U}\dot{Y}_A + \dot{V}\dot{Z}_A) \right] dz$$

$$+ \frac{1}{2}\rho I \int\limits_0^L \left[\begin{array}{l} \left(\dot{\alpha}_x^2 + \dot{\alpha}_y^2 + \dot{\alpha}_z^2\right) + \left(\dot{\theta}_x^2 + \dot{\theta}_y^2 + \dot{\theta}_z^2\right) + 4\Omega\left(\dot{\alpha}_y\alpha_z\right) + 4\Omega\left(\dot{\theta}_y\theta_z\right) \\ + 4\Omega\left(\dot{\alpha}_y\theta_z - \dot{\alpha}_z\theta_y\right) + 2\left(\dot{\alpha}_y\dot{\theta}_y + \dot{\alpha}_z\dot{\theta}_z\right) + 2\Omega^2 \end{array} \right] dz$$

(1)

where $\{U, V, W, \theta_x, \theta_y, \theta_z\}$, $\{\dot{U}, \dot{V}, \dot{W}, \dot{\theta}_x, \dot{\theta}_y, \dot{\theta}_z\}$, $\{X_A, Y_A, Z_A, \alpha_x, \alpha_y, \alpha_z\}$ and $\{\dot{X}_A, \dot{Y}_A, \dot{Z}_A, \dot{\alpha}_x, \dot{\alpha}_y, \dot{\alpha}_z\}$ are the displacements and the velocities corresponding respectively to the elastic movements and to rigid movements.

The displacements $\{U, V, W\}$ are composed of the displacements $\{U_b, V_b, W_b\}$ due to the effect of the bending and displacements $\{U_s, V_s, W_s\}$, which result from the shear effect of the element.

The potential energy is calculated according to the flexion and shear displacements using the following expression:

$$E_p = \frac{1}{2}\int\limits_0^l EI\left(\dot{U}_b^2 + \dot{V}_b^2 + \dot{W}_b^2\right)dx + \frac{1}{2}\int\limits_0^l KGA\left(\dot{U}_s^2 + \dot{V}_s^2 + \dot{W}_s^2\right)dz \quad (2)$$

where A is the section of the element, E is the Young's modulus, G is the shear modulus, K is the shear coefficient, ρ is the density and I is the moment of inertia.

2.2 Modeling of the Electromagnetic Bearings

In this study, the classical electromagnetic bearings configuration was used: two identical bearings are placed at the top and bottom. Each bearing can be composed of two, three or four pairs of electromagnets mounted symmetrically on either side of the two axes x and y in Fig. 2.

For a bearing with four electromagnets, the two components of the force, in the x and y directions, exerted by the electromagnetic bearings can be rewritten in the following form:
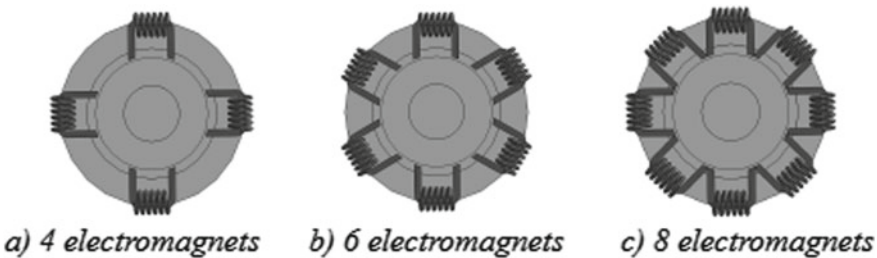

a) 4 electromagnets   b) 6 electromagnets   c) 8 electromagnets

Fig. 2 Electromagnetic bearings model

$$F_{pi} = a \left[\left(\frac{1 - \frac{k_p u_i}{I_0} - \frac{k_d \dot{u}_i}{I_0}}{1 - \frac{u_i}{e_0}} \right)^2 - \left(\frac{1 + \frac{k_p u_i}{I_0} + \frac{k_d \dot{u}_i}{I_0}}{1 + \frac{u_i}{e_0}} \right)^2 \right], \quad i = x, y \qquad (3)$$

where, u_i is the displacement, $\dot{u}_i$ is the velocity, k_d is the derivative gain, k_p is the proportional gain and e_0 is the nominal airgap.

2.3   Determination of the Dynamic Coefficients

The electromagnetic field is modeled by dynamic coefficients, as indicated in Fig. 3 stiffness coefficients that are a function of the displacements and damping coefficients relative to the velocities corresponding to displacements.

The electromagnetic forces along the two directions x and y are put into a matrix form as follows (Bouaziz et al. 2011):

$$\left\{ \begin{array}{c} F_{px} \\ F_{py} \end{array} \right\} = \left[\begin{array}{cc} K_{xx} & K_{xy} \\ K_{yx} & K_{yy} \end{array} \right] \left\{ \begin{array}{c} u_x \\ u_y \end{array} \right\} + \left[\begin{array}{cc} C_{xx} & C_{xy} \\ C_{yx} & C_{yy} \end{array} \right] \left\{ \begin{array}{c} \dot{u}_x \\ \dot{u}_y \end{array} \right\} \qquad (4)$$
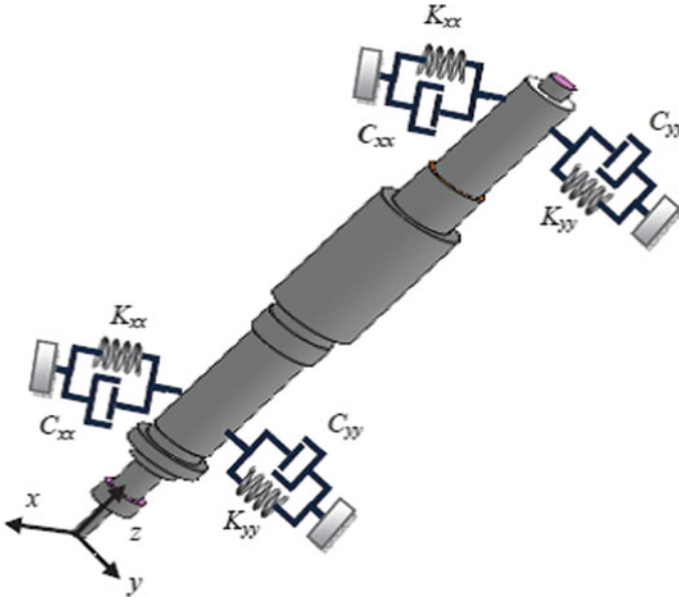

Fig. 3 Modeling of electromagnetic bearings using the stiffness and damping coefficients

2.4 Equation of Movement of the Electromagnetic Spindle

The global motion equation of the electro-spindle is written in the following form (Trabelsi et al. 2019):

$$[M][\ddot{Q}] + ([G] + [D] + [C_b(t)])\{\dot{Q}\} + ([K] + [K_b(t)])\{Q\} = \{F_{c(x,y,z)}(t, \{Q\})\} \tag{5}$$

where:

$[M] = \begin{bmatrix} [M_F] & [M_{RF}] \\ [M_{RF}]^T & [M_R] \end{bmatrix}$: the mass matrix, 'F' and 'R' designate the two movements flexible and rigid;

$\{Q\} = [U_1, V_1, W_1, \theta_{x1}, \theta_{y1}, \theta_{z1}, \ldots, U_i, V_i, W_i, \theta_{xi}, \theta_{yi}, \theta_{zi}, X_A, Y_A, Z_A, \alpha_x, \alpha_y, \alpha_z]^T$: the displacement vector (the degrees of freedom of elastic and rigid movements);

$[G] = 2\Omega \begin{bmatrix} [G_F] & [G_{RF}] \\ -[G_{RF}]^T & [G_R] \end{bmatrix}$: the gyroscopic matrix;

$[D] = \alpha[M] + \beta[K]$: the modal damping matrix;

$[K] = \left(\begin{bmatrix} [K_F] & 0 \\ 0 & 0 \end{bmatrix} - \Omega^2 \begin{bmatrix} [C_F] & 0 \\ 0 & 0 \end{bmatrix} \right)$: the dynamic stiffness matrix;

$\Omega^2 \begin{bmatrix} [C_F] & 0 \\ 0 & 0 \end{bmatrix}$: the terms of centrifugal force;

$[K_b(t)]$ and $[C_b(t)]$: are variable matrices containing the coefficients of stiffness of the electromagnetic bearings;

$F_{c(x,y,z)}(t, \{Q\})$: the vector of the cutting force along x, y and z.

In this part, the necessary parameters that define the dynamic model of the electromagnetic spindle are introduced. Thus, the simulation of the dynamic behavior of the studied system is presented in the following section.

3 Simulation Results Using Interval Computation Technique

Due to the non-linearity of the spindle motion equation, the resolution with uncertainties of this type of system using the Newmark method coupled with Newton-Raphson (Gościniak and Gdawiec 2019; Faroughi and Lee 2015) gave diverging results. Consequently, the choice of parameters with uncertainty (which will be represented using intervals) affects on the convergence of the obtained results. In order to overcome this problem, the objective of this part is to solve the system of differential equations of the electromagnetic spindle with the interval calculation method. The main advantage is to obtain convergent results that reflect the effectiveness of this method. For

**Table 1** Characteristics of the electromagnetic spindle

Variables	Nomenclature	Values	Units
Ω	Rotation speed of the spindle	20,000	tr/m
L	Length of the shaft	651,95	mm
I_r	Moment of inertia	0.11	kg m^2
m	Spindle mass	16,03	kg
E	Young's module	2.11×10^{11}	Pa
ρ	Density	7.85	g/cm^3
D_1	Diameter of element 1	38.1	mm
L_1	Length of element 1	12.7	mm

this, the following uncertainties are introduced in the model to study the dynamic behavior of the spindle with interval:

- 2% on the diameter of element 1
- 2% on the length of element 1

The characteristics of the electromagnetic spindle are given in Table 1.

The dynamic responses of the spindle with the consideration of uncertainty are exposed in Figs. 4 and 5. The resolution of the differential equations of the electromagnetic spindle with interval, allowed obtaining results similar to those with fixed
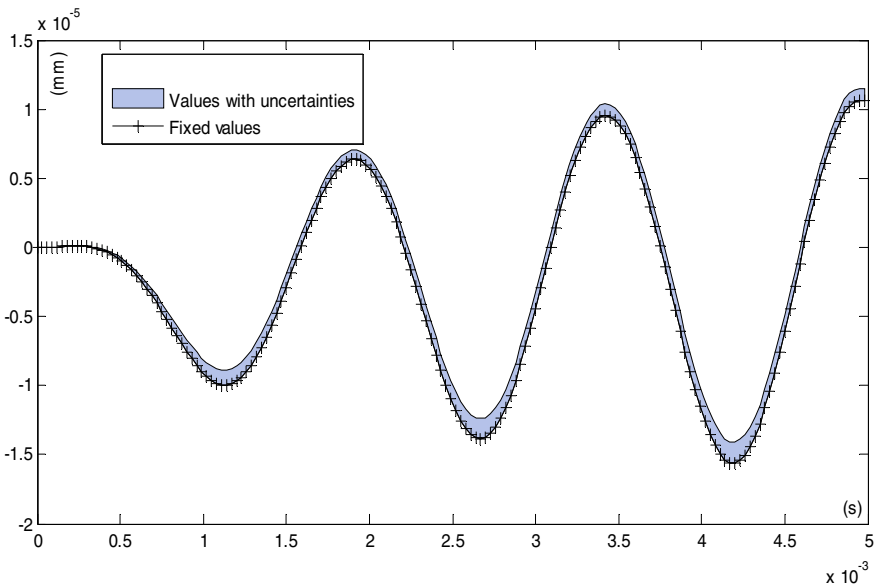
Fig. 4 Variation of the displacement Z
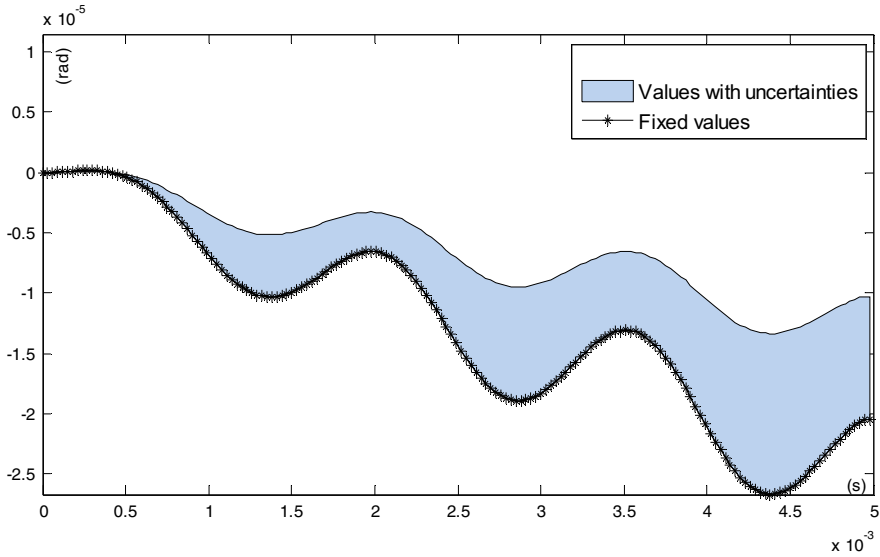
Fig. 5 Variation of the rotational movement θ_x

values. Envelopes of performances are obtained, which represent the set of values for the displacement Z and the rotational movement θ of the elastic part.

Thus, according to the obtained envelopes, the designer can therefore determine the best solution (design) that can fulfill the imposed requirements, which facilitates the sizing of the studied system and therefore to obtain a guaranteed design process.

4 Conclusion

In this paper, the study of the dynamic behavior of an electromagnetic spindle supported by two AMBs using the interval calculation technique was done. A complete envelope (a set of solutions) is obtained for the different design parameters and therefore to avoid making several simulations that in most cases make the model to study expensive or inefficient.

The goal of future work is to perform parametric studies to study the influence of different design parameters on the behavior of the spindle and to optimize its model.

References

Auchet S, Chevrier P, Lacour M, Lipinski P (2004) A new method of cutting force measurement based on command voltages of active electro-magnetic bearings. Int J Mach Tools Manuf 44:1441–1449. https://doi.org/10.1016/j.ijmachtools.2004.05.009

Bouaziz S, Messaoud NB, Mataar M, Fakhfakh T, Haddar M (2011) A theoretical model for analyzing the dynamic behavior of a misaligned rotor with active magnetic bearings. Mechatronics 21:899–907. https://doi.org/10.1016/j.mechatronics.2011.05.001

Chen M, Knospe CR (2007) Control approaches to the suppression of machining chatter using active magnetic bearings. IEEE Trans Control Syst Technol 15:220–232. https://doi.org/10.1109/TCST.2006.886419

Chiba A, Fukao T, Ichikawa O, Oshima M, Takemoto M, Dorrell D (2005) Magnetic bearings and bearingless drives. Elsevier. https://doi.org/10.1016/b978-0-7506-5727-3.x5000-7

Faroughi S, Lee J (2015) Analysis of tensegrity structures subject to dynamic loading using a Newmark approach. J Building Eng 2:1–8. https://doi.org/10.1016/j.jobe.2015.03.005

Gourc E, Seguy S, Arnaud L (2011) Chatter milling modeling of magnetic bearing spindle in high speed domain. Int J Mach Tools Manuf 51:928–936. https://doi.org/10.1016/j.ijmachtools.2011.08.008

Gościniak I, Gdawiec K (2019) Control of dynamics of the modified Newton-Raphson algorithm. Commun Nonlinear Sci Numer Simul 67:76–99. https://doi.org/10.1016/j.cnsns.2018.07.010

Hentati T, Bouaziz A, Bouaziz S, Choley JY, Haddar M (2013) Dynamic behaviour of active magnetic bearings spindle in high-speed domain. Int J Mechatron Manuf Syst 6:474–492. https://doi.org/10.1504/IJMMS.2013.058527

Kimman MH, Langen HH, Munning Schmidt RH (2010) A miniature milling spindle with active magnetic bearings. Mechatronics 20:224–235. https://doi.org/10.1016/j.mechatronics.2009.11.010

Knospe CR (2007) Active magnetic bearings for machining applications. Control Eng Prac 15:307–313. https://doi.org/10.1016/j.conengprac.2005.12.002

Kyung JH, Lee CW (2003) Controller design for a magnetically suspended milling spindle based on chatter stability analysis. JSME Int J Ser C-Mech Syst Mach Elem Manuf Jpn Soc Mech Eng 46:416–422. https://doi.org/10.1299/jsmec.46.416

Sawicki JT, Maslen EH, Biscof KR (2007) Modeling and performance evaluation of machining spindle with active magnetic bearing. J Mech Sci Technol 21:847–850. https://doi.org/10.1007/BF03027055

Schweitzer G, Bleuler H, Cole M, Keogh P, Larsonneur R, Malsen E, Nordmann R, Okada Y, Traxler A (2009) Magnetic bearings: theory, design, and application to rotating machinery. Springer. https://doi.org/10.1007/978-3-642-00497-1

Trabelsi H, Guizani A, Tounsi D, Hammadi M, Barkallah M, Haddar M (2019) Consideration of uncertainties in the preliminary design case of an electromagnetic spindle. J Theor Appl Mech 57:821–832. https://doi.org/10.15632/jtam-pl/111913

Tsai NC, Lee RM (2011) Regulation of spindle position by magnetic actuator array. Int J Adv Manuf Technol 53:93–104. https://doi.org/10.1007/s00170-010-2830-0

Magnesium Powder Compacting

Anas Bouguecha and Bernd-Arno Behrens

Abstract Sintering technology is becoming increasingly important in metal industry as they offer numerous advantages comparing to other manufacturing processes. So that, the powder metal (PM) technology is currently well-established for the manufacturing of near-net-shape thin-walled sintered components with strong cross-sectional transitions, especially in the automotive industry. The density gradients in the green bodies caused during the powder compacting process lead to the sintering distortion which is a relevant problem in this industry. The numerical simulation based on the finite element method (FEM) can provide a significant contribution in the design and optimization of powder compacting processes to reliably reduce such problems. Here, the material modeling required for the FE calculation is of crucial importance. In this presented work, the DRUCKER-PRAGER-Cap model was chosen for the numerical description of the compressible behavior of magnesium powder. Here, in the first step, the material-dependent failure line was determined on the basis of diametrical and uniaxial compression tests. In the second step, the elliptical caps depending on the relative density were specified by means of a simple axial compression test combined with the assumption of associated flow. This material modeling is then used to study the influence of the powder compacting strategy on the homogeneity in the distribution of the relative density is shown for the rotationally symmetric L-shape.

Keywords Sintering · Compacting · Magnesium · FE Simulation · Material Modeling

A. Bouguecha (✉)
Laboratory of Mechanics, Modeling and Manufacturing (LA2MP), National School of Engineers of Sfax (ENIS), University of Sfax, Sfax, Tunisia
e-mail: anas.bouguecha@gmx.de

B.-A. Behrens
Institute of Forming Technology and Machines, Leibniz Universitaet Hannover, Hanover, Germany
e-mail: behrens@ifum.uni-hannover.de

© Springer Nature Switzerland AG 2020

1 Introduction

Sintering technology has its origins in the ceramic industry but is becoming increasingly important in metal industry as they offer numerous advantages comparing to other manufacturing processes, such as low energy consumption and high material utilization (Fig. 1). Partly for these reasons, the proportion of powder metallurgy (PM) components in the automotive industry has steadily increased in recent years (Herlan 1989).

According to Schatt and Wieters (1994), PM production processes can be subdivided mainly into powder production, shaping by compacting, sintering and finishing (Fig. 2).

PM technology is established for the manufacturing of near-net-shape thin-walled sintered components with strong cross-sectional transitions, as presented in Fig. 2 (Doege et al. 2003). For this, powder presses equipped with multi-punches adapter are necessary. In Fig. 3 the powder press available at the IFUM is shown.

For the design and optimization of the tool kinematic strategy, numerical simulations are performed in which the influence of the tool movement on the distribution of the porosity in the component is examined. In such FE calculations, material modeling plays a crucial role.

In this research work, the precise FE simulation of the compacting process of magnesium powder is presented. Hence, the influence of the kinematics of the punches on the compacting result in the component is numerically examined.
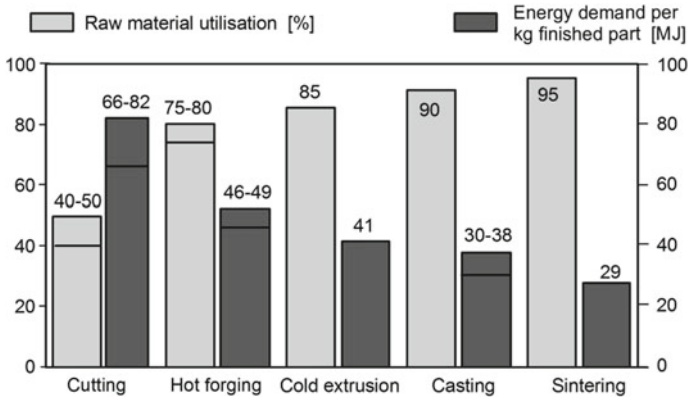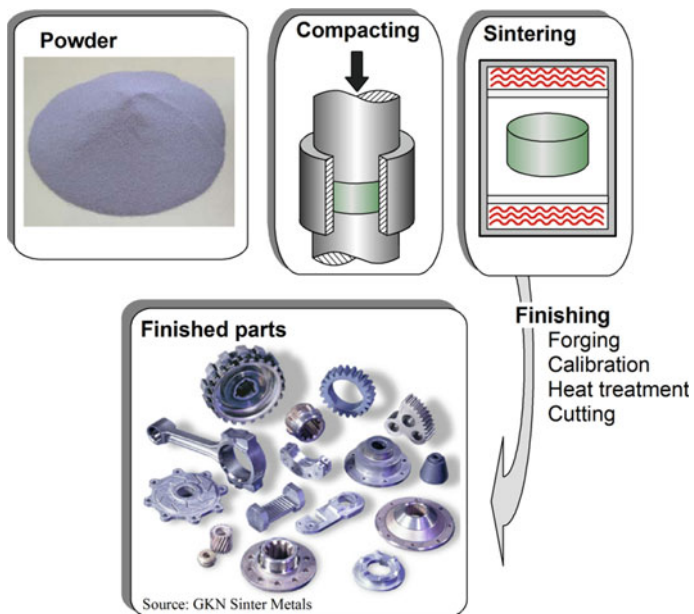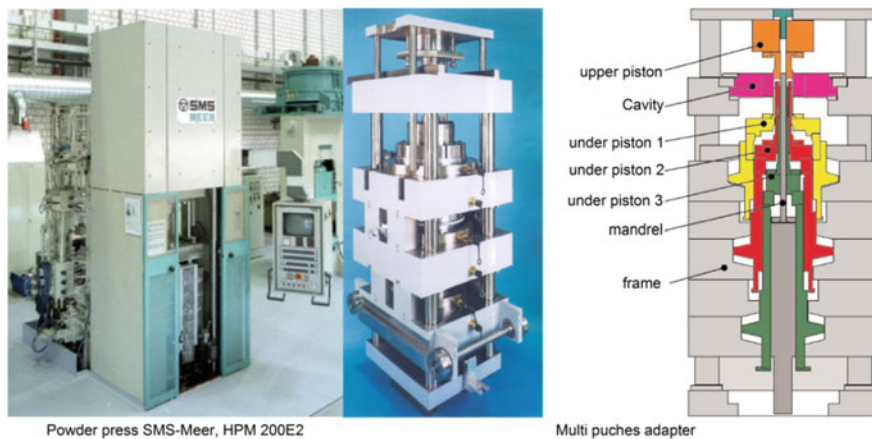

Fig. 1 Advantages of the metal sintering industry (according to Herlan 1989)

Fig. 2 Manufacturing flow in the metal sintering industry (according to Behrens and Bouguecha 2012)

Fig. 3 Powder press available at the IFUM with a multi punches adapter (according to Behrens et al. 2005)

2 Material Modeling

For the description of the compressible material behavior of the considered magnesium powder, the DRUCKER-PRAGER-Cap (DPC) model is used for the numerical investigations of the powder compacting process and adapted to the investigated aluminum powder (Riedel 1997).

The DPC model is used to map the properties of porous materials in the FE simulation. Here a body is considered as an elastic-plastic and compressible continuum (Doege et al. 2003). In the plane of the hydrostatic pressure p and the v Mises equivalent stress q, the yield surface is composed of an elliptical hardening cap and a straight failure line, as shown in Fig. 4, and is described by Eqs. 1 and 2 described (Doege et al. 2003).

$$F_k = \sqrt{(p - p_a)^2 + Rq^2} - R(d + p_a \tan \beta) = 0 \tag{1}$$

$$F_v = q - p \tan \beta - d = 0 \tag{2}$$

Here, R represents the eccentricity of the elliptical cap, and p_a the pressure at which the cap merges into the failure line. The shear strength d and the slope $\tan \beta$ characterize the failure line and thus the green strength in the green part (Riedel 1997).

Within the yield surface, the material behaves elastically. When the stress state reaches the locus, plastic deformation of the powder begins. Stress conditions on the
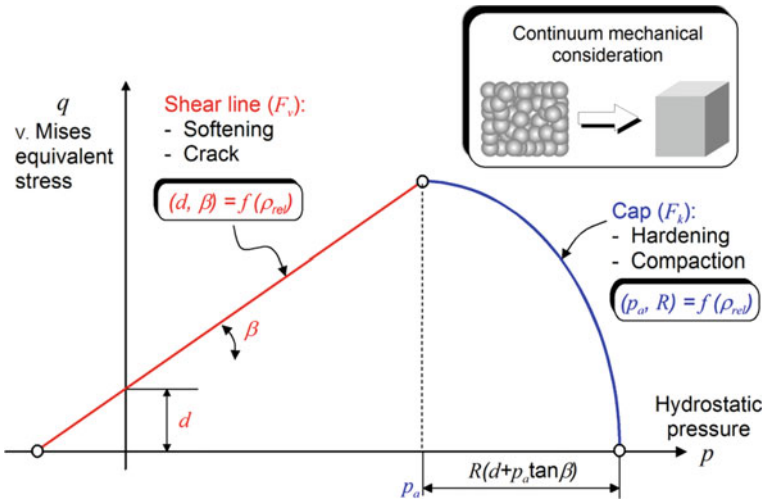

Fig. 4 Yield surface in the DPC model (according to Behrens et al. 2005, 2006; Behrens and Bouguecha 2012)

consolidation cap result in compaction of the powder. In contrast, stresses on the failure line cause softening, which results in the risk of cracking (Doege et al. 2003).

To describe the porosity of a material, the relative density ρ_{rel} is defined, which represents the ratio of the particle volume to the total volume (Eq. 3).

$$\rho_{rel} = \frac{V_{Particles}}{V_{total}} 100\% \qquad (3)$$

The investigated magnesium powder was produced in the Center for Functional Materials gGmbH in Clausthal-Zellerfeld by gas atomization under protective gas. The grain size is about 25 μm.

2.1 Shear Lines of the DPC Model

The failure straight line, as shown in Fig. 4, can be determined experimentally with different strength tests giving different stress states (p and q). In this work, the diametrical and the uniaxial compression tests with different specimen sizes are used (Fig. 5).

For each green body with a specific relative density ρ_{rel}, the v Mises equivalent stress q and the hydrostatic pressure p were calculated by means of the measured breaking stress in the diametrical and the uniaxial compression tests (Table 1).

On the basis of these points developed, the failure lines for the considered relative densities ρ_{rel} can be formed in the model plane, as shown in Fig. 6. As the failure lines are approximately congruent, a mean failure line will be implemented and used later.
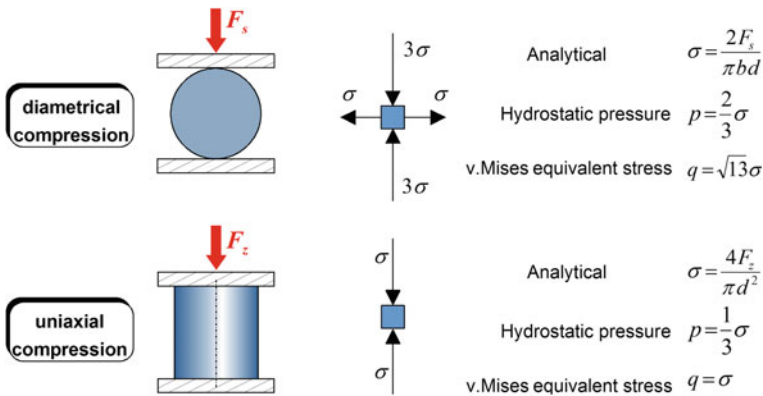

Fig. 5 Yield surface in the DPC model (Behrens et al. 2006; Behrens and Bouguecha 2012)

Table 1 Determined stress states from the diametrical and the uniaxial compression tests (according to Behrens et al. 2005)

Test	Diametrical compression				Uniaxial compression			
Specimen size	Ø 8 × 8 (mm)		Ø 8 × 12 (mm)		Ø 8 × 8 (mm)		Ø 8 × 12 (mm)	
ρ_{rel} (%)	p (MPa)	q (MPa)	p (MPa)	q (MPa)	p (MPa)	q (MPa)	p (MPa)	q (MPa)
80	0.11	0.61	0.18	0.96	3.28	9.85	1.99	7.3
85	0.5	2.691	0.44	2.39	12.27	36.82	6.635	19.9
90	1.27	6.89	1.26	6.82	13.2	39.61	13.27	39.81
95	2.65	14.35	3.1	16.75	15.26	47.3	28.02	84.06
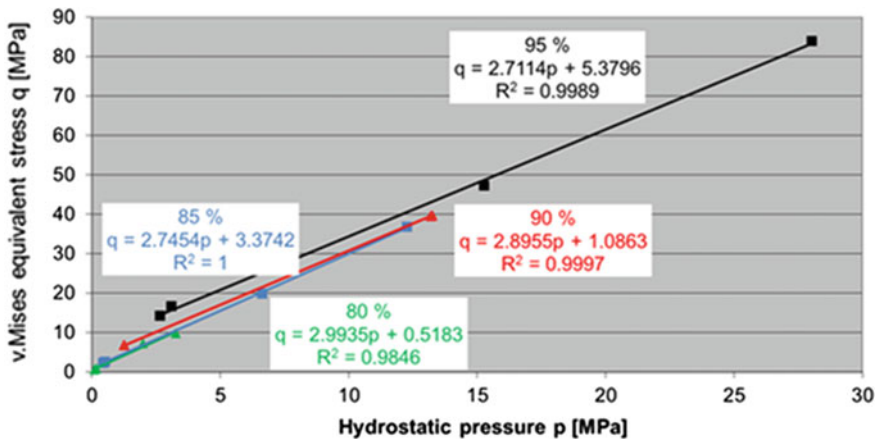
Fig. 6 The shear failure lines for different relative densities

2.2 Hardening Cups of the DPC Model

In the literature, the elliptical cap is measured by triaxial experiments (Coube and Riedel 2000). However, these experiments are associated with great experimental effort and the construction of the measuring device is costly. Therefore, the method described in (Doege et al. 2003; Behrens and Bouguecha 2012) is used in this work, which is based solely on simple axial compression tests and the assumption of associated flow (Fig. 7).

Thus, the material parameters R and p_a of the hardening cap in the DPC model can be calculated as a function of the relative density ρ_{rel} (Table 2).

The results of the determined DPC models depending on the relative Density are presented in Fig. 8.
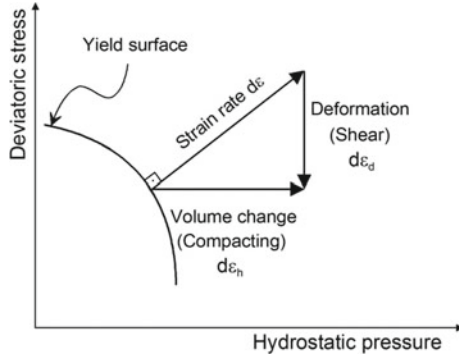
Fig. 7 Associated flow (according to Behrens and Bouguecha 2012)

Table 2 The model-relevant parameters of the compacting cap (according to Behrens et al. 2005)

ρ_{rel} (%)	p_a (MPa)	R (−)
80	26.57	0.745
85	33.87	0.772
90	47.81	0.797
95	77.63	0.808
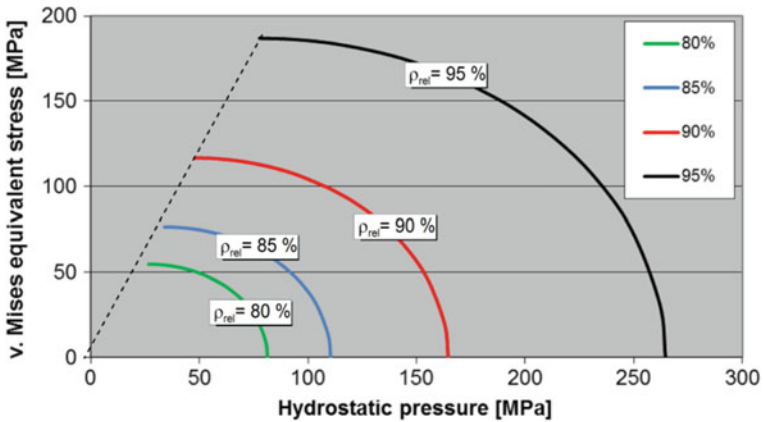
Fig. 8 Yield cups in the DPC model for different relative densities (according to Behrens et al. 2005, 2006)

3 Importance of the Tool Kinematics on the Compacting Process

Powder metallurgical forming processes have become established in the manufacture of stepped thin walled components.

In order to show the advantages of numerical simulation in the design and optimization of the compacting of magnesium alloys, the manufacturing process of two components (a thin walled reference L-shape and a complex stepped crown gear) are considered in this study.

The magnesium powder has an initial density of 43% and the aimed relative final density of 90%. The aim is that during compaction as possible no powder is moved from one to another cross-section to minimize shear stress and to avoid cracks.

The height of the tool cavity before pressing is given by the following equation:

$$h_{cavity} = \frac{\rho_{rel,initial}}{\rho_{rel,final}} h_{final} \qquad (4)$$

Since friction has a decisive influence on the density distribution, the density-dependent sliding friction coefficients determined in (Behrens et al. 2004) are implemented in the commercial FE system ABAQUS/STANDARD and used for the following rotationally symmetric calculations. In order to investigate the influence of the tool kinematics on the compaction behavior, the one-sided and the double-sided compacting will be compared.

The final dimensions of the green compact after compacting of the reference L-shape are shown in Fig. 9.
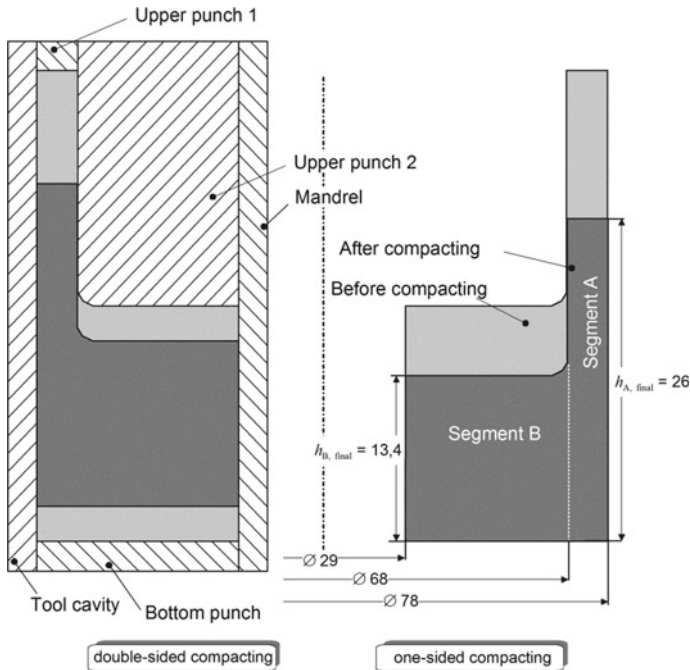

Fig. 9 Reference part L-shape (according to Behrens and Bouguecha 2012)

The design of the process is based on the proportional compacting. This means no material flow between the segments (A and B) of the part, as shown in Fig. 9. Therefore, the one-sided compacting (Fig. 9, right) occurs exclusively by the movement of both upper punches at different speeds due to the different compacting paths. In contrast, in two-sided pressing (Fig. 9, left), in addition to the movement of both upper punches, the lower punch moves at the same speed in the opposite direction as the upper punch 2. In both cases, the die and the mandrel are fixed. In the quasi-static calculations performed, only half of an axial cross-section is discretized with 4-noded rotationally symmetrical quadrangular elements (type: CAX4) due to the axis symmetry of the green body. The tools are assumed to be rigid bodies. In order de determine the number of elements for the discretization of the part a convergence study is firstly performed. This study has shown that the convergence in the punch forces is reached by the use of 300 elements at the least.

Figure 10 shows the density distributions in the one-sided and the double-sided compacted green body. It is to be noted that in contrast to the one-sided pressing, in which the low densities are in the lower region of the reference component, they are located vertically centered in the two-sided compression. Furthermore, in the one-side pressed component, the density distribution is very inhomogeneous, since the corresponding density gradients ($\Delta\rho_{rel} = 30\%$) are high due to the frictional effects. In double-sided compression, on the other hand, the density gradients are much lower ($\Delta\rho_{rel} = 16\%$). Thus, it is characterized by a more homogeneous distribution of relative density.
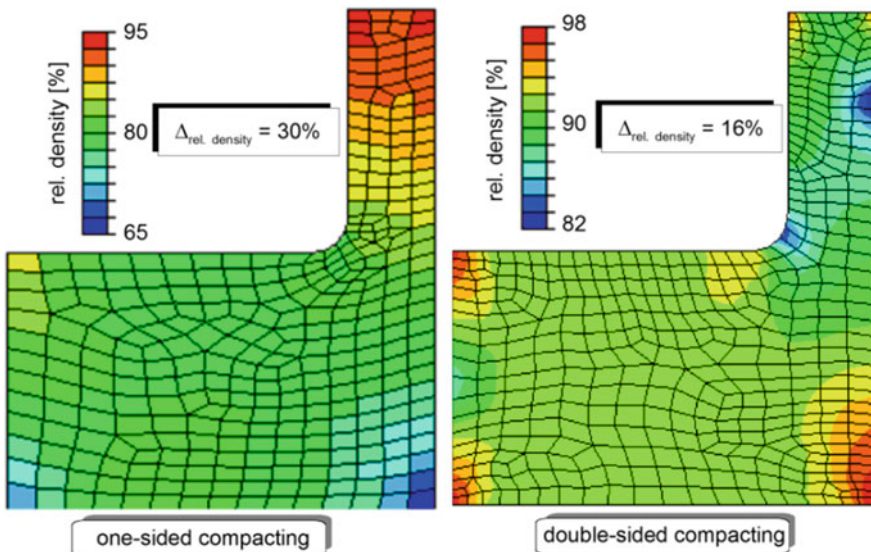
Fig. 10 Calculated compaction in the reference L-shape (left: one-sided powder compacting, right: double-sided powder compacting)

4   Conclusion

In order to provide a precise calculation of powder compaction processes using the FEM, the DPC model was used in this work to describe the compressible behavior of magnesium powder numerically. Here, the determination of the material-dependent failure line was carried out on the basis of diametrical and uniaxial compression tests. Furthermore, the elliptical cap, which represents the hardening behavior of the magnesium powder, was determined by means of a simple method which is based solely on axial compression tests and the assumption of associated flow.

This material modeling is then used for the simulation-based design of powder compacting processes. In this study the influence of the powder compacting strategy on the homogeneity in the distribution of the relative density is shown for the rotationally symmetric L-shape.

References

Behrens B-A, Bouguecha A (2012) Numerical and experimental investigations of aluminum powder compaction and sintering. Mat-wiss und Werkstofftech 43(6):511–519

Behrens B-A, Bouguecha A, Hanini K (2004) Ermittlung dichteabhängiger Reibkoeffizienten für das Pressen von Aluminiumpulver. UTFscience, IV

Behrens B-A, Gastan E, Bouguecha A (2005) Numerische und experimentelle Untersuchungen zum Matrizenpressen von Mg-Legierungen. Metall 59(7–8):469–472

Behrens B-A, Bouguecha A, Gastan E (2006) Numerische Untersuchungen zum Pulverpressen von Magnesium. Metall 60(4):210–213

Coube O, Riedel H (2000) Numerical simulation of metal powder die compaction with special consideration of cracking. Powd Metall 43(2):123–131

Doege E, Hanini K, Schmidt-Jürgensen R (2003) Numerische und experimentelle Untersuchungen zum Pulverpressen von Aluminium. Mat-wiss und Werkstofftech 34:729–735

Herlan T (1989) Optimaler Energieeinsatz bei der Fertigung durch Massivumformung. Dissertation, Universitaet Stuttgart, Springer, Berlin

Riedel H (1997) Rechnerisch optimiertes Pressen und Sintern: Formgenaue und rissfreie Teile. Schweizer Maschinenmarkt 20:54–56

Schatt W, Wieters KP (1994) Pulvermetallurgie, Technologien und Werkstoffe. VDI Verlag, Düsseldorf

Frequencies Analysis of a Segmented Wind Turbine Blade in Presence of Uncertainty

Majdi Yangui, Abderraouf Kamel, Mounir Ben Jdidia, Lotfi Hammami, Slim Bouaziz, and Mohamed Haddar

Abstract Wind turbine blades structures must be well balanced during the manufacturing and mounting processes in order to avoid the imbalance of the system and the undesirable dynamic effects during the rotor motion. This work presents a numerical frequencies analysis of a segmented wind turbine blade assembled with a steel spar in order to study the effects of the assembling load, considered as a uncertainty parameter, on the wind turbine rotor balance. For this purpose, the finite beam element was adopted to model the blade segments and the spar structures. The additional assembly stiffness caused by segments assembly load was considered in the developed numerical model. In this work, a deterministic analysis was established to study the influence of the applied load on the assembled blade natural frequencies. Furthermore, a stochastic approach was proposed, based on the Monte Carlo method considering the assembly load as a random variable, to discuss their influences on the wind turbine rotor balance. This study, highlights the significant influence and the importance of the assembly load adjustment on the segmented blade dynamic behavior and thus on the wind turbine life cycle. Thus, the wind turbine rotor must be equipped with a mechatronic system to ensure the blades behavior readjustment during the rotor motion.

M. Yangui (✉) · A. Kamel · M. Ben Jdidia · L. Hammami · S. Bouaziz · M. Haddar
Mechanics, Modelling and Production Laboratory (LA2MP), Mechanic Department, National
School of Engineers of Sfax, University of Sfax, B.P. 1173, 3038 Sfax, Tunisia
e-mail: yanguimajdi@gmail.com

A. Kamel
e-mail: abderraof.kamel@gmail.com

M. Ben Jdidia
e-mail: mounir.benjdidia@enis.rnu.tn

L. Hammami
e-mail: lotfi.hammami@enis.rnu.tn

S. Bouaziz
e-mail: slim.bouaziz1@gmail.com

M. Haddar
e-mail: mohamed.haddar@enis.rnu.tn

1 Introduction

The concerns about environmental problems has made the wind energy, considered as one of the most profitable renewable energy sources, development more and more indispensable for a sustainable future. Accordingly, in order to extract more energy from wind, manufacturers aim to develop the wind turbine blade size and to reduce the manufacturing and transport costs. For this purpose, the wind turbine blade segmentation into several parts assembled altogether along a steel spar was proposed. In this context, Saldanha et al. (2013) showed that the natural frequencies of the wind turbine system are an important parameter to design a segmented wind turbine blade. Furthermore, several studies were developed to investigate the dynamic behavior of rotating wind turbine blade taking into account various external effects and loads. However, the influence of the segments assembly effort was ignored, which must be considered in priority during the segmented blade design. Yangui et al. (2018) investigated the dynamic behavior of a segmented wind turbine blade using the finite element method. Experimental and numerical modal analysis was developed by Tartibu et al. (2012). The wind turbine blade modeling was treated by some simplified shapes of stepped beam. The measured and computed natural frequencies present some discrepancies observed for the highest frequencies. In fact, numerical methods are conducted on models that can not take account of all characteristics of real blade structure and their working conditions. To study the effects of the assembling load on the segmented shell type wind turbine blade, Yangui et al. (2019) developed a numerical model using the 3 node shell element DTK18. To determine the effects of segments assembly load on the rotor dynamic behavior, experimental modal analysis was established. The discussion of the experimental results showed the considerable influence of the segments assembly load on the blade dynamic behavior, which must be well investigated to ensure the rotor stability. Several parametric studies was established to investigate the wind turbine dynamic behavior. However, the parameters lack of precision give rise to unreliable results. Thus, considering the uncertainties of the investigated parameters in the numerical model is very important to ensure the stability and the robustness of the structure. To this end, probabilistic approaches are adopted to consider the effects of the parameters uncertainties. In these approaches, the uncertain variables were treated by probability density functions. The Monte Carlo simulation is one of the most known probabilistic methods able to provide accurate results. The accuracy and the reliability of this method is discussed by Shreider (2014).

In the present work, the finite beam element is used to model a segmented wind turbine blade assembled altogether along a steel spar. The aerodynamic profile, the spar and the assembly stiffness matrix caused by the assembly load are considered

in the developed numerical model. In this work, the segments assembly load is considered as uncertain parameter. To predict the wind turbine blade natural frequencies taking into account of the uncertain parameter, the Monte Carlo method is adopted.

2 Assembled Blade Design and Modeling

The investigated wind turbine blade consists of five segments assembled with a steel threaded shaft and a nut modeled as a spar. The blade model is presented in Fig. 1.

The designed segmented blade has a length $L = 22$ m where the aerodynamic profile was presented by Griffin (2000). The blade segments and spar material properties are presented in Table 1.

To model the blade and the spar structure, 36 finite beam elements of different cross sections were used to discretize the blade segments structure and 30 elements were adopted to model the spar. Each beam element has six degrees of freedom per node. Thus, the blade equation of motion can be written as:

$$[M]\ddot{q} + [C]\dot{q} + [K_e]q = \{F\} \tag{1}$$

where $[M]$, $[C]$, $[K_e]$ and $\{F\}$ are respectively the mass matrix, the damping matrix, the elastic stiffness matrix and the global force vector applied on the blade. The defined matrices are obtained by assembling the elementary matrices given by Hamdi et al. (2011).

Taking into account of the segments assembling load, an additional strain energy increases the investigated blade stiffness. To this end, the stiffness of a beam in
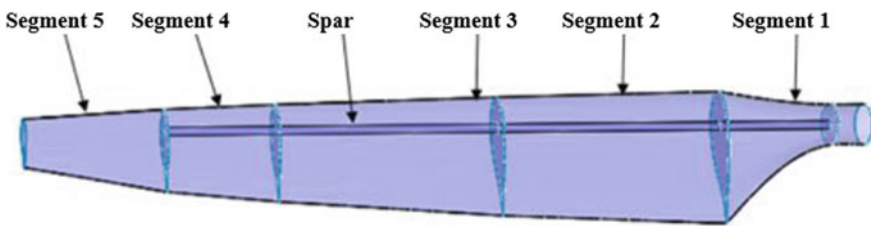
Fig. 1 Assembled wind turbine blade

Table 1 Blade segments and spar material properties

Parameters	Elastic modulus (GPa)	Poisson's ratio	Density (kg/m^3)
Blade segments	1.7	0.35	2530
Spar	210	0.3	7850

traction presented by Lalanne and Ferraris (1998) is considered in the assembled blade modeling. Thus, the resulting equation of motion is obtained as:

$$[M]\ddot{q} + [C]\dot{q} + ([K_e] + [K_S])q = \{F\} \tag{2}$$

where $[K_S]$ represents the assembly stiffness matrix obtained by assembling the elementary matrix $[k_s]$ expressed by:

$$[k_s] = \frac{F_{ass}}{30l} \begin{bmatrix} 0 & 0 & 0 & 0 & 0 & 0 & 0 & 0 & 0 & 0 & 0 & 0 \\ 0 & 36 & 0 & 0 & 0 & -3l & 0 & -36 & 0 & 0 & 0 & -3l \\ 0 & 0 & 36 & 0 & 3l & 0 & 0 & 0 & -36 & 0 & 3l & 0 \\ 0 & 0 & 0 & 0 & 0 & 0 & 0 & 0 & 0 & 0 & 0 & 0 \\ 0 & 0 & 3l & 0 & 4l^2 & 0 & 0 & 0 & -3l & 0 & -l^2 & 0 \\ 0 & -3l & 0 & 0 & 0 & 4l^2 & 0 & 3l & 0 & 0 & 0 & -l^2 \\ 0 & 0 & 0 & 0 & 0 & 0 & 0 & 0 & 0 & 0 & 0 & 0 \\ 0 & -36 & 0 & 0 & 0 & 3l & 0 & 36 & 0 & 0 & 0 & 3l \\ 0 & 0 & -36 & 0 & -3l & 0 & 0 & 0 & 36 & 0 & -3l & 0 \\ 0 & 0 & 0 & 0 & 0 & 0 & 0 & 0 & 0 & 0 & 0 & 0 \\ 0 & 0 & 3l & 0 & -l^2 & 0 & 0 & 0 & -3l & 0 & 4l^2 & 0 \\ 0 & -3l & 0 & 0 & 0 & -l^2 & 0 & 3l & 0 & 0 & 0 & 4l^2 \end{bmatrix} \tag{3}$$

where F_{ass} and l are, respectively, the assembling load and the beam element length.

3 Monte Carlo Method

The Monte Carlo method is the most widely used to investigate uncertainty propagation problems. This method is based on a probability law of a sampling of uncertain variables. Therefore, a deterministic calculation must be effected for each random draw. Usually, this method lead to determine precise results. Considering the great number of simulations to perform, the Monte Carlo implementing require lots of computing power. The method implementation and process, detailed by Hammersley (2013), is presented in Fig. 2.

As presented the Monte Carlo implementation can be summarized as follows: Once the uncertain parameters and the corresponding probability laws are identified, a random generation and a sampling of the input vector is executed to determine the propagation of the uncertainty i.e. the output vector. The obtained results are analysed statistically by the determination of the mean value and the standard deviation.

Fig. 2 Implementation of the Monte Carlo method
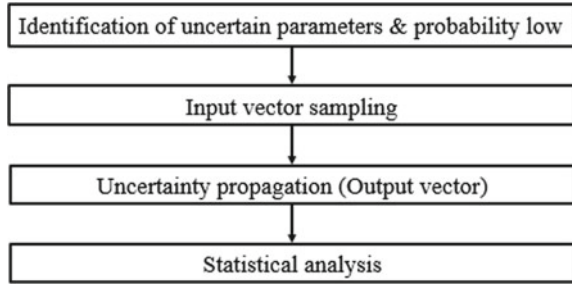
Table 2 Segmented blade natural frequencies variation

	1st natural frequency	2nd natural frequency	3rd natural frequency
$F_{ass} = 0 \text{ N}$	0.85	1.06	3.22
$F_{ass} = 250 \text{ N}$	1.52	2.37	3.35
$F_{ass} = 500 \text{ N}$	1.98	3.02	3.41

4 Results and Discussion

To study the influence of assembly load on the segmented wind turbine blade natural frequencies, a deterministic and a probabilistic analysis were performed.

4.1 Deterministic Analysis

Taking into account of the segments assembly load F_{ass}, the first three natural frequencies of the blade were determined. The obtained results are illustrated in Table 2.

The present results show that blade natural frequencies are strongly influenced by the segments assembly load. The discussed parameter can be maladjusted during the blade mounting or messed up under the wind turbine rotor motion. Thus, it must be considered as an uncertainty parameter in the wind turbine system investigation.

4.2 Probabilistic Analysis

In this section, a probabilistic analysis of the blade natural frequencies was performed. The segments assembling load, considered as an input variable, follows the normal distribution:

$$F_{ass} = F_{ass_0} + \sigma_{F_{ass}}\xi \tag{4}$$

Table 3 Natural frequencies mean values and standard deviations

	1st blade mode	2nd blade mode	3rd blade mode
Natural frequency mean value	1.98	2.97	3.32
Standard deviation	0.19	0.11	0.16

where F_{ass_0} is the mean value, $\sigma_{F_{ass}}$ represents a normal or uniform variable and ξ represents a convenient constant.

The Natural frequencies mean values and the standard deviations were determined for $F_{ass_0} = 500\ N$ and $\sigma_{F_{ass}} = 10\%$. The obtained results convergence were ensured with 2000 simulations. The first three natural frequencies mean values and standard deviations are presented in Table 3.

According to the obtained results, the standard deviations caused by 10% of assembly load variation are very important. In general the wind turbine rotor is composed by three blades, thus this variation can involve the system imbalance and undesirable dynamic effects during the rotor motion.

5   Conclusion

In this study, a segmented wind turbine blade assembled with a spar has been modeled using linear beam elements. A deterministic and a probabilistic analysis were performed to investigate the effects of the segments assembly load on the blade natural frequencies. The Monte Carlo method was adopted to determine the mean values and standard deviations of the blade natural frequencies caused by 10% of assembly load variation. Results show the significant influences of the assembly load uncertainty on the rotor balance. Thus, the necessity of a mechatronic system to ensure the adjustment of the blades rotor dynamic behavior during the wind turbine operation. The present research can be extended taking into account all the wind turbine systems and the aerodynamic effects.

References

Griffin DA (2000) NREL advanced research turbine (ART) aerodynamic design of ART-2B rotor blades. National Renewable Energy Lab, Golden, US

Hamdi H, Mrad C, Nasri R, Hamdi A (2011) Static and dynamic study of a wind turbine blade with horizontal axis. J Environ Sci Eng 5(9):1167–1174

Hammersley J (2013) Monte Carlo methods. Springer Science & Business Media, London

Lalanne M, Ferraris G (1998) Rotordynamics prediction in engineering, 2nd edn. Wiley

Saldanha FA, Rao VV, Christopher J, Adhikari R (2013) Investigations on concepts for modularizing a horizontal axis wind turbine blade. In: ASME 2013 international design engineering technical conferences and computers and information in engineering conference. American Society of Mechanical Engineers Digital Collection

Shreider YA (2014) The Monte Carlo method: the method of statistical trials. Elsevier

Tartibu LK, Kilfoil M, Van Der Merwe AJ (2012) Vibration analysis of a variable length blade wind turbine. Int J Adv Eng Technol 630–639

Yangui M, Bouaziz S, Taktak M, Haddar M, El-Sabbagh A (2018) Nonlinear analysis of twisted wind turbine blade. J Mech 34(3):269–278

Yangui M, Bouaziz S, Taktak M, Debut V, Antunes J, Haddar M (2019) Numerical and experimental analysis of a segmented wind turbine blade under assembling load effects. J Theor App Mech 57(1):85–97

Modeling the Transmission Path in a Planetary Gearbox: A Comparison of Two Methods

Oussama Graja, Ahmed Ghorbel, Fakher Chaari, and Mohamed Haddar

Abstract   When the goal is to reduce the shaft speed with an important ratio between a driving and a driven part, engineers use a planetary gearbox (PG). For this reason, this power transmission system can be found in many mechanical units such as excavators, helicopters, ship propeller, etc. Hence, their condition-based monitoring has been investigated for decades and their diagnostic is still important since their breakdown can cause catastrophes and disasters. So, researchers have been interested in the difference between healthy and damaged cases PG dynamic behaviour. Due to its complex design, the knowledge of its healthy state is still investigated: as known, planet gears have two rotational motions: first one is around itself and the second one is around the gearbox centre. The last motion amplitude modulates the vibration signal acquired by a sensor attached to the housing. Hence, in this work, the variable transmission path in a planetary gearbox is modelled by two mathematical approaches. One of the above methods can be used when the amplitude modulation phenomenon is explicitly modelled from the dynamic model, in other words, when someone thinks to use a windowing function to model amplitude modulation phenomenon in a planetary gearbox. Advantages and drawbacks of each methodology are investigated.

Keywords Planetary gearbox · Dynamic modelling · Vibration transmission path

Nomenclature

f_c	Carrier frequency
GMF	Gear mesh frequency
N	Number of planets
R_r	Base radius of the ring gear
R_c	Radius where the carrier holds planets

O. Graja (✉) · A. Ghorbel · F. Chaari · M. Haddar
Tunisia (ENIS)/Laboratory of Mechanics, Modelling and Production (LA2MP), National School of Engineers of Sfax, Sfax, Tunisia
e-mail: grajaoussama@gmail.com

95

U   Time varying distance
θ_c Instantaneous angle of the carrier

1 Introduction

Since a transducer is attached to the gearbox housing and the planet gears have a
relative motion with respect to it, the transmission path of vibration in a planetary
gearbox is time varying which causes an amplitude modulated vibration signal. This
phenomenon has been investigated from several researchers to clarify that it is a
major characteristic of healthy behavior and differs from a modulation due to faults.

A double helical planetary gear 3D lumped parameters model is proposed by
Prashant and Kahraman (2013). Their work can be summarized into two points: first
to predict the maximum amplitude of the dynamic mesh force; second to investigate
the mesh force changes due to a sun gear radial floating. A mathematical model
was developed by Inalpolat and Kahraman (2009) in order to report the modula-
tion sideband origin occurring in a healthy planetary gear-set. The investigation of
the sideband around the gear-mesh frequency component in spectrum results that
it comes principally from an epicyclical gearbox having either a stationary sun or
ring gear. Later, they developed a nonlinear dynamic model in order to evaluate the
modulation activity in a damaged planetary gear-set in the form of run out and eccen-
tricity (Inalpolat and Kahraman 2010). Mesh force fluctuation is also investigated
by Guo and Parker (2010) and they declared that it was originated from tooth wedg-
ing, causing bearing failures. A model was developed to combine wedging, bearing
clearance, back-side contact and tooth separation influence. Both amplitude and fre-
quency modulation phenomenon in time series which occur as side-band activity in a
spectrum were studied by Feng and Zuo (2012), Liang et al. (2015), Liu et al. (2016).
Feng and Zuo (2012) simulate the dynamic behaviour in case of gear damages (faulty
planet and sun gear) after defining faulty gears characteristic frequencies in a PG.
A lumped parameter model was developed by Liang et al. (2015) in order to build
sources of vibration. Then, all vibration was projected with respect to the sensor
location by including the transmission path effect due to the planet gear motion held
by the carrier. Properties of vibration signals were investigated in both cases: healthy
and cracked tooth case. In a later work, Liu et al. (2016) focused on modelling the
transmission path. They consider that the vibration path can be divided into two
parts: a first part from gears to the housing and a second part through the casing up
to the sensor location. A mathematical formulation was developed by Graja et al.
(2017) in order to model the transmission path of vibrations. Since the planetary
gearbox casing is cylindrical, they approximate the time varying path separating the
sensor location and the planet/ring gear contact to an arc. In a later work, Graja et al.
(2019) developed another formulation for modelling the transmission path. They
considered that the distance separating the centre of planet gear and the transducer
location is time varying and it can reflect an image of the transmission path. In Graja

et al. (2017, 2019), attractive results were presented and the sideband activity of acceleration signals in frequency domain is figurative.

As mentioned, the path of vibration in a planetary gearbox was extremely investigated. Hence, in this work, authors aim to compare two new developed mathematical formulations in order to enhance the amplitude modulation function and to turn out its more realistic shape.

2 Origin of the Variable Transmission Path

Figure 1 highlights that, when the carrier is rotating, one planet is able to occupy different positions. It has principally two rotational motions: it revolves around its own axis (O1, Z) and it turns around the planetary gearbox centre (O, Z). The second motion originates the amplitude modulation phenomenon. Consequently, vibration signals captured by a transducer mounted on the stationary housing are affected by the instantaneous location of the planet gear.

As the time is increasing, the planet gear alternates by coming closer and going further with respect to the transducer location; when the planet gear becomes closer, the vibration energy increases and vice versa. So, the vibration signals are under amplitude modulation. The fundamental frequency that amplitude modulates the signal is equal to the carrier frequency.
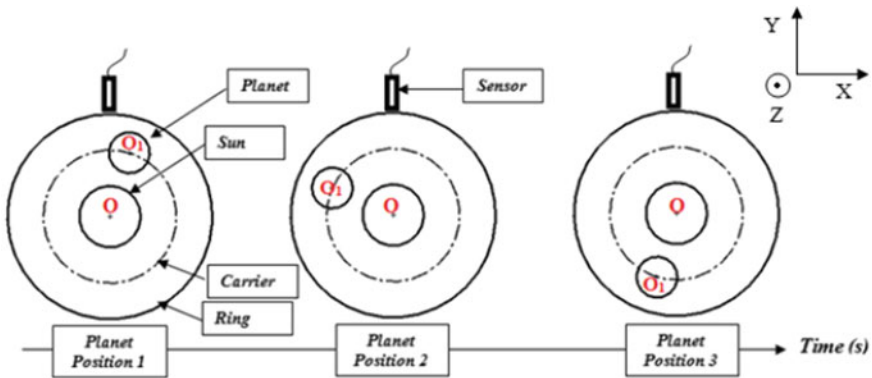

Fig. 1 Different positions occupied by planets during the rotation of the carrier

3   Mathematical Formulation of the Variable Transmission Path

The variable transmission path, in other words, the modulation function, can be formulated by two different ways:

- Evaluation of the time varying distance between the centre of the planet and the transducer location.
- Evaluation of the time varying arc separating the centre of the planet and the sensor location.

3.1   First Mathematical Formulation: Time Varying Distance

In order to quantify the variable transmission path, a first mathematical formulation can be considered based on the geometric construction given in Fig. 2.

U is the line separating the following points:

- First point: the sensor location.
- Second point: planet gear centre.

Since we investigate geometric relations of a triangle, one can apply the cosine law which gives the equation:

$$U = \sqrt{R_r^2 + R_c^2 - 2R_r R_c \sin(\theta_c)} \tag{1}$$

The vibration energy is increasing when the planet gear becomes closer to the transducer. Mathematically, this condition imposes that the distance U decreases.
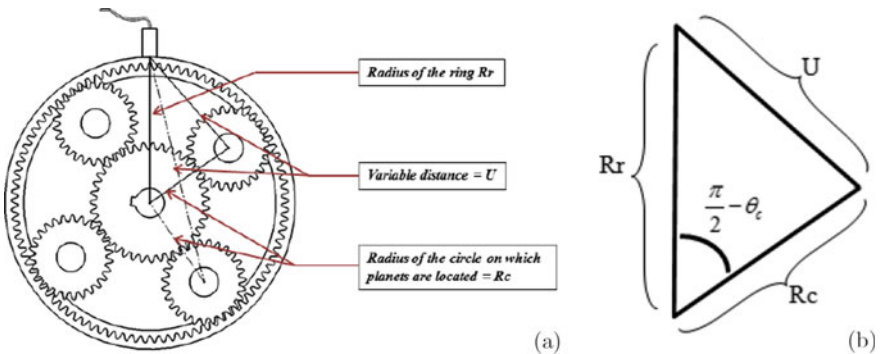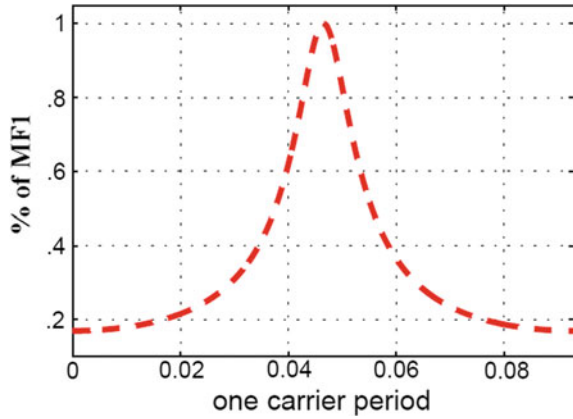

Fig. 2 Clarification of the time varying distance U, **a** planetary gearbox, **b** zoom on the triangle

Fig. 3 MF$_1$ shape

As a matter of fact, U is inversely proportional to the modulating function (MF1). Hence, the MF1 can be expressed as:

$$MF_1 = 1/U = 1/\sqrt{R_r^2 + R_c^2 - 2R_r R_c \sin(\theta_c)} \qquad (2)$$

Figure 3 shows a time representation of the MF1 within one period rotation of the carrier. As seen, it is like the Hamming function, but it is more realistic because it is derived from the planetary gearbox physical and geometric parameters given in Eq. 2.

3.2 Second Mathematical Formulation: Time Varying Arc

For the same purpose (variable transmission path quantification), a second mathematical formulation based on the geometric construction, presented in Fig. 4, is proposed.

When the planet is rotating, its vibration will go through the ring which is considered as a cylinder. Hence, in the front view presented in Fig. 4, the path can be considered as an arc. Derived from the given geometric construction, the modulation function (MF2) can be expressed as:

$$MF_2 = \frac{\frac{1}{2R_r \sin(Arc/R_r)+1}}{\max(\frac{1}{2R_r \sin(Arc/R_r)+1})} \qquad (3)$$

An offset equal to one is considered to avoid the division by zero. In addition, the MF2 is divided by its maximum to consider the percentage of the function. Figure 5 presents the MF2 shape.

Fig. 4 Clarification of time varying arc
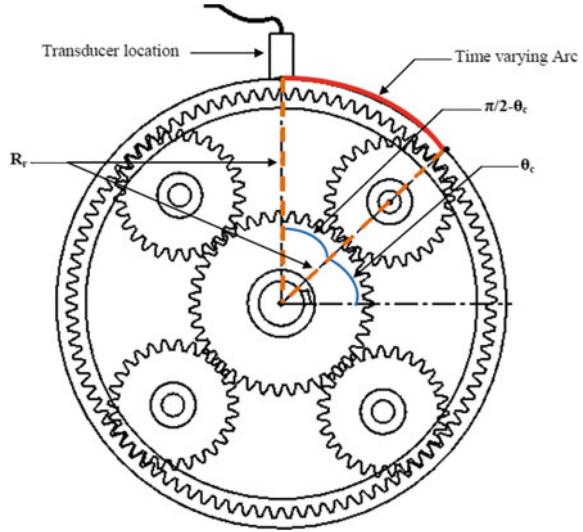
Fig. 5 MF$_2$ shape
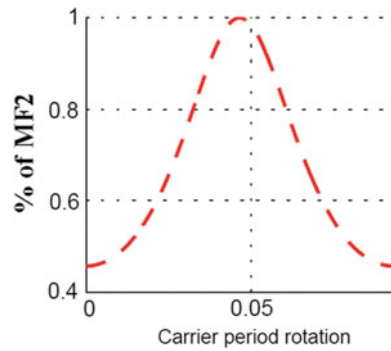
4   Comparison of the Proposed Methods

Both proposed modulating functions (MF1 and MF2) are similar in terms of shape: they are at their minimum value when the planet is at the farthest position from the transducer and reaches their maximum when the planet is at the closest position. They are like some developed functions such as the Hanning and the Hamming functions. But, as mentioned above, they are more realistic because they are expressed also as function of geometric parameters of the planetary gearbox.

4.1 Sensitivity of the Modulating Functions Due to the Change of Geometric Parameters

Since MF1 and MF2 are expressed as function of geometric parameters of the planetary gearbox, we seek to modify one of those parameters in order to investigate their influences on their shapes. For instance, a modification of Rc while keeping Rr constant is given in Table 1.

Figure 6 provides only the results of those modifications on the shape of MF1 since MF2 doesn't depend on Rc. As seen, MF1 is more sensitive to the modification of Rc. Since the radius of the ring is kept constant, bigger the radius of the carrier smaller the radius of the planet. Therefore, when increasing Rc, in other words, when the planet is smaller, the flatness of MF1 becomes narrow and the percentage of vibrations captured somehow by the sensor, when the planet is at the farthest position, is smaller.

Table 1 Modification of Rc

Rr			
Rc	1.1 × Rc	1.2 × Rc	1.3 × Rc
Red	Blue	Magenta	Black

Fig. 6 Sensitivity of MF$_1$
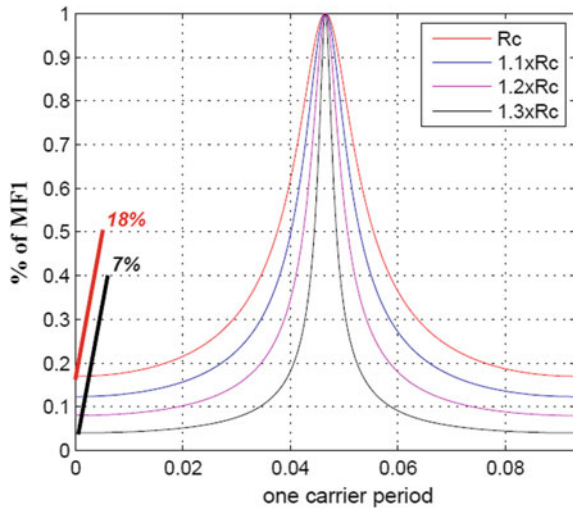
Fig. 7 Simulated spectra on Y-axis of the ring gear, **a** using MF1, **b** using MF2

4.2 Impact of MF_1 and MF_2 on Simulated Vibration Characteristics

Usually, the modulating function is used when researchers apply the methodology of combining lumped parameter model with the amplitude modulation by window function. Hence, this section aims to present simulated vibration characteristics using both proposed f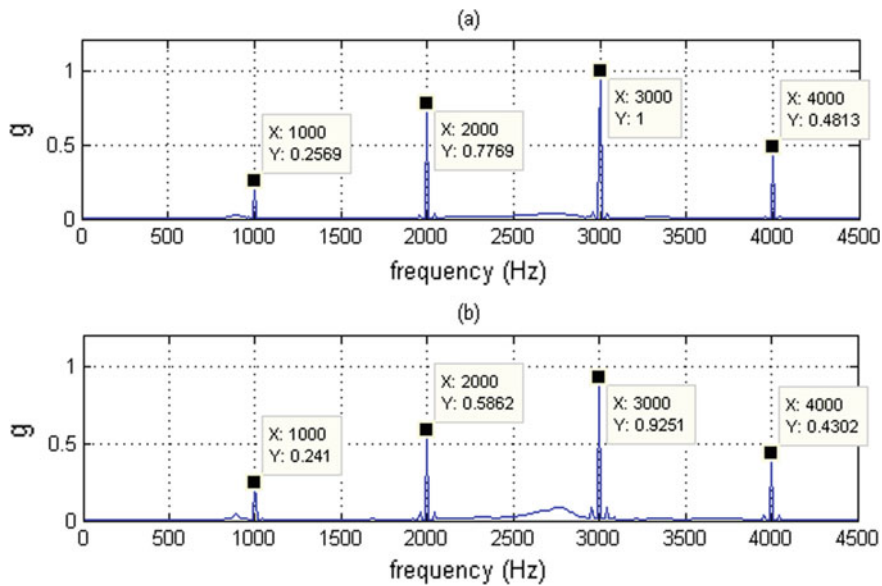unctions. Figure 7a, b present a zoom section between 0 and 4500 Hz of the simulated spectra of acceleration on Y-axis of the ring gear. The gear mesh frequency is equal to 1000 Hz.

As shown, both spectra have the same vibration characteristics in terms of gear mesh frequency components and its harmonics. Another zoom section at the third gear mesh frequency harmonic is shown in Fig. 8a, b in order to focus on the side band activity generated by both modulating functions.

Side bands are located at $GMF \pm Nf_c$ for both simulated spectra. Hence, the same behaviour is presented only in terms of frequency component locations but not in terms of energy level because by the use of the MF2, the sideband activity has bigger level of energy compared with vibration spectrum deduced by the use of MF1. Indeed, the energy of vibration signals located at the GMF and their harmonics, using the MF1, is bigger than those simulated with the incorporation of MF2 since, as mentioned in Sect. 4.1, the MF1 is more sensitive than the MF2; as a consequence, the energy level will be more and more concentrated at those frequency components.
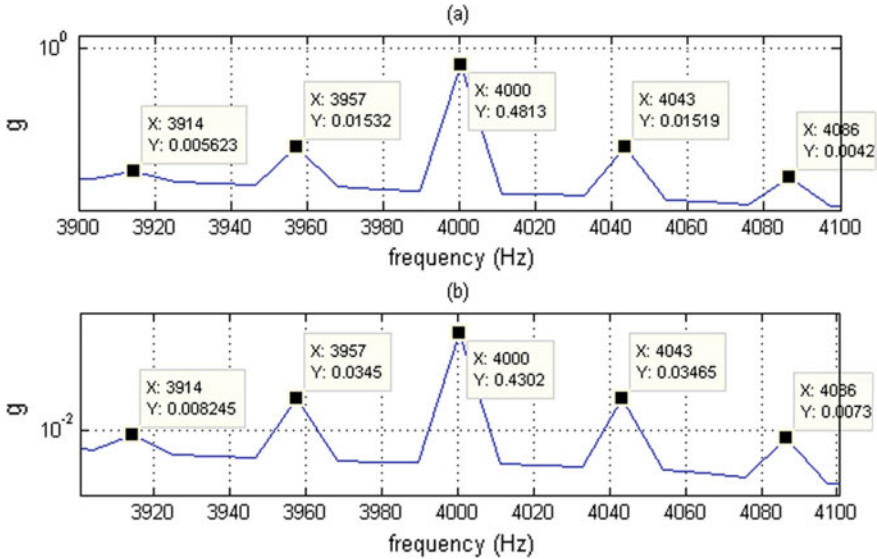
Fig. 8 Zoom section at 4000 Hz, **a** using MF1, **b** using MF2

5 Conclusion

In this paper, the variable transmission path in a planetary gearbox is investigated due to the different positions of planets. For this purpose, two mathematical formulations are developed and compared. The main conclusions of this work can be resumed as follows:

- For the modelling of the transmission path effect, not only the known functions as Hanning or Hamming are useful but also some others as MF1 and MF2 presented in this paper have similar effects on vibration characteristics.
- The presented modulation functions are given as function of both geometric and physical characteristics of the planetary gearbox which make its shape more realistic.
- The MF1 shape is more sensitive than the MF2 shape to the change of geometric parameters.
- By combining each modulation function by the same lumped parameter model, vibration characteristics are the same, but they differ only on the sideband energy level.

References

Feng Z, Zuo MJ (2012) Vibration signal models for fault diagnosis of planetary gearboxes. J Sound Vib 331:4919–4939

Graja O, Zghal B, Dziedziech K, Chaari F, Jablonski A, Barszcz T, Haddar M (2017) Modelling the transmission path effect in a planetary gearbox, rotating machinery and signal processing. SIGPROMD'2017 2017, Appl Condition Monit 12:133–142

Graja O, Zghal B, Dziedziech K, Chaari F, Jablonski A, Barszcz T, Haddar M (2019) Simulating the dynamic behaviour of planetary gearbox based on improved Hanning function. CR Mec 347(1):49–61

Guo Y, Parker RG (2010) Dynamic modelling and analysis of a spur planetary gear involving tooth wedging and bearing clearance nonlinearity. Eur J Mech A Solids 29:1022–1033

Inalpolat M, Kahraman A (2009) A theoretical and experimental investigation of modulation sidebands of planetary gear sets. J Sound Vib 323:677–696

Inalpolat M, Kahraman A (2010) A dynamic model to predict modulation sidebands of a planetary gear set having manufacturing errors. J Sound Vib 329:371–393

Liang Z, Zuo MJ, Hoseini MR (2015) Vibration signal modelling of a planetary gear set for tooth crack detection. Eng Fail Anal 48:185–200

Liu L, Liang X, Zuo MJ (2016) Vibration signal modelling of a planetary gear set with transmission path effect analysis. Measurement 85:20–31

Prashant S, Kahraman A (2013) A dynamic model of a double-helical planetary gear set. Mech Mach Theory 70:157–174

Sensitivity Analysis of Porous Material Using the Mixed Formulation

Mohamed Riadh Letaief, Lassaad Walha, and Mohamed Haddar

Abstract The porous materials are commonly used as a solution to increase the sound comfort in several systems especially in the automotive industry. Most of the models that describe their behavior use 5 or 6 and even 9 intrinsic parameters of the materials. The most generalized model is that defined through the nine intrinsic parameters that are: porosity, tortuosity, flow resistivity, thermal and viscous characteristic dimensions of pores, density of frame, shear modulus, Poisson coefficient and damping coefficient. In this paper we present a sensitivity study of materials to intrinsic parameters as a function of frequency. Methods used here is Sobol algorithms. Model studied is the mixed formulation for porous materials (depends on 9 intrinsic parameters). Obtained results show a hierarchy strongly depending on frequency. On the other hand, sensitivity analysis ensures that the materials acoustic absorption is largely dominated by the resistivity.

Keywords Porous material · Sensitivity analysis · Mixed formulation

1 Introduction

Sound comfort has become a competitive advantage during the design phase of rotating systems. To do this a study of vibro-acoustic behavior is essential. This study will allow us to control this behavior and subsequently to predict it. Porous materials are mainly used as a solution to isolate noise sources and then reduce sound levels due to their ability to attenuate the vibro-acoustic level. But given their biphasic structure is still more complicated to model them, In fact several models describe the acoustic propagation in a porous material. One of the simplest to implement is the

M. R. Letaief (✉) · L. Walha · M. Haddar
Mechanical, Modeling and Manufacturing Laboratory LA2MP, National School
of Engineers of Sfax, Sfax, Tunisia
e-mail: riadh.med@gmail.com

L. Walha
e-mail: walhalassaad@yahoo.fr

M. Haddar
e-mail: mohamed.haddar@enis.rnu.tn

model of Delany and Bazley (1970). But this model does not take into account the vibration of the skeleton and it is valid only for the tested material. To express the dissipative effects, a function of viscous form, not depending to the geometric nature of the skeleton, was introduced Johnson et al. (1987). The viscous characteristic length introduces the viscous dissipation, which is an intrinsic parameter of the material that can be obtained by experiment. Champoux and Allard (1991) introduce the thermal characteristic length as is an intrinsic parameter expressing the thermal effects. In 1997, Lafarge et al. (1997) to improve thermal effects at low frequencies introduces thermal permeability. But, the model with rigid structure is not suitable in the case of deformed or mobile skeleton of the material which is presented in many applications where porous material is directly subjected to a mechanical or acoustic wave excitation. The numerical implementation of porous model are enormously expensive in terms of simulation time. The indicator, which qualifies the acoustic performance of a porous material, is the sound absorption coefficient. We expresses the sound absorption coefficient as a function of the surface impedance, and this surface impedance depends on the characteristic impedance and the wave number. These latter can express themselves according to the effective density and dynamic compressibility.

We propose in this work a sensitivity analysis of nine intrinsic parameters on the acoustic performance of porous materials. To do this, we use sensitivity methods that quantify the variance of the parameters on the responses of a system. This sensitivity includes the calculated value of the sensitivity factor of the first order and adding the factor or interaction occurs. The method used is Sobol. Here, the investigation concerns the study of the mixed formulation, giving access to the surface impedance and absorption coefficient. Since the model is harmonic, the sensitivity will also depend on the frequency.

We read this article as follows: the first describes Atalla model and so called mixed formulation. Then we present sensitivity analysis by the Sobol indices method. The results and their interpretations are described in Part 4 of this paper.

2 The Mixed Formulation

In order to alleviate the cumbersome calculations, formulation of mixed type have been implemented. It is developed by Atalla et al. (1998) using the classical equations of Biot (1962) with u represents the solid phase displacement field and p is the pore pressure instead of u and v which represent respectively the solid and the fluid phase displacement field in the classical Biot formulation. In terms of finite element calculation, this means that using this formulation we can pass from 6 to 4 degrees of freedom per node. The mixed formulation is valid only for a harmonic motion. The modified equations of equilibrium (for small harmonic oscillations) are as follows:

$$\overbrace{\hat{\sigma}_{ij/j}^{S} + \omega^2 \tilde{\rho}\, u_i}^{\text{skeleton 'in vacuo' behavior}} + \overbrace{\tilde{\gamma}\, p_{/i}}^{\text{coupling term}} = 0\sqrt{b^2 - 4ac} \tag{1}$$

$$\underbrace{-\omega^2 \frac{\tilde{\rho}_{22}\tilde{\gamma}}{\phi^2} u_{i/i}}_{\text{coupling term}} + \underbrace{\omega^2 \frac{\tilde{\rho}_{22}}{\tilde{\lambda}^f} p}_{\substack{\text{fluid behavior when}\\\text{the frame is motionless}}} + p_{/ii} = 0 \tag{2}$$

$\hat{\sigma}_{ij}^{s}$ is the stress tensor of the material "in vacuum", it does not depend on the fluid phase:

$$\hat{\sigma}_{ij}^{s} = \hat{\tilde{\lambda}}^{s}\varepsilon_{kk}^{s}\delta_{ij} + 2\mu^{s}\varepsilon_{ij}^{s} \tag{3}$$

$$\varepsilon_{ij}^{s} = \frac{1}{2}\left(u_{i|j} + u_{j|i}\right) \tag{4}$$

Above equations depend on certain factors: $\hat{\tilde{\lambda}}^{S}$, $\tilde{\rho}$, $\tilde{\gamma}$ and $\tilde{\lambda}^f$. These are based on hard poroelastic characteristics (Horoshenkov and Swift 2001; Umnova et al. 2001).

The acoustic absorption coefficient which is expressed as follows:

$$\alpha = 1 - \left|\frac{Z_S - Z_0}{Z_S + Z_0}\right|^2 \tag{5}$$

where $Z_0 = \rho_0 c_0$ is air impedance.

Surface impedance Z_S at normal incidence is defined as the complex ratio of the acoustic pressure and total velocity at the impinged face. Since the amplitude of the incident pressure front is 1 Pa and considering the propagation axis to be x_3, Z_S can be stated as in Eq. (6).

$$Z_S(\omega) = \left[j\omega\left\{\frac{\phi^2}{\omega^2\tilde{\rho}^{22}}p_{,3} + \left(1 - \phi\left(1 + \frac{\tilde{\rho}^{12}}{\tilde{\rho}^{22}}\right)\right)u_3\right\}\right] \tag{6}$$

The analytical resolution allows writing surface impedance as in the following form:

$$Z_S = -j\frac{\left(Z_1^s Z_2^f \mu_2 - Z_2^s Z_1^f \mu_1\right)}{D} \tag{7}$$

given that δ_1 and δ_2 are fluid and solid phases wave numbers and $\left(Z_1^f, Z_2^f, Z_1^s, Z_2^s\right)$ are characteristic impedances and (μ_1, μ_2) are ratios between velocity in solid and velocity in air for the two compression waves. This parameters formula are operated by Letaief et al. (2017) using poroelastic material characteristics.

3 Sensitivity Analysis

In this section, we define the sensitivity index in general. We give the general expressions of the sensitivity indices of first order and total. Consider the model

$$Y = f(X_1, \ldots, X_p) \tag{8}$$

where the input variables are independent.

(X, Y) is couple of random variables, where Y takes values in R and X_i in a finite or countable set, or in $\mathbb{R}$ or $\mathbb{R}^p$. If the variance of Y is finite, then:

$$V(Y) = V[E\langle Y \mid X_i \rangle] + E[V\langle Y \mid X_i \rangle] \tag{9}$$

And that's how an sensitivity indicator of Y at X_i will be the variance of the expectation of Y conditionally at X_i: $V[E(Y|X_i)]$. More X_i will be important, the more this quantity will be large. In order to use a standardized indicator, we finally define the sensitivity index of Y at X_i:

$$S_i = \frac{V[E\langle Y|X_i \rangle]}{V(Y)} \tag{10}$$

This index is called first-order sensitivity index by Sobol (1993), correlation ratio by McKay (1995), or even importance measure. It quantifies the sensitivity of the output Y to the input variable X_i, or the variance part of Y due to the variable X_i.

La variance du modèle à entrées indépendantes (8) se décompose en:

$$V = \sum_{i=1}^{p} V_i + \sum_{1 \leq i < j \leq p} V_i + \cdots + V_{1\ldots p} \tag{11}$$

$$V[E\langle Y \mid X_i \rangle]$$
$$V_{ij} = V\big[E\langle Y \mid X_i, X_j \rangle\big] - V_i - V_j$$
$$V_{ijk} = V\big[E\langle Y \mid X_i, X_j, X_k \rangle\big] - V_{ij} - V_{ik} - V_{jk} - V_i - V_j - V_k$$
$$\cdots$$

$$V_{i\cdots p} = V - \sum_{i=1}^{p} V_i - \sum_{1 \leq i < j \leq p} V_{ij} - \cdots - \sum_{1 \leq i_1 < \cdots < i_{p=1} \leq p} V_{i_1 \cdots i_{p-1}} \tag{12}$$

Thus, it is possible to define first-order sensitivity indices:

$$S_i = \frac{V_i}{V} = \frac{V[E\langle Y \mid X_i \rangle]}{V} \tag{13}$$

the second order sensitivity indices:

$$S_{ij} = \frac{V_{ij}}{V} \qquad (14)$$

which express the sensitivity of the variance of Y to the interaction of the variables X_i and X_j. The third order sensitivity indices are defined by:

$$S_{ijk} = \frac{V_{ijk}}{V} \qquad (15)$$

which express the sensitivity of the variance of Y to the variables X_P, X_h and X_j which is not taken into account in the effect of the variables alone and the interactions 2 to 2. And so on up to the order p.

Homma and Saltelli (1996) then introduced total sensitivity indices, which express the total sensitivity of the variance Y to a variable. The total sensitivity index ST_i at the variable X_i is defined as the sum of all the sensitivity indices relative to the variable X_i:

$$ST_i = S_i + \sum_{i \neq j \neq k} S_{ijk} \qquad (16)$$

where i, j, k represent all index sets containing the index i.

For example, for a model with three input variables, we have:

$$ST_1 = S_1 + S_{12} + S_{13} + S_{123} \qquad (17)$$

For more details on the Sobol method, the reader can refer to the papers Sobol (1993).

The knowledge of the total sensitivity indexes makes it possible to classify the importance of the parameters on the model in question. Parameters whose index is greater than 0.8, they are considered very important. In the case where the index is between 0.5 and 0.8, the parameters are considering important, whereas if they vary between 0.5 and 0.8, they are not important. Finally, in the case where the total sensitivity index is less than 0.3, the parameter is insignificant.

4 Results and Interpretations

The sensitivity analysis is carrying out on this model by Sobol method. To carry out our sensitivity index calculations. Table 1 presents the inventory of the intrinsic parameters.

Figure 1 shows the general shape of the sound absorption coefficient as a function of the frequency for two different porous materials.

As is shown Fig. 2, two points are worth quoting following these graphs. First, we can appreciate the importance of coupling parameters throughout the frequency

Table 1 Inferior and superior limits of poroelastic parameters

Parameter	Unity	Inferior limit	Superior limit
ρ_1	kg/m^3	8	200
ϕ	—	0.7	0.99
σ	N sm^{-4}	1500	200,000
α_∞	—	1	3
ν	—	0	0.44
Λ	µm	5	200
Λ'	µm	5	400
E	N/m^2	1000	5,000,000
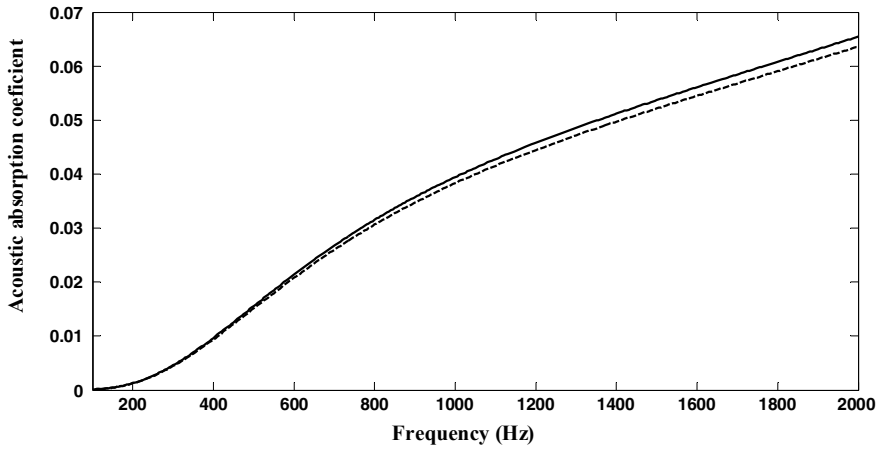
Fig. 1 Acoustic absorption coefficient
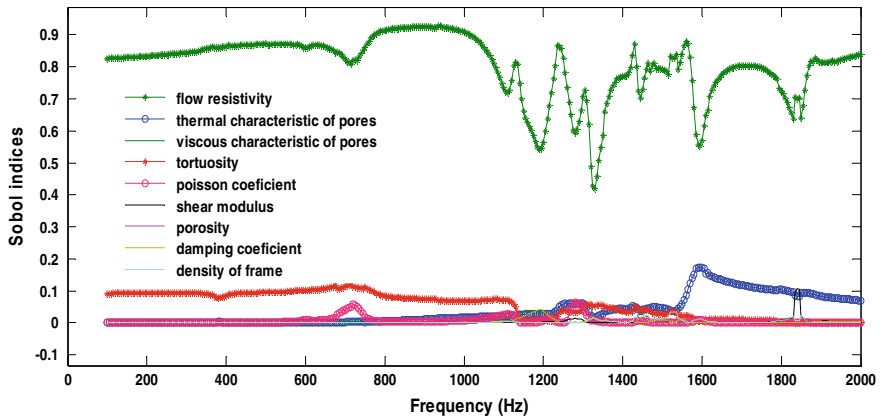
Fig. 2 Evolution of the sensitivity index as a function of frequency

scale. The second interesting point is the importance of interactions between intrinsic parameters on acoustic performance between 1100 and 1600 Hz.

For the acoustic absorption coefficient, the resistivity will keep a total sensitivity between 87 and 98% throughout the frequency scale. The porosity and the tortuosity have between 3 and 7% of influence each on the acoustic absorption, the characteristic thermal length between 1 and 4.5%, and the viscous characteristic length between 4 and 17% of sensitivity total.

By studying the sensitivity of the intrinsic parameters on the acoustic absorption coefficient, we can conclude that the interactions involving porosity constitute 74% of the total sensitivity index of the parameter in question. In fact, the resistivity indexes can be up to 8% and those of the tortuosity up to 95%, while for the characteristic viscous length can go up to 47%. Finally the sensitivity index of the characteristic thermal length can reach 92% of the total sensitivity index. However, this study shares the same idea of Delany and Bazeley (1970) where the flow resistivity remains dominant and the most influential on the acoustic performance of a porous material.

5 Conclusion

The study presented here concerns the hierarchy of the nine intrinsic parameters by studying the mixed formulation which describes the acoustic behavior of porous materials. The results showed on the one hand a strong dependence of the sensitivity indices as a function of the frequency, and on the other hand, the strong dependence of the acoustic characteristics of the flow resistivity. Following these results, and quantitatively, sensitivities (including existing interactions) intrinsic parameters are known.

References

Atalla N, Panneton R, Debergue P (1998) A mixed displacement-pressure formulation for poroelastic materials. J Acoust Soc America 104(3):1444–1452

Biot MA (1962) Mechanics of deformation and acoustics propagation in porous media. J Appl Phys 33:1482–1498

Champoux Y, Allard JF (1991) Dynamic tortuosity and bulk modulus in air-saturated porous media. Appl Phys 70(4):1975–1979

Delany ME, Bazley EN (1970) Acoustic properties of fibrous absorbent materials. Appl Acoust 3:105–116

Homma T, Saltelli A (1996) Importance measures in global sensitivity analysis of non linearmodels. Reliab Eng Syst Saf 52:1–17

Horoshenkov K, Swift MJ (2001) The acoustic properties of granular materials with pore size distribution close to log-normal. J Acoust Soc Am 110:2371–2378

Johnson DL, Koplik J, Dashen R (1987) Theory of dynamic permeability and tortuosity influid-saturated porous media. J Fluid Mech 176:379–402

Lafarge D, Lemarinier P, Allard JF, Tarnow V (1997) Dynamic compressibility of air in porous structures at audible frequencies. J Acoust Soc Am 102(4):1995–2006

Letaief MR, Walha L, Taktak M, Chaari F, Haddar M (2017) Porous material effect on gearbox vibration and acoustic behavior. J Theor Appl Mecanics (JTAM) 55(4):1381–1395

McKay MD (1995) Evaluating prediction uncertainly. Technical report NUREG/CR-6311, US Nuclear Regulatory Commission and Los Alamos National Laboratory

Sobol IM (1993) Sensitivity estimates for nonlinear mathematical models. Math Model Comput Exp 1:407–414

Umnova O, Attenborough K, Li KM (2001) A cell model for the acoustical properties of packings of spheres. Acta Acust United Ac 87(2):226–235

Analysis of a Three Dimensional Multiphysics System—Application to Thermo-Mechanical Simulation of Shearing

Sonda Moakhar, Hamdi Hentati, Maher Barkallah, Jamel Louati, and Mohamed Haddar

Abstract Numerical simulation is nowadays an effective tool to satisfy the increasing precision requirements of metal working industry. The modelling of a single industrial process involves many interacting variables from different physical fields (thermal, chemical, mechanical, fluid, electromagnetic …). The finite element analysis of bar shearing is a typical case of multiphysics. It involves basically thermal and mechanical interrelated phenomenon. The elevated deformation rate induces a rapid temperature increase in the shear zone. High Temperature has also an evident effect on mechanical characteristics of sheared material. The thermo-mechanical coupled modelling is thus necessary for the accuracy of the simulation. The aim of this paper was to present an insight into modelling a multiphysics system and focuses on coupled thermo-mechanical finite element analysis of shearing and the respective governing equations. The Johnson-Cook plasticity and failure models were adopted for modelling and predicting material flow behavior and ductile rupture. These models are consistent under coupled effects of strain, strain rate and temperature. The bar material was the Al7075-T6 which is a high strength aluminum alloy widely used for highly stressed mechanical components. The results of a shearing simulation were presented including the evolution of force and temperature distribution. The developed model can be used to optimize bar shearing, and valuable prediction results for geometrical and microstructural evolution can be achieved.

Keywords Multiphysics · Thermo-mechanical coupling · Finite element method · Explicit analysis · Shearing

1 Introduction

Bar shearing process is widely used in the metalworking industry to produce semifinished billets. The improvement of the result of this process requires a preliminary numerical analysis and experimental tests. To generate a suitable modelling of the

S. Moakhar (✉) · H. Hentati · M. Barkallah · J. Louati · M. Haddar
Research Laboratory of Mechanics, Modeling and Manufacturing (LA2MP),
National School of Engineers of Sfax, Sfax, Tunisia
e-mail: sonda.moakhar@stud.enis.tn

process, the consideration of the main interacting phenomenon and an accurate material modelling are required. Finite element analysis has been improved along the last decades: from structural two-dimensional to multiphysics three-dimensional analysis in addition to the consideration of failure and microstructural changes. Maiti (1982) first applied finite element method (FEM) to examine the influence of shearing process parameters on the geometry of the sheared surface employing two-dimensional elements and linear elastic fracture mechanics. Breitling et al. (1997) built some two-dimensional simulations including fracture behavior of rectangular bar shearing and tested the influence of several process parameters on the sheared surface as well as the prediction of shearing stages. Hu et al. (2018) have used a three-dimensional model to test the influence of different cropping strategies on the sheared billet quality. Their model included fracture behavior. FEM simulation was useful to predict the billet geometry, but the thermal aspect was neglected in most of the previous numerical studies on bar shearing. The improvement of shear surface quality and the process productivity require an elevated shearing rate up to 10 m/s. This fact induces an adiabatic heating in the shear zone which affects material properties and has consequence on flow and failure behavior. Temperature distribution and material properties are thus dependent from each other especially in friction and shear zones. A coupled thermo-mechanical modelling is necessary to analyze shearing process. To this purpose the brick elements with coupled displacement temperature were used in the FEA of bar shearing. The dependency of material behavior on temperature and shear rate was also taken into account by using Johnson-Cook plasticity and damage models. Generally, multiphysics problems are solved with virtual work principle. An overview about multiphysics computation strategies was presented in Sect. 2. In Sect. 3 the governing equations of the studied thermo-mechanical system were exposed. A simulation of bar shearing was finally performed on ABAQUS/Explicit in Sect. 4 to make in evidence the interactions between temperature distribution and mechanical force.

2 Fundamentals of Numerical Multiphysics Systems

The discretization of a physical system leads to writing its algebraic governing equations in matrix form (Xiaoguang 2015):

$$[K]\{X\} = \{F\} \tag{1}$$

where $\{X\}$ is the unknowns vector like displacements and temperature, $[K]$ is the stiffness matrix and $\{F\}$ is the force vector. In the case of linear equations, solving the problem means inverting $[K]$ matrix and calculating $\{X\} = [K]^{-1}\{F\}$. But in the case of nonlinearity, matrix inversion is impossible and the problem has to be solved on a number of steps called increments. Nonlinearities can be material, geometric or in the boundary conditions. In multiphysics simulations, many physical fields intervene simultaneously and interact with each other which create nonlinearities. When

the variable's flow has a single direction from a subsystem to another, the coupling is called weak and the problem can be sequentially solved. When the different subsystems depend from each other, the coupling is called strong. The matrix form of a strong coupled system can be written as following:

$$\begin{bmatrix} [K_{MM}] & [K_{MT}] \\ [K_{TM}] & [K_{TT}] \end{bmatrix} \left\{ \begin{array}{c} \{X_M\} \\ \{X_T\} \end{array} \right\} = \left\{ \begin{array}{c} \{F_M\} \\ \{F_T\} \end{array} \right\} \tag{2}$$

where $\{X_T\}$ and $\{X_M\}$ are respectively the thermal and mechanical vectors of unknown variables, $[K_{ij}]$ is the coefficient sub-matrix relating filed i to field j, $\{F_T\}$ and $\{F_M\}$ are load vectors, M designates mechanical field and T designates thermal field. In weak coupled system the off-diagonal coefficient terms $[K_{TM}]$ and $[K_{MT}]$ have the value zero.

Resolution method of nonlinear time dependent problems can be implicit or explicit. Implicit solving is effective when the problem is static. The calculation is incremental and iterative. That means: at each time step, the solution depends on the previous time step solution. Explicit solving is needed when the velocity effect is not negligible. The calculation is only incremental, with small increments. The computation using Newton-Raphson procedure continues even if equilibrium conditions are not attained at a given time step.

3 Governing Equations of a Thermal-Structural Multiphysics System

When the studied process involves structural deformation that dissipate heat, which affects the material properties, a strong coupling between thermal and mechanical domains is necessary to build the numerical model. Such interactions are found in shearing. To understand the modeling of shearing process, the governing equation of both thermal and mechanical domains are given in this section.

3.1 Thermodynamic Theory

Assume a solid with volume $V \subset \Re^3$, the governing thermal equation that describes temperature equilibrium between external and internal heat fluxes reads:

$$\rho C p \dot{T} = -divq + Q \tag{3}$$

where ρ is the density, C_p is the specific heat, $\dot{T}$ is the temperature time derivative, div is the divergence operator, q is the heat flux through the body, and Q is the internal heat generation rate per unit deformed volume.

In many forming processes with large deformation, heating is generated from friction between tool and work piece as well as from plastic straining. Taking into consideration Fourier's conduction equation and heat flux splitting (Gouge and Michaleris 2017), the thermal energy conservation Eq. (3) is rewritten as follows:

$$\rho Cp\dot{T} - div(k\nabla T) - \eta_p\sigma : \dot{\varepsilon}_{pl} - Q_f = 0 \tag{4}$$

where k is the isotropic temperature dependent thermal conductivity, ∇ is the gradient operator, σ is the stress tensor, $\dot{\varepsilon}_{pl}$ is the plastic strain rate,: is the double inner product of two tensors, η_p is the Taylor-Quinney factor that designates the fraction of plastic work converted into heat and Q_f is the heat flux generated from friction work.

The weak variational form of the thermodynamic equilibrium can be written as a function of an arbitrary temperature variation δT:

$$\int_V \rho C_p \dot{T}\delta T dV - \int_V div(k\nabla T)\delta T dV - \int_V \eta_p\sigma : \dot{\varepsilon}\delta T dV - \int_V Q_f\delta T dV = 0 \tag{5}$$

3.2 Mechanical Theory

In this section, the equations of the mechanical equilibrium are presented.

- The governing motion equation in a dynamic system:

$$\nabla\sigma + f_v = \rho\ddot{u} \tag{6}$$

where σ is the stress tensor obtained from the constitutive law, f_v is the body force density, $\ddot{u}$ is the acceleration.

- The kinematic compatibility equation:

$$\dot{\varepsilon} = \frac{1}{2}\left(\nabla\dot{u} + (\nabla\dot{u})^T\right) \tag{7}$$

- Strain splitting into elastic, plastic and thermal parts:

$$\varepsilon = \varepsilon^{el} + \varepsilon^{pl} + \varepsilon^{th} \tag{8}$$

- The constitutive equation of stress-strain relation, represented here with the Johnson-Cook plasticity model. This model allows to consider the thermo-visco-plastic behavior which is necessary by the simulation of processes with high deformation, high deformation rates and high temperature changes.

$$\tilde{\sigma}\left(\varepsilon_p, \dot{\varepsilon}, T\right) = \left[A + B\left(\varepsilon_p\right)^n\right]\left[1 + C\ln\left(\frac{\dot{\varepsilon}}{\dot{\varepsilon}_0}\right)\right]\left[1 - \left(\frac{T - T_0}{T_m - T_0}\right)^m\right] \quad (9)$$

where A, B, C, n and m are material constants, ε_p is the von Mises equivalent plastic strain, $\dot{\varepsilon}$ is the strain rate, $\dot{\varepsilon}_0$ is the reference strain rate, T_m is the melting temperature and T_0 is the reference ambient temperature.

- The ductile rupture is modelled with the Johnson-Cook damage criterion which is suitable to shearing simulation because it makes fracture strain depending on stress state, represented with the stress triaxiality ratio (Tr), on velocity and temperature change.

$$\varepsilon_p^f(Tr, \dot{\varepsilon}, T) = \left[D_1 + D_2 e^{D_3 Tr}\right]\left[1 + D_4\ln\left(\frac{\dot{\varepsilon}}{\dot{\varepsilon}_0}\right)\right]\left[1 - D_5\left(\frac{T - T_0}{T_m - T_0}\right)\right]$$
$$(10)$$

where ε_p^f is the plastic strain at fracture and $D_1 - D_5$ are material constants determined from specific characterization tests. The fracture takes place when the cumulative damage parameter D attains the value 1. This parameter can be calculated as follows:

$$D = \sum\left(\frac{\Delta\varepsilon}{\varepsilon^f}\right) \quad (11)$$

where $\Delta\varepsilon$ is the cumulated plastic deformation and ε_f is the fracture strain. $D \in [0;1]$. The damage affects material behavior and reduces material strength.

- Contact condition is modeled with the combined model that uses coulomb friction on the sliding region and the constant shear friction factor model on the sticking region:

$$\tau_f = \begin{cases} \mu\sigma_n & if \quad \tau_f < \tau_{max} \\ mk_f & if \quad \tau_f \geq \tau_{max} \end{cases} \quad (12)$$

where τ_f is the shear friction stress, σ_n is the normal friction stress, μ is the Coulomb friction factor, m is the shear friction factor, k_f is the shear flow stress and τ_{max} is the maximal shear stress.

- Stress boundary condition:

$$\sigma n = s \tag{13}$$

where s is the stress vector and n is the unit outward normal to a boundary element on the stress surface.

- The variational weak form can be obtained from the principle of Alembert. This statement allows to study the stability and the equilibrium of a dynamic system composed from many interconnected components (Lestriez 2003). It states that when a continuum solid is subjected to infinitesimal virtual displacement, the total virtual work from external and internal forces vanishes (Leine et al. 2009).

$$-\int_V \sigma\delta\dot{u}dV + \int_V f_v\delta u dV + \int_{S_c} F_f\delta u dS + \int_{S_\sigma} s\delta u dS - \int_V \rho\ddot{u}\delta u dV = 0 \tag{14}$$

3.3 Global Formulation

To relate all of the involved variables and to solve the unknown field values, the variational equation are assembled as follows:

$$\begin{cases} F(u, T, \delta u) = -\int_V \sigma\delta\dot{u}dV + \int_V f_v\delta u dV + \int_{S_c} F_f\delta u dS \\ \qquad\qquad + \int_{S_\sigma} s\delta u dS - \int_V \rho\ddot{u}\delta u dV = 0 \\ G(u, T, \delta T) = \int_V \rho C_p\dot{T}\delta T dV - \int_V div(k\nabla T)\delta T dV \\ \qquad\qquad - \int_V \eta_p\sigma : \dot{\varepsilon}\delta T dV - \int_{S_c} Q_f\delta T dS = 0 \end{cases} \tag{15}$$

The objective of the variational formulation is to minimize the functions $F(u, T, \delta u)$ and $G(u, T, \delta T)$ to solve the multiphysics problem.

3.4 FEM Discretization

The considered finite element analysis has three sources of nonlinearity: material nonlinearity, contact nonlinearity and geometrical nonlinearity. The main methods to compute the solution of nonlinear equations are: the iterative splitting method, which splits every iteration into elastic predictor and plastic corrector, and the Newton's method which is applied in ABAQUS and in the current study.

To simplify the model, the continuum system was discretized in time, by dividing the period into intervals Δt, and discretized in the space by dividing the geometry into n finite elements.

3.4.1 Time Discretization

In a coupled thermo-mechanical problem, the stability is assured with setting the step time limit smaller than the critical time limit of both mechanical and thermal subsystems (Abaqus Help 2013). When no damping exists in the mechanical solution response, the time step has the following limit:

$$\Delta t \leq min\left(\frac{2}{\omega_{max}}, \frac{2}{\lambda_{max}}\right) \tag{16}$$

where ω_{max} is the highest eigenvalue of the mechanical subsystem and λ_{max} is the highest eigenvalue in the thermal subsystem. The time increment is calculated as follows:

$$\Delta t \approx \frac{L_{min}^2}{2\alpha} \tag{17}$$

where L_{min} is the smallest element dimension and α is the thermal diffusivity of the material (Abaqus Help 2013).

3.4.2 Spatial Discretization

In order to analyze the coupling between physical and thermal phenomenon in 3D shearing modelling, the hexahedron continuum linear element with coupled displacement-temperature C3D8T from Abaqus library was adopted. It has four degrees of freedom (DOF): displacements in the three special directions and temperature. This element is fully integrated i.e. Gaussian integration are established at each of the 8 nodes at every increment. Figure 1 shows the isoparametric coordinate system and the corner nodes numbering of a first-order brick element in Abaqus.

The nodal coordinates (x_{ik}), nodal displacements (u_{ik}) and nodal temperatures (T_k) are reformulated in the isoparametric coordinate system (ξ, η, ζ) using the same shape functions ϕ_k.
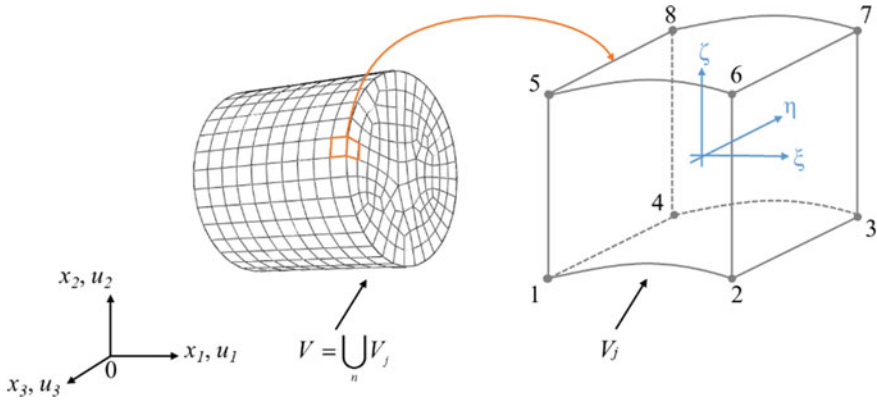
Fig. 1 Spatial discretization with isoparametric brick element

$$
\begin{cases}
x_i = x_{ik}\varphi_k(\xi, \eta, \zeta) \\
u_i = u_{ik}\varphi_k(\xi, \eta, \zeta) \quad i = 1, 2, 3; \quad k = 1, \dots 8; \quad -1 \le \xi, \eta, \zeta \le 1 \\
T = T_k\varphi_k(\xi, \eta, \zeta)
\end{cases}
\tag{18}
$$

4 Numerical Example of Three-Dimensional Shearing Simulation

4.1 Finite Element Model for Shearing

The purpose of the simulation is to study shearing operation. So a cylindrical bar is fixed horizontally between bar blade and bar holder and sheared with a vertical moving closed section blade which velocity is 10 m/s. In order to reduce the calculation cost, only the half of the geometry was modelled using a symmetry plane parallel to the shearing force. The geometry and meshing of the model are similar to the model of Moakhar et al. (2019a). The clearance between the blades was set to 0.5 mm and the initial temperature was 20 °C. In shearing simulation, two physical subsystems are involved: the thermal one and the mechanical one. The effect of strain rate is important that's why the explicit calculation method was necessary. A strong thermo-mechanical coupling is required because of the interaction between mechanical and thermal variables. On the one hand, bar material properties and the induced stress state in the bar are dependent on temperature. On the other hand, when shear rate is elevated, a part of deformation energy is converted into heat. This phenomenon is mathematically applicable with the consideration of the inelastic heat fraction equal to 0.9. An adiabatic phenomenon is observed in the shear zone, where high temperature is concentrated.

The bar material is the Al7075-T6, which was modelled as an elastic-viscoplastic material with nonlinear strain hardening. The material flow behavior and failure strain were modelled with the constitutive equations of plasticity and damage of Johnson-Cook (Eqs. 9 and 10). The material constants were determined in the study of Brar et al. (2009) from tension tests on smooth and notched bars at different strain rates and temperatures. In general, material modelling for shearing simulation should include compression, shear and tension stress states because all of these states are involved in the shear zone during shearing and induce different rupture mechanisms (Moakhar et al. 2019b). The contact between tool and work piece as well as the self-contact in the shear zone were modelled with the combined Coulomb-Tresca friction model (Eq. 12) assuming $\mu = 0.2$ and $m = 0.45$.

4.2   Simulation Results and Discussion

The shearing model have been performed according to the settings mentioned above. Figure 2 shows the force-displacement curve to understand the different phases in the process. Generally, shearing operation consists in four main stages (Dalloz 2007): elastic deformation (0–1), plastic deformation and hardening (1–2), plastic deformation with section reduction (2–3) and crack propagation until total separation of the billet (3–4).

The shear force increases with advancing movement of the tool until point (2) because of the strain hardening. After crack initiation in (3), the shear force decreases because of the degradation of the material strength due to damage and thermal softening. The plastic deformation is converted into heat in the shear zone where the temperature attains its maximal value 606 °C at the point (4). Furthermore, friction between sectioned billet and bar-rest generates local heating. Consequently, the temperature remains elevated in the shear zone even after total separation. Temperature depends thus on the stress evolution and vice versa. In the interface between tools and bar, there was no significant temperature increase. Temperature increase can induce microstructural change of the material in the shear zone. The FEA of the quality of sheared surface may be ameliorated when microstructural evolution is considered in the material modelling.

5   Conclusion

Bar shearing was modelled with three-dimensional finite element method. Stability was provided using an explicit coupled strategy. The mechanical and thermal governing equations as well as the discretization method were presented. The results of the simulation showed the necessity of using a coupled thermo-mechanical numerical modelling to analyse the shearing operation. It was demonstrated that high strain is concentrated in the shear zone and an important part of the plastic deformation
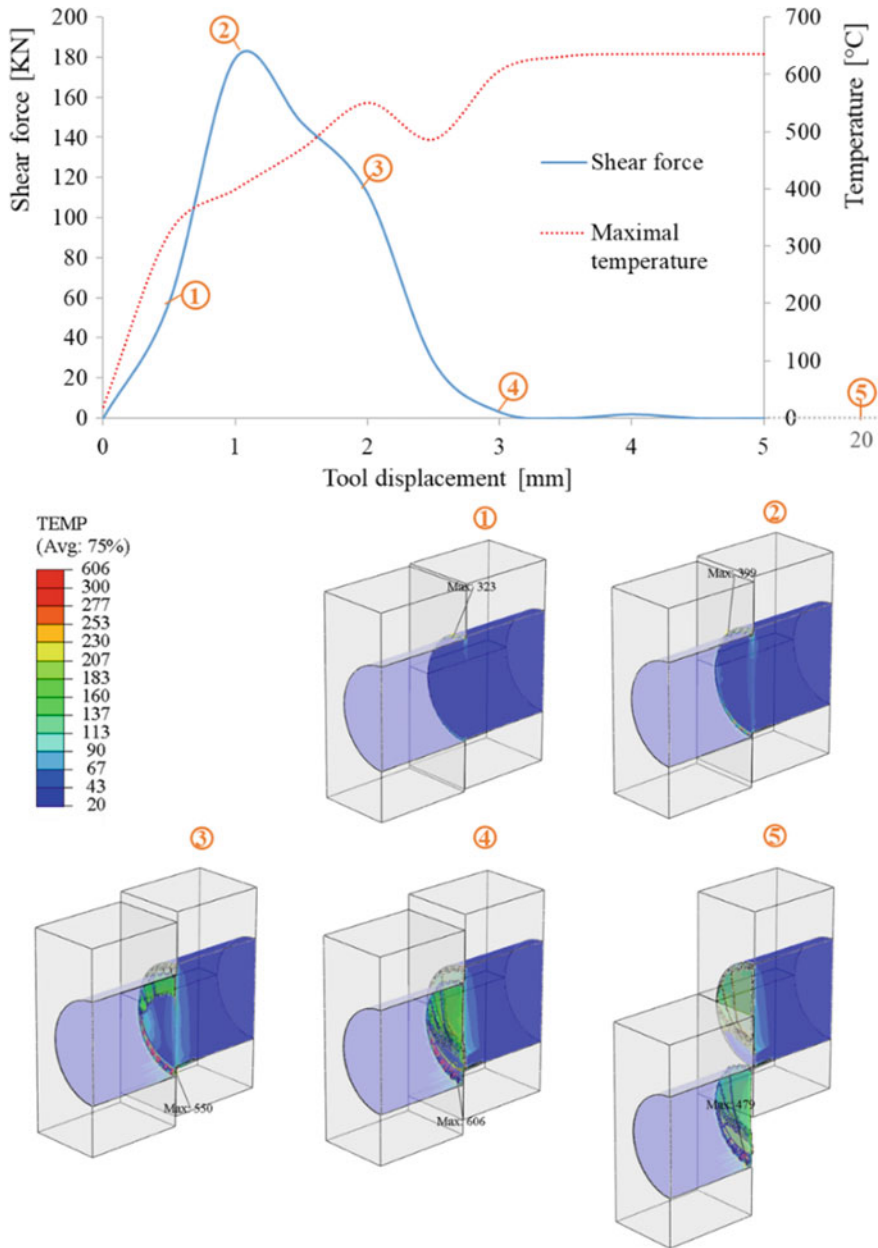
Fig. 2 Shearing force displacement-curve and temperature evolution

energy is dissipated into heat which induces material softening. This work may be considered as a baselines to conduct FEA and optimization of shearing as well as other metal working processes involving high plastic deformation and elevated temperature.

References

Abaqus Help (2013) Abaqus analysis user's guide (6.13). © Dassault Systèmes

Brar NS, Joshi VS, Harris BW (2009) Constitutive model constants for Al7075-T651 and Al7075-T6. AIP Conf Proc 1195:945–948. https://doi.org/10.1063/1.3295300

Breitling J, Chernauskas V, Taupin E, Altan T (1997) Precision shearing of billets—special equipment and process simulation. J Mater Process Technol 71:119–125. https://doi.org/10.1016/S0924-0136(97)00157-X

Dalloz A (2007) Etude de l'endommagement par la découpe des aciers dual phase pour application automobile. Thesis, Paris, ENMP

Gouge M, Michaleris P (2017) Thermo-mechanical modeling of additive manufacturing, 1st edn. Butterworth-Heinemann

Hu CL, Chen LQ, Zhao Z, Li JW, Li ZM (2018) Study on the pre-shearing cropping process of steel bars. Int J Adv Manuf Technol 97:783–793. https://doi.org/10.1007/s00170-018-1979-9

Leine RI, Aeberhard U, Glocker C (2009) Hamilton's principle as variational inequality for mechanical systems with impact. J Nonlinear Sci 19:633–664. https://doi.org/10.1007/s00332-009-9048-z

Lestriez P (2003) Modélisation numérique du couplage thermo-mécanique-endommagement en transformations finies. Application à la mise en forme. Thesis, Université de Troyes

Maiti SK (1982) A numerical study on the edge-profile during shearing of bars using the principles of linear elastic fracture mechanics. J Mech Des 104:661–665. https://doi.org/10.1115/1.3256402

Moakhar S, Hentati H, Barkallah M, Louati J, Haddar M, Bonk C, Behrens BA (2019a) Modeling of the ductile damage-application for bar shearing. Mater wiss Werkstofftech 50(11):1353–1363. https://doi.org/10.1002/mawe.201800128

Moakhar S, Hentati H, Barkallah M, Louati J, Haddar M (2019b) Evaluation of AW-6082 aluminium bar shearing simulation. Lecture Note in Mechanical Engineering. Springer. ISBN 978-3-030-24246-6. https://doi.org/10.1007/978-3-030-24247-3_17

Xiaoguang Y (2015) Introduction of FEA and Abaqus. https://intranet.birmingham.ac.uk/as/libraryservices/library/skills/digitaltechnologyskills/documents/public/abaqustutorial1.pdf

Parametric Study of a Minimal Model of Wind Turbine Drivetrain System

Ahmed Ghorbel, Oussama Graja, Amel Bouaziz, Moez Abdennadher, Lassâad Walha, and Mohamed Haddar

Abstract There are several types of renewable energy, produced from different sources. One of the most efficient renewable today is the wind energy. In the case of wind power, the kinetic energy of the wind drives a generator which produces electricity. The drive train is an important component in realizing reliable and robust wind turbines. This research work investigates the dynamic behavior of a horizontal axis wind turbine drivetrain under different excitation sources. The present paper developed an 11° of freedom (DOF) dynamic model of wind turbine geared transmission system. This model includes the main factors such as the time-varying mesh stiffness, bearing stiffness and damping. The aerodynamic driving is also defined taking into account the size of the blades and the average wind speed. Using the implicit Newmark's method, the dynamic response of the bearing and the transmission error of the wind turbine gearbox is presented with the time signal and Fast Fourier Transform (FFT) spectrum. The results show the different vibration levels of the bearings and the effect of the wind speed and the gear ratio on the dynamic behavior of the system. Finally, a time-frequency representation is used to have more information about our system dynamic behavior.

Keywords Wind turbine · Gearbox · Dynamic responses · Profile error

1 Introduction

A wind turbine is a device designed to transform the kinetic energy of the wind into mechanical energy. They are generally used to produce electricity and come under the category of renewable energies (Zhao and Ji 2016).

In this context, several studies have been developed to study the dynamic behaviour of wind turbines (Gabriele et al. 2008; Tounsi et al. 2016). Various dynamic models including the multi-body model and the lumped-parameter model (Zhao and Ji 2015) have been proposed for dynamic behavior study. Abboudi et al. (2011) have

A. Ghorbel (✉) · O. Graja · A. Bouaziz · M. Abdennadher · L. Walha · M. Haddar
Laboratory of Mechanics, Modeling and Production, National School of Engineering of Sfax, University of Sfax, Sfax, Tunisia
e-mail: gh.ahmed.enis@gmail.com

investigated the dynamic response of a two stage gear gearbox under an aerodynamic excitation. In 2011 Helsen et al. investigated the modal behaviour of a wind turbine gearbox using flexible multi-body modelling techniques. The main cause of many problems on the diagnosis of the wind energy is the gearbox faults. Vibration induced by geared system includes an important data about drivetrain condition (Ghorbel et al. 2017a). We can use dynamic modeling of gear vibration for increasing our information about the dynamic behavior of gearbox in the presence of some kind of gear defects (Divandari et al. 2012; Sharma and Anand 2016; Ghorbel et al. 2018). Zhu et al. (2014) developed a dynamic mass-lumped model of a wind turbine gearbox with flexible pins, and then investigated the dynamic behaviors of the wind turbine transmission system.

The main objective of this work is to investigate the dynamic responses of wind turbine drivetrain. The proposed dynamic model can be used to investigate the fundamental mechanism of wind turbine components including hub, generator, gearbox and bearings, which could give useful information to reduce the possibility of the gearbox check at an early stage. This chapter will study the effect of the wind turbine characteristics of the dynamic behavior of the system, and the dynamic response is investigated by a time signal, frequency spectrum and time-frequency representation.

2 Model of the Drivetrain Wind Turbine

The wind turbine is composed, mainly, by the hub, the transmission power system, the disc brake and the generator. The drivetrain model implemented in this work is developed with eleven degrees of freedom (11 DOF) and three main blocks as shown in Fig. 1.

Each block is supported by a flexible bearing characterized by two stiffness k_{xj} and k_{yj} according to the x and y directions, respectively. The connecting shafts admit a torsional stiffness parameter $k_{\theta j}$ according to the z direction. I_{11} is the inertia of the
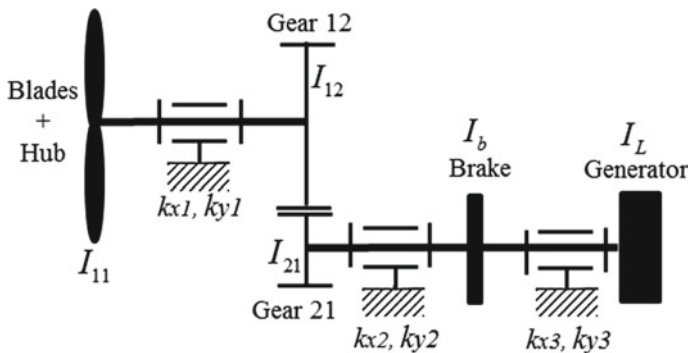

Fig. 1 Kinematic layout of the drivetrain wind turbine

blades and the hub. The brake disc and the generator inertias are defined by I_b and I_L. m_i ($i = 1, 2, 3$) represents the mass of block (i) supported by each bearings.

The linear displacements of the bearing are noted by x_j and y_j. The angular displacements of the wheel and gears following the directions Z are represented by θ_i.

In addition to the external excitation, the system is also submitted to internal excitation, which is the periodic fluctuation of mesh stiffness $k(t)$. The base radius of the gear is rb_{ji} and the inertia moments of gears are I_{ji} ($i, j = 1, 2$). The generalized coordinate's vector of the linear dynamic model can be defined by:

$$\{q\} = \left\{ x_1 \ y_1 \ x_2 \ y_2 \ x_3 \ y_3 \ \theta_{11} \ \theta_{12} \ \theta_{21} \ \theta_b \ \theta_L \right\} \tag{1}$$

2.1 Excitation Conditions

The input torque T_{in} is applied to gearbox as the input of the system. It can be defined by Eq. 1. ω_{blade} represents the blades rotational speed and P_{blades} represents the power produced by the blades. These two parameters are expressed by Eq. 2 (Zhao and Ji 2016):

$$T_{in} = P_{blade} / \omega_{blade} \text{ and } P_{blades} = \rho_{air} \pi r_{blade}^2 V_{wind}^3 C_p / 2 \tag{2}$$

where ρ_{air} represent the air density and r_{blade} expresses the blades radius. The average wind velocity is defined by V_{wind} and the performance coefficient is presented C_p. It is assumed that the loss of power in the gear system is negligible, the average output torque of the gearbox T_{out} can be expressed by using Eq. 3, where G_R is the gear ratio of the gearbox:

$$T_{out} = T_{in} / G_R \tag{3}$$

Assuming only external excitation is taken into account, the aerodynamic driving torque can be expressed by Eq. 4 as a periodic sinusoidal function, where T_{in} is the constant external driving torque, T_{f-in} represents the fluctuation of the driving torque, ω_e is the pulse of the external excitation ($\omega_e = 2\pi f_e$). When the main shaft is braked, the gears are not allowed to rotate:

$$T_{aero}(t) = T_{in} + T_{f-in} \cos(\omega_e t) \tag{4}$$

The braking torque C_{br} can be expressed as following (Ghorbel et al. 2017b):

$$C_{br} = \frac{4\mu N\varphi(R_1 + R_2)}{6 \cdot \sin(\varphi/2)} \left(1 - \frac{R_1 R_2}{(R_1 + R_2)^2} \right) \tag{5}$$

where μ represents the pad friction coefficient, N define the normal force and φ describe opening angle of the pad. R_1 and R_2 represent the brake pad outer and inner radii.

2.2 Equation of Motions

According to Lagrange's formalism, the kinematic differential equations governing the system motion are given by Eq. 6:

$$
\begin{cases}
I_{11}\ddot{\theta}_{11} + k_{\theta 1}(\theta_{11} - \theta_{12}) = T_{aero}(t) \\
I_{12}\ddot{\theta}_{12} - k_{\theta 1}(\theta_{11} - \theta_{12}) + k(t)rb_{12}\delta(t) = 0 \\
I_{21}\ddot{\theta}_{21} + k_{\theta 2}(\theta_{21} - \theta_b) + k(t)rb_{12}\delta(t) = 0 \\
I_b\ddot{\theta}_b - k_{\theta 2}(\theta_{21} - \theta_b) + k_{\theta 3}(\theta_b - \theta_L) = -C_{br} \\
I_L\ddot{\theta}_L - k_{\theta 3}(\theta_b - \theta_L) = -T_{out} \\
m_1\ddot{x}_1 + k_{x1}x_1 - k(t)\delta(t)\sin\alpha = 0 \\
m_1\ddot{y}_1 + k_{y1}y_1 + k(t)\delta(t)\cos\alpha = 0 \\
m_2\ddot{x}_2 + k_{x2}x_2 + k(t)\delta(t)\sin\alpha = -F_{tx} \\
m_2\ddot{y}_2 + k_{y2}y_2 - k(t)\delta(t)\cos\alpha = -F_{ty} \\
m_3\ddot{x}_3 + k_{x3}x_3 = -F_{tx} \\
m_3\ddot{y}_3 + k_{y3}y_3 = -F_{ty}
\end{cases}
\tag{6}
$$

where F_{tx} and F_{ty} are the tangential forces applied on the brake disc. The displacement $\delta(t)$ along the line of action is expressed by:

$$
\delta(t) = (x_1 - x_2)\sin\alpha + (y_1 - y_2)\cos\alpha + rb_{12}\theta_{12} + rb_{21}\theta_{21}
\tag{7}
$$

The variation of the teeth mesh stiffness of the single stage spur gear is assumed by a periodic square wave.

Table 1 Model parameters values

Parameters	Value
Bearing stiffness (N/m)	$k_{xj} = k_{yj} = 10^8$
Torsional shaft stiffness (N m/rad)	$K_{oj} = 10^5$
Teeth number	$Z_{12} = 72$, $Z_{21} = 18$
Average mesh stiffness (N/m)	$2 \cdot 10^8$

3 Numerical Results

The parameters values of the wind turbine system are summarized in Table 1. For the simulation, we consider that the rotor blades radius r_{blade} is 6 m, the performance coefficient C_p is 16/27 and the air density is equal to 1.21 kg/m^3. The effect of gear ratio and the rotation speed of the blades and hub is investigated in this section.

Figure 2 show the speed time response of the three bearings according to the direction x. It is found that the vibration of the first bearing is lower compared to the other two bearings. The time domain vibration signals are converted into frequency domain with the help of FFT (Fig. 3). The spectrum presents the gear mesh frequency, its harmonics and some Eigen frequencies.

The effect of rotational speed of the rotor blades are shown in Fig. 4. This figure represents the time dynamic response of the teeth deflection. It should be noticed that in the low speed, the vibrations are more important. The spectrum at 20 rpm of is shown in Fig. 5. The existence of several peaks in the signal is noticed. These
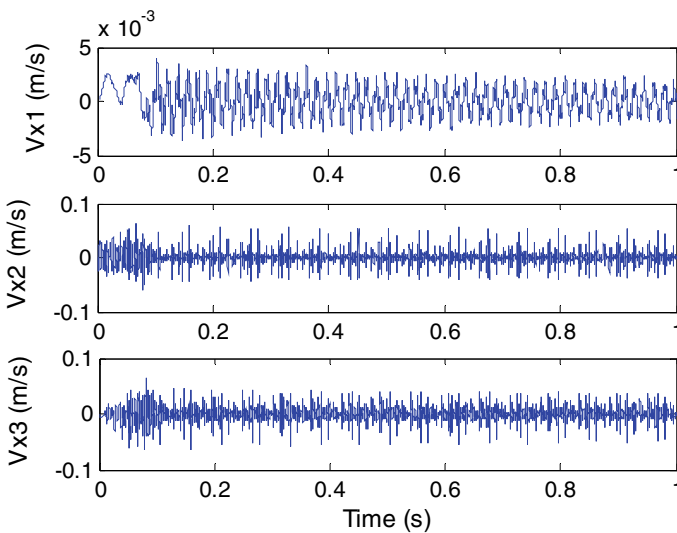
Fig. 2 Speed time response of the three bearings according to the direction x
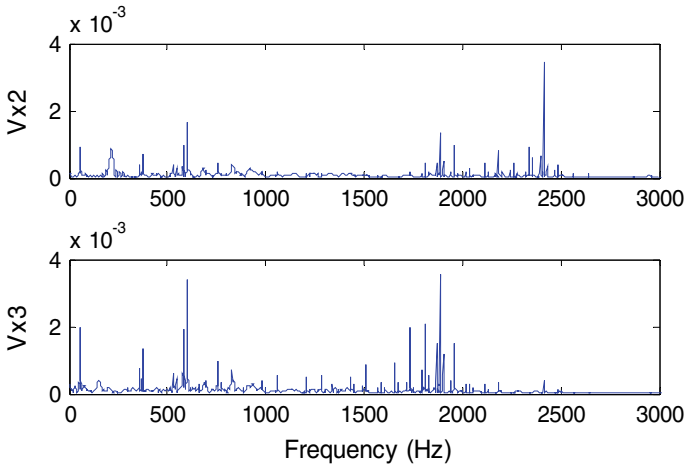
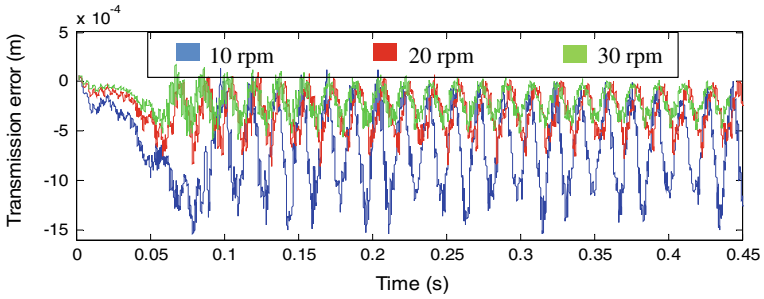**Fig. 3** Spectrum of the three bearings according to the direction *x*

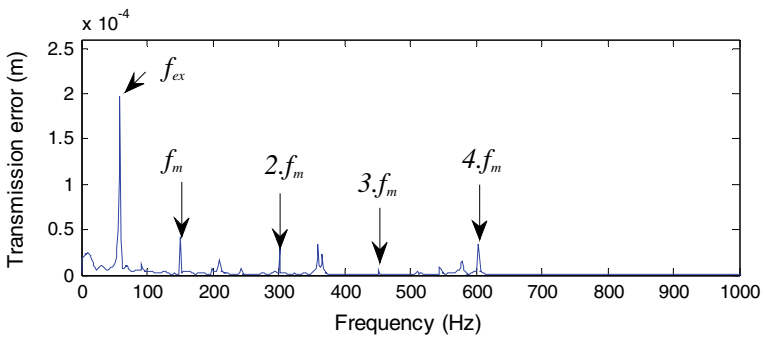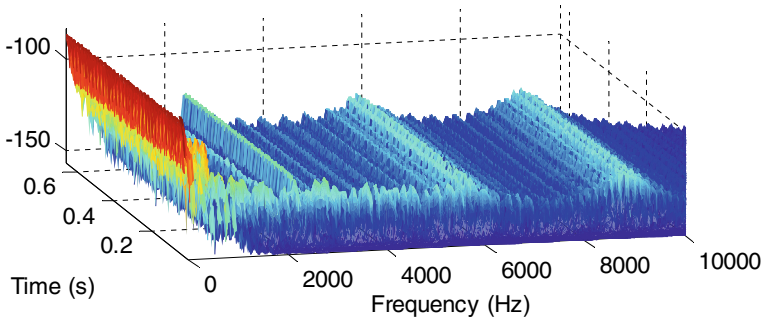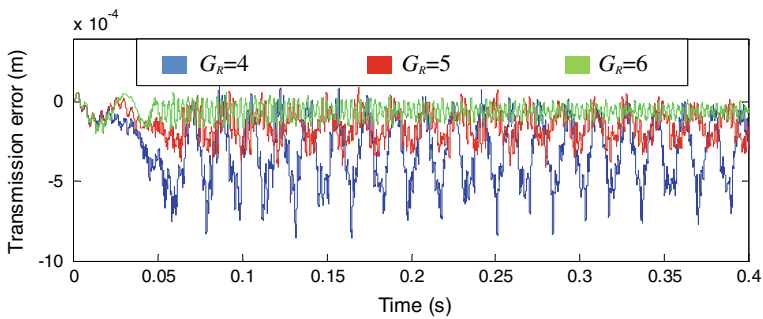**Fig. 4** Teeth deflection for different hub speeds

Fig. 5 Spectrum of the teeth deflection at 20 rpm

Fig. 6 Time-frequency response of the transmission error at 20 rpm

Fig. 7 Teeth deflection for different gear ratio

peaks correspond to the mesh frequency $f_e = 15,079$ Hz with their harmonics, the wind turbine torque frequency and the dominant Eigen frequencies.

Figure 6 shows the spectrogram obtained from the simulation. It presents the energy distribution of the transmission error signal as a function of time and frequencies. From the figure, we note that at lower frequency the system has the strongest power.

The effect of the gear ratio variation is shown in Fig. 7. It indicates that increasing the ratio will decrease the vibration amplitude of tooth deflection. So, it can be said that increasing speed in the gearbox can minimize the vibrations of the entire system.

4 Conclusion

In this paper, a rigid-flexible coupled dynamic model was developed based on the analysis of the transmission system of a wind turbine drive train. This model considered the time mesh stiffness variation of the geared system, the wind torque fluctuation, the three elastic supports, the hub, and the disc brake. The drivetrain system

was modelled by 11° of freedom. The dynamic responses of this dynamic model were made with the Newmark method. The vibration signals are analyzed by using the temporal responses, the frequency domain technique (Fast Fourier Transform) and by a time-frequency representation. A parametric study is achieved. It follows that the increase in the rotation speed of the hub and the increase of the gearbox ratio reduce the vibration amplitude of the transmission error.

References

Abboudi K, Walha L, Driss Y, Maatar M, Fakhfakh T, Haddar M (2011) Dynamic behavior of a two-stage gear train used in a fixed-speed wind turbine. Mech Mach Theory 46:1888–1900

Divandari M, Aghdam B, Barzamini R (2012) Tooth profile modification and its effect on spur gear pair vibration in presence of localized tooth defect. J Mech 28(2):373–381

Gabriele M, Hansen AD, Hartkopf T (2008) Variable speed wind turbines—modeling, control and impact on power systems. In: Proceedings of the European wind energy conference and exhibition, Brussels, pp 100–104

Ghorbel A, Abdennadher M, Walha L, Zghal B, Haddar M (2017) Modal analysis of the clutch single spur gear stage system with eccentricity defect. In: Signal processing applied to rotating machinery diagnostics, (SIGPROMD'2017), pp 87–95

Ghorbel A, Abdennadher M, Zghal B, Walha L, Haddar M (2017) Modal analysis and dynamic behavior for analytical drivetrain model. J Mech 1–17

Ghorbel A, Zghal B, Abdennadher M, Walha L, Haddar M (2018) Effect of the gear local damage and profile error of the gear on the drivetrain dynamic response. J Theoret Appl Mech 56

Helsen J, Vanhollebeke F, de coninck F, Vandepitte D, Desmet W (2011) Insights in wind turbine drive train dynamics gathered by validating advanced models on a newly developed 13.2 MW dynamically controlled test-rig. Mechatronics 21:737–752

Sharma V, Anand P (2016) A review of gear fault diagnosis using various condition indicators. Procedia Eng 144:253–263

Tounsi M, Beyaoui M, Abboudi K, Feki N, Walha L, Haddar M (2016) Influence of uncertainty in aerodynamic performance on the dynamic response of a two stage gear system. J Theoret Appl Mech 54(2):601–612

Zhao M, Ji JC (2015) Nonlinear torsional vibrations of wind turbine gearbox. Appl Math Model 39(16):4928–4950

Zhao M, Ji J (2016) Dynamic analysis of wind turbine gearbox components. Energies 9(2):110

Zhu C, Xu X, Liu H et al (2014) Research on dynamical characteristics of wind turbine gearboxes with flexible pins. Renew Energy 68(7):724–732

Unbalance Response of Composite Rotor Based on Equivalent Single Layer Theory

Safa Ben Arab, Slim Bouaziz, and Mohamed Haddar

Abstract The excitation due to the inevitable mass unbalance is the main reason of rotor vibrations. Therefore, this paper studies the rotating shaft dynamic behaviour and the mass unbalance theoretical formulation. Equivalent Single Layer Theory available in the literature is used to model the rotating composite shaft and the rotating hybrid shaft. This finite element formulation is adopted to analyse the effects of fiber orientations and stacking sequences while considering shear-normal coupling effects. Results obtained form this work are in good agreement with those available in the literature in terms of natural frequency, critical speed and receptance response amplitude and prove that the adopted shaft finite element reveals adequate for the dynamic analysis of rotating composite shafts with both symmetric and non-symmetrical stacking sequences. Moreover, obtained results revealed that fiber orientations and stacking sequences have a great influence on the dynamic characteristics of rotating composite shafts. This analysis focuses also on the natural frequencies and the unbalance response of isotropic, composite and hybrid shafts. Obtained results show that the receptance response amplitude of the different configurations decreases when the frequency increases. Furthermore, the receptance response amplitude of different hybrid configurations depends on the rotor performing frequency.

Keywords Dynamic analysis · Unbalance response · Rotating shaft · Composite material · Hybrid configuration

S. Ben Arab (✉) · S. Bouaziz · M. Haddar
Mechanics, Modelling and Production Laboratory (LA2MP), Mechanic Department,
National School of Engineers of Sfax, University of Sfax, B.P. 1173, 3038 Sfax, Tunisia
e-mail: safabenarab@gmail.com

S. Bouaziz
e-mail: slim.bouaziz1@gmail.com

M. Haddar
e-mail: mohamed.haddar@enis.rnu.tn

1 Introduction

Misalignment is one of the most commonly observed faults in rotors. Nevertheless, there have been limited research to comprehend its effect on rotor dynamic behaviour. Patel and Darpe (2009a, b) focused on understanding misaligned rotor dynamics and reducing the uncertainty to ameliorate the reliability of the diagnosis of the misalignment fault. They examined the misalignment effects and its type on flexible coupling forcing characteristics. In fact, (Patel and Darpe 2009a) used Timoshenko beam elements with six dof to model the coupled rotor system. They proposed an experimental approach in order to determine the magnitude and the harmonic nature of the misalignment excitation. The misalignment coupling stiffness matrix, derived from experimental data and applied misalignment between the two rotors is used to found the force vector. For sub-critical speeds, authors studied the steady-state vibration response. In addition, lateral, axial and torsional vibrations are also examined. Patel and Darpe (2009b) experimentally investigated the vibration response of misaligned coupled rotors supported on rolling bearings. Moreover, authors studied the steady-state vibration response at integer fraction of the first bending natural frequency. Besides, authors proposed new misalignment diagnostics recommendations and the effectiveness of the full spectra and orbit diagrams to reveal the unique nature of misalignment fault. In fact, the spectra is an important tool to separate defects that generate similar frequency spectra and allow for a more reliable misalignment diagnosis. Bouaziz et al. (2011) investigated numerically the dynamic response of a misaligned rotor mounted in two identical active magnetic bearings (AMBs). Authors presented three simplified models of current biased radial active magnetic bearings: the magnetic forces acting on the rotor, the coil currents and the rotor displacement are obtained using an electromagnetic theory. Furthermore, authors modeled the AMBs' dynamic support parameters by linearised direct cross axes stiffness and damping coefficients. They presented also a misaligned rotor spatial model with two dofs. In order to study the dynamic behavior of spatial misaligned rotor mounted in AMBs, simulation results are performed. The angular misalignment is such that the 2B and 4B running speed components are important. In fact, their magnitudes vary according to the magnet number in the bearing and to the air gap between the stator and the shaft. In order to identify the unbalance in a single disk rotor bearing system, (Yao et al. 2018) proposed a method that combines modal expansion and optimization algorithms. Simulation and experimental results demonstrate the effectiveness of the proposed identification method, which permits to detect the location of the unbalance and to define its parameters. While, in order to identify the unbalance parameters in a double disk rotor bearing system, authors proposed a method that involves an integrated modal expansion/inverse problem approach combined with optimization. This method overcomes the limitation of the inverse problem applications which rely upon the prior knowledge of the unbalance axial location. Furthermore, the comparison between both methods shows that obtained results using the latter methodology are more accurate in the case of a double disk rotor bearing system. The dynamic balance experiments also demonstrate the validity of the proposed methods, which
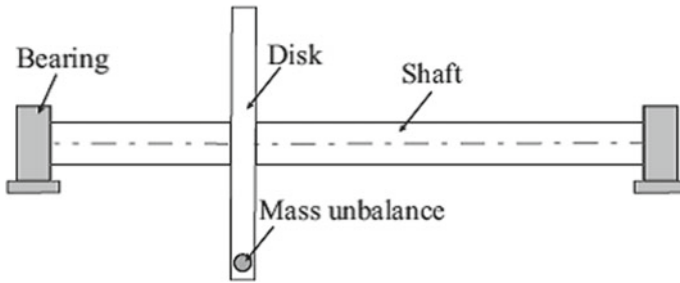
Fig. 1 Rotor system elements

could provide effective help to the rotordynamics designer. Shrivastava and Mohanty (2019) proposed an unbalance identification technique based on a joint input-state estimation algorithm. The technique has been verified by numerical simulations and experimental measurements. Incorporating measurement errors in the numerical study prove the robustness of the proposed technique. Authors presented results for different shaft speeds and measurement noise levels and experimental results for different unbalance configurations. Furthermore, they performed a sensitivity analysis in order to analyse the effect of system parameters. Obtained results show that the estimated amount of unbalance is close to the actual value. However, for some cases, some deviations are observed in the estimated phase angles.

The present work focuses on the analysis of the shaft dynamic behaviour and the theoretical approach for the characterization of mass unbalance in the rotor system elements for composite shafts and hybrid shafts by using the Equivalent Single Layer Theory (ESLT) available in the literature developed by Arab et al. (2017). Results obtained by Arab et al. (2017) proved the effectiveness of ESLT to analyse the dynamic behavior of rotating composite shafts while considering the effects of fiber orientation, stacking sequence and shear-normal coupling. The geometry of the rotor system adopted in this work is shown in Fig. 1. The mass unbalance denoted by m_u is located at a distance d from the geometric center of the rotating shaft.

2 Mass Unbalance

The unbalance appears due to several causes such as: material inhomogeneity, thermal deformation and manufacturing error, Fig. 2.

In this work, the unbalance is defined by a mass m_u positioned at a distance d from the geometric center C of the shaft as shown in Fig. 3.

Accordingly to Fig. 3, the mass unbalance remains in a plane perpendicular to x axis and the coordinate along this axis is constant. The mass unbalance coordinates in the reference frame R_0 are defined as:
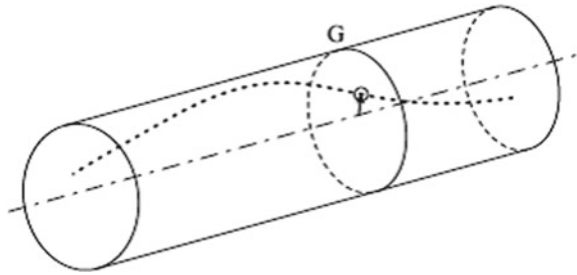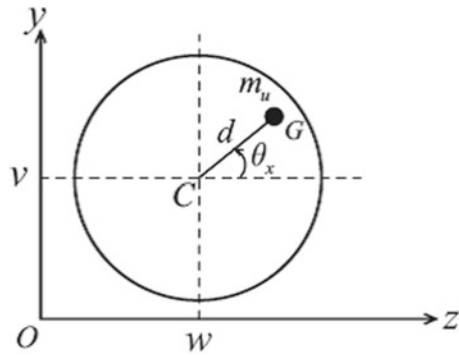
Fig. 2 Unbalance in a rotor

Fig. 3 Position of the mass unbalance

$$OG_{/R_0} = OC + CG = \left\{ \begin{array}{l} u(x, t) + x_c \\ v(x, t) + d \sin \theta_x \\ w(x, t) + d \cos \theta_x \end{array} \right\} \tag{1}$$

Hence, the mass unbalance velocity is expressed as:

$$V_{G/R_0} = \frac{dOG}{dt} = \left\{ \begin{array}{l} \dot{u} \\ \dot{v} + d\dot{\theta}_x \cos \theta_x \\ \dot{w} - d\dot{\theta}_x \sin \theta_x \end{array} \right\} \tag{2}$$

The angular velocity θ_x is assumed constant where $\theta_x = \Omega t$. So, $\dot{\theta}_x = \Omega$. As a result, the mass unbalance velocity can be rewritten as follows:

$$V_{G/R_0} = \left\{ \begin{array}{l} \dot{u} \\ \dot{v} + d\Omega \cos(\Omega t) \\ \dot{w} - d\Omega \sin(\Omega t) \end{array} \right\} \tag{3}$$

The kinetic energy T_u of the mass unbalance is determined as:

$$T_u = \frac{1}{2} m_u \left\| V_{G/R_0} \right\|^2$$

$$= \frac{1}{2} m_u \big(\dot{u}^2 + \dot{v}^2 + \dot{w}^2 + d^2 \Omega^2 + 2 d \Omega \cos(\Omega t) \dot{v} - 2 d \Omega \sin(\Omega t) \dot{w} \big) \quad (4)$$

On one hand, the mass unbalance is much smaller than the rotor mass. So, the first, second and third terms of Eq. (4) can be neglected. On the other hand, the fourth term is constant and has no influence on the equation. For that resons, the mass unbalance kinetic energy equation can be expressed:

$$T_u = m_u d \Omega (\cos(\Omega t) \dot{v} - \sin(\Omega t) \dot{w}) \quad (5)$$

The application of Lagrange's equation to the mass unbalance kinetic energy Eq. (5) gives:

$$\begin{cases} \frac{d}{dt} \left(\frac{\partial T_u}{\partial \dot{v}} \right) - \frac{\partial T_u}{\partial v} = -m_u d \Omega^2 \sin(\Omega t) \\ \frac{d}{dt} \left(\frac{\partial T_u}{\partial \dot{w}} \right) - \frac{\partial T_u}{\partial w} = -m_u d \Omega^2 \cos(\Omega t) \end{cases} \quad (6)$$

Consequently, the resulting force of the mass unbalance is given as follows:

$$\{Q(t)\} = \begin{Bmatrix} -m_u d \Omega^2 \sin(\Omega t) \\ -m_u d \Omega^2 \cos(\Omega t) \end{Bmatrix} \quad (7)$$

which can be rewritten as:

$$\{Q(t)\} = \mathbb{R} \left(\Omega^2 \begin{Bmatrix} j m_u d \\ -m_u d \end{Bmatrix} e^{j\Omega t} \right)$$
$$= \mathbb{R} \big(\Omega^2 \{b_0\} e^{j\Omega t} \big) \quad (8)$$

where $\mathbb{R}$ and $\Omega^2 \{b_0\}$ represent respectively, the real solution part and the force vector which is acting because of the mass unbalance where $\{b_0\}$ is a complex vector.

3 Composite Shaft

Arab et al. (2017) proposed ESLT to analyse the dynamic behaviour of rotating composite shafts. In this approach, a rotating shaft finite element model based on Timoshenko theory is adopted. This formulation is used to model composite material shafts by defining equivalent shaft section properties. In addition, the developed ESLT consists on considering an equivalent single layer with equivalent mechanical properties of all the orthotropic layers of the composite shaft. Moreover, this theory is developed to avoid the main limitations of formulations which do not consider the shear-normal coupling effects.

Considering an arbitrary layer of the laminate with fiber orientated at angle α with respect to the x axis of the cylindrical coordinate system (x, r, ϕ) as shown in Fig. 4.
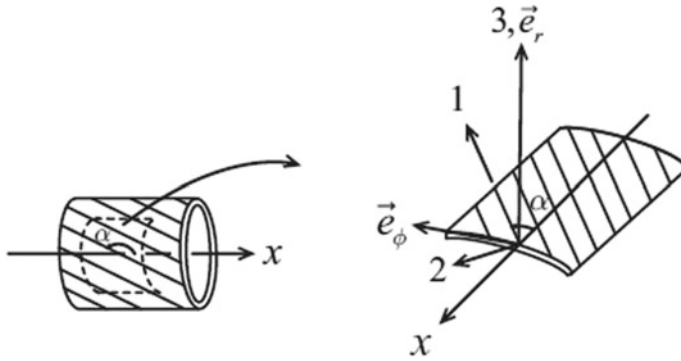
Fig. 4 Principal material coordinates axes on arbitrary orthotropic layer

The stress-strain relation expressed in this chosen cylindrical coordinate system is defined as (Arab et al. 2017):

$$\{\sigma\} = [\bar{Q}]\{\varepsilon\} \tag{9}$$

where $\{\sigma\}$, $\{\varepsilon\}$ and $[\bar{Q}]$ are respectively the stress filed, strain field and the transformed material stiffness matrix of the layer (Reddy 1997).

4 Results and Discussion

4.1 Validation Case Study

Let consider the rotor system proposed by Lalanne and Ferraris (1990), which is a steel shaft with three rigid steel discs supported by two bearing as shown in Fig. 5.

The adopted rotor system has the following properties:

- Two identical bearings defined as: $K_{yy} = 7 \times 10^7$ N/m, $K_{zz} = 5 \times 10^7$ N/m, $K_{yz} = K_{zy} = 0$ and $C_{yy} = 7 \times 10^2$ N/m, $C_{zz} = 5 \times 10^2$ N/m, $C_{yz} = C_{zy} = 0$.
- Mass unbalance of 200g mm is situated on the disk D_2.
- The steel discs geometric data are given in Table 1.
- The steel shaft geometric and material properties are given as follows:

    - $L_1 = 0.2$ m, $L_2 = 0.3$ m, $L_3 = 0.5$ m, $L_4 = 0.3$ m, radius $= R = 0.05$ m;
    - Steel: $E = 2 \times 10^{11}$ Pa, $\nu = 0.3$, $\rho = 7800$ kg/m^3;
    - The shaft uses 13 finite elements of equal length.

Table 2 gives the critical speeds, amplitude of the response at node 6 and accuracy percentage of the amplitude obtained from this work in case of mass unbalance.
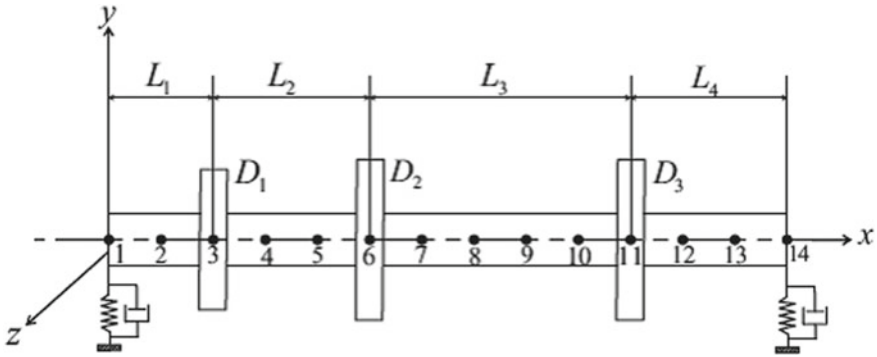
Fig. 5 Rotor system

Table 1 Discs geometric data (m)

Disk	Inner radius	Outer radius	Thickness
D_1	0.05	0.12	0.05
D_2	0.05	0.2	0.05
D_3	0.05	0.2	0.06

Table 2 Critical speed (rpm), amplitude of the response (m) and accuracy percentage of the amplitude

Peak	Lalanne and Ferraris 1990, p. 74	Present work
1st	3620.5 0.938×10^{-3}	3621 0.9856×10^{-3} 4.8%
2nd	3798.3 0.210×10^{-2}	3798 0.2116×10^{-2} 0.7%
3rd	10,018 0.499×10^{-4}	10,020 0.5331×10^{-4} 6.4%
4th	11,281 0.130×10^{-3}	11,280 0.1428×10^{-3} 9%
5th	16,787 0.421×10^{-5}	16,860 0.4361×10^{-5} 3.5%
6th	24,418 0.684×10^{-4}	24,410 0.8009×10^{-4} 14.6%
7th	26,611 0.311×10^{-4}	26,570 0.3524×10^{-4} 11.7%
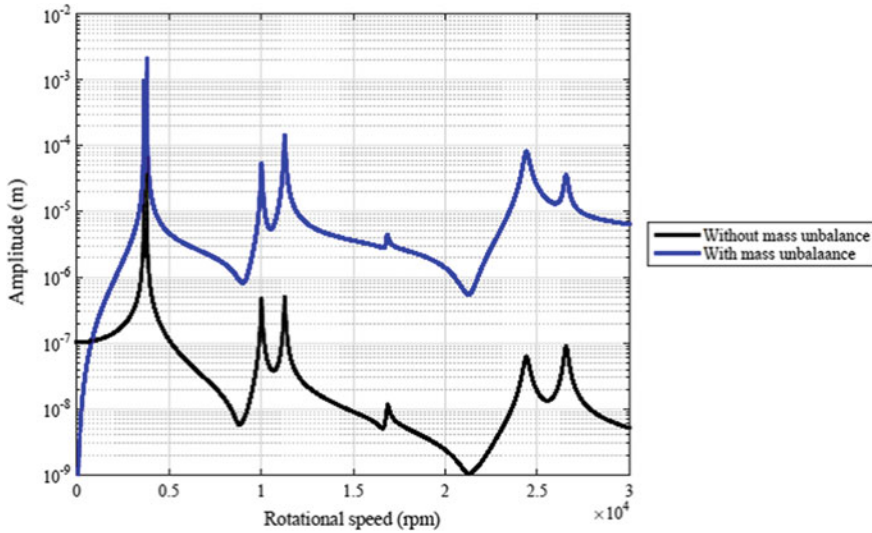
Fig. 6 Mass unbalance response

Obtained results in terms of critical speeds and amplitude of the receptance at node 6 are compared with those obtained by (Lalanne and Ferraris 1990) as shown in Table 2. In fact, critical speeds obtained from this work are satisfactory when comparing with those obtained by Lalanne and Ferraris (1990). A variation between 0.7 and 9% is obtained when comparing the amplitude of the receptance from the 1st peak to the 5th peak, while variation between 11.7 and 14.6% is obtained when comparing the 6th peak to the 7th peak.

The displacement at the node 6 for both cases without and with mass unbalance are shown in Fig. 6. It can be observed that the displacement amplitude increases in case of mass unbalance.

4.2 Effects of Fiber Orientation and Stacking Sequence

Considering a simply supported composite shaft which presents the following geometric and material properties:

- Carbon/epoxy shaft: $L = 1.2$ m, outer radius $= R_O = 0.048$ m, wall thickness $= h = 0.008$ m, $E_1 = 172.7$ GPa, $E_2 = 7.2$ GPa, $G_{ij} = 3.76$ GPa, $v_{12} = 0.3$, $\rho = 1446.2$ kg/m^3.
- Shear correction factor: $k_s = {}^1/_2$.

In this study, the stacking sequence consists of four layers: two layers with fibers oriented at 90° and two layers with fibers oriented at 0°. Table 3 gives the variation of the bending natural frequencies for different stacking sequences.

Table 3 Variation of the bending frequencies (Hz) with stacking sequence

Configurations	1st bending	2nd bending	3rd bending
[90, 90, 0, 0]	245	734	1261
[0, 0, 90, 90]	222	695	1221
[0, 90, 90, 0]	235	717	1244
[90, 0, 0, 90]	234	715	1242
[0, 90, 0, 90]	229	706	1233
[90, 0, 90, 0]	240	726	1253

Figure 7 presents the Campbell diagram of the first pairs of the bending mode of the rotating shaft for different stacking sequence. It can be noted that the natural bending frequencies of the rotating composite shaft are very similar and have a slight dependance on fiber orientations for symmetric stacking sequences. It can be observed also that the highest bending natural frequencies correspond to the stacking sequence where maximum layer number with fibers oriented at 0° occupy the outer radius. While, the lowest bending natural frequencies correspond to the stacking sequence where maximum layer number with fibers oriented at 0° occupy the inner radius as proved by Arab et al. (2017).
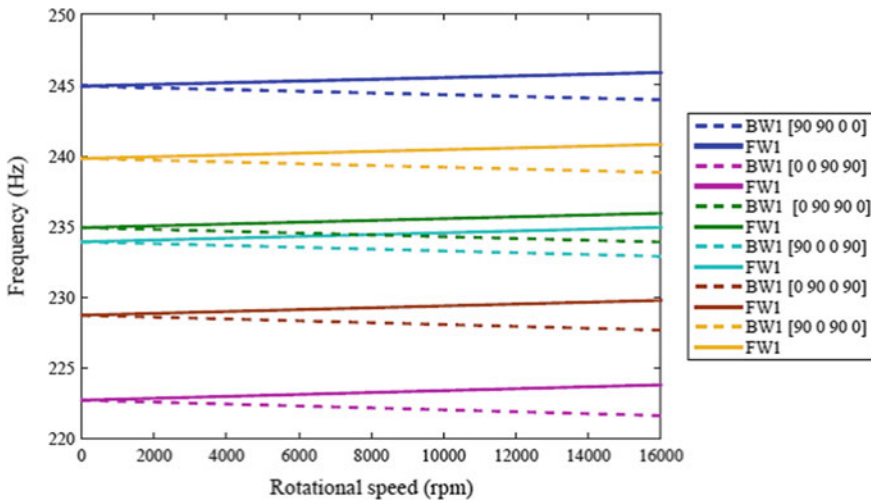
Fig. 7 First pairs of the bending mode for different stacking sequence

4.3 Different Shaft Configurations

In the above example, an isotropic configuration is assumed. However, in the present example a hybrid configuration is taken into account. Let consider a simply supported shaft with one rigid steel disk at $L/3$ position as shown in Fig. 8.

The rotor system has the following properties:

- The length of the shaft is $L = 1.3$ m and the outer diameter is $D_o = 50$ mm.
- A mass unbalance of 10^{-4} Kg located at 0.15 m from the center of the disk.
- Four different shaft configurations are studied:

  - Two isotropic configurations: aluminium shaft and composite shaft.
  - Two hybrid configurations [inner material, outer material] shaft such as: [aluminium, composite] and [composite, aluminium] shafts.

The composite shaft is made of carbon/epoxy whose material properties are defined in Table 4. The stacking sequence adopted in this example is [0, 90, 90, 0].

The aluminium material properties are defined as: $E = 66 \times 10^9$ Pa, $\nu = 0.33$ and $\rho = 2680$ kg/m^3. The unbalance response of point receptance type for the different configurations is shown in Fig. 9. In fact, the response is examined on the associated node.

Figure 9 shows that for low frequencies below 200 Hz, natural frequencies of both configurations [Al, Comp] and [Comp, Al] are higher than those of aluminium and composite configurations. While, for frequencies higher than 200 Hz, natural frequencies of both hybrid configurations are between that of composite configuration and aluminium configuration. It can be observed that both hybrid configurations have a slight difference in the natural frequencies. Moreover, it can be noted that the receptance amplitude of the different configurations decreases when the frequency increases. Furthermore, the receptance amplitude of [Al, Comp] and [Comp, Al] depends on the rotor frequency performing.

Fig. 8 Rotor system
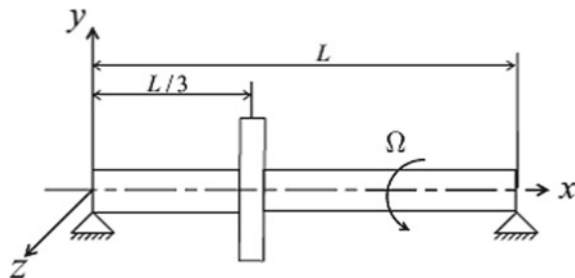
Table 4 Carbon/epoxy shaft material properties

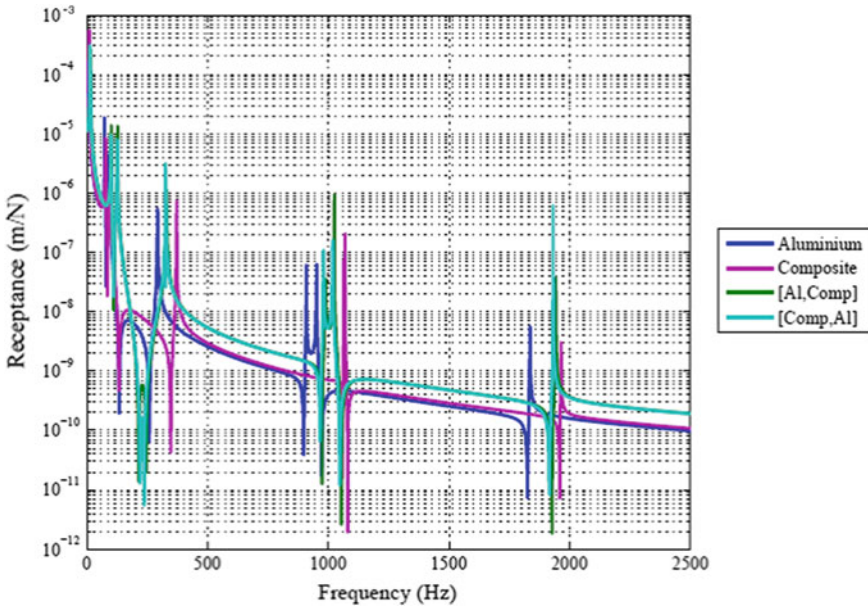| Material	E_1 (GPa)	E_2 (GPa)	G_{ij} (GPa)	ν_{12}	ρ (kg/m^3)
Carbon/epoxy	130	10	7	0.25	1500

Fig. 9 Unbalance response for different configurations

5 Conclusion

A theoretical formulation of the mass unbalance in a rotating shaft was developed in this work. Obtained results prove the good agreement with those available in the literature in terms of critical speed and response amplitude. Natural frequencies and unbalance response of isotropic, composite and hybrid shafts was also analysed in this work. Obtained results show that frequency increases as the receptance amplitude of the different configurations decreases. They show also that the receptance amplitude of different hybrid configurations depends on the rotor frequency performing.

References

Arab SB, Rodrigues JD, Bouaziz S, Haddar M (2017) A finite element based on equivalent single layer theory for rotating composite shafts dynamic analysis. Compos Struct 178:135–144

Bouaziz S, Messaoud N, Maatar M, Fakhfakh T, Haddar M (2011) A theoretical model for analyzing the dynamic behavior of a misaligned rotor with active magnetic bearings. Mechatronics 21:899–907

Lalanne M, Ferraris G (1990) Rotordynamics prediction in engineering. Wiley, Hoboken, NJ

Patel T, Darpe A (2009a) Vibration response of misaligned rotors. J Sound Vib 325:609–628

Patel T, Darpe A (2009b) Experimental investigation on vibration response of misaligned rotors. Mech Syst Signal Process 23:2236–2252

Reddy J (1997) Mechanics of laminated composite plates—theory and analysis. CRC Press, Boca Raton

Shrivastava AS, Mohanty AR (2019) Identification of unbalance in a rotor system using a joint input-state estimation technique. J Sound Vib. https://doi.org/10.1016/j.jsv.2018.11.019

Yao J, Liu L, Yang F, Scarpa F, Gao J (2018) Identification and optimization of unbalance parameters in rotor-bearing systems. J Sound Vib 431:54–69

The Effect of Perturbation on the FRF Based Substructuring

Marwa Bouslema, Taher Fakhfakh, Rachid Nasri, and Mohamed Haddar

Abstract The substructuring method premised on the receptance functions of the subsystems is studied in order to determine the global dynamics behavior of a coupled transmission system. This approach is applied on a double reducer stage. The formulation of the lumped-parameter model and the resolution of the eigenvalue problem are determined. Measurements of FRFs produce noise, which can affect the efficiency of the studied system. In fact, the effect of perturbation due to the noise of measurement in the FRFs of subsystems (which can represent a fault in gears systems) is illustrated on the model studied. Two types of noise are artificially introduced to the exact FRFs, which are the pole shifting, and the perturbed FRFs. The theoretically FRFs are simulated by applying the method of modes superposition. The disturbed FRFs for the subsystems are generated and the results of these FRFs are compared to exact FRFs. The effect of perturbed FRF and the pole shifting on the FRF substructuring method were discussed. Simulation demonstrate that the noise on FRFs of reducer stage can be influence by the neighbor FRFs system. The perturbation in subsystem FRFs can be propagated due to the process of coupling and they affect especially the coupling frequency.

Keywords Substructuring method · Perturbed FRF · Pole shifting

M. Bouslema (✉) · T. Fakhfakh · M. Haddar
Mechanical Modeling and Manufacturing Laboratory (LA2MP), National School of Engineers of Sfax, University of Sfax, B.P. 1173, 3038 Sfax, Tunisia
e-mail: marwa.bouslema@yahoo.fr

T. Fakhfakh
e-mail: tahar.fakhfakh@enis.rnu.tn

M. Haddar
e-mail: mohamed.haddar@enis.rnu.tn

R. Nasri
Applied Mechanics and Engineering, University of El-Manar II, 1002 Tunis, Tunisia
e-mail: rachid.nasri@enit.rnu.tn

1 Introduction

The Dynamic Substructuring (DS) methods have been used in order to reduce both the complexity of dynamical models and the size of computational models. This method is used to study the vibration modes of such a coupled system. The Frequency Based on Sub-structuring method (FBS) is the most used DS method. Several research were proposed the experimental FBS approaches due to their various advantages.

Despite several successes reported in the literature concerning the method of sub-structuring, one of the major difficulties is encountered in the perturbation of FRFs. For this reason, several investigations have been focused to the influence of FRF errors on the response of system. Providing an exact FRF is difficult because FRFs are often contaminated by random measurement noise. The control noises should be considering in numerical simulations of robust algorithms. For more realistic simulated measurements. D'Ambrogio and Fregolent (2010) added random noise with a Gaussian distribution to corresponding responses obtained by decoupling in the studied system FRFs. D'Ambrogio found that perturbation in the identifying FRFs appears new peaks in the spectra response. An important issue has attracted the attention of many researchers is how disturbances in the mechanical structure are propagated in the process of the assembly of substructuring dynamic (Urgueira 1989; Wenjie 2000; Xiuchang et al. 2013).

So, researches are interested to examine the influence of the perturbation on the coupled system FRFs. Xiuchang et al. (2013) used the substructuring method to investigate the transmission of vibrations and the propagation of uncertainty in a floating study system with considering elastic coupling. Furthermore, he studied the effects of various errors frequently encountered in FRFs of subsystems, such as the pole shifting, the perturbation in the modes and the perturbation in the FRFs on the results FRFs. The perturbed FRF was investigated by modifying the pole of the raft system to analyze these influences on the response of the coupled system. Much effort was devoted to develop well-conditioned FBS methods, such as the coupling method proposed by Jetmundsen et al. (1988).

The main objective of this paper is to propose a substructuring approach to analyze the vibration modes in multi-stage gears. In fact, the analysis of the global system is more difficult than that of the local dynamic behavior. If a subsystem is replaced by another whose FRF is known, this method becomes useful and allows a rapid computation of the global system FRF. In addition, the sub-structuring method can be useful in some applications of damage detection in gear systems, which can be considered as kind of system perturbation. A parametric study is make to determine the sensitivity of the substructuring method to measurement noise.

The present manuscript is organized as following structure. Section two described the analytical main of FBS. Section three gives the description of the studied system and the effects of various perturbation on the response of subsystem obtained by substructuring method.

2   Theory of Substructuring Method

The substructuring method aims the determination of the dynamic behavior of a rigidly coupled system based on the FRF of the uncoupled subsystem. An assembly procedure is applied to determine the FRFs of global system by combining the FRF of each sub-system.

2.1   Frequency Response Functions (FRF)

Bishop and Johnson (1960) described the FRF coupling method. The frequency based substructuring method (FBS) consists to determine the FRF of damped subsystem by executing an FRF synthesis based on a natural frequencies and a mode shape. According to the method of modes superposition, exact FRFs are expressed by:

$$H_{pq}(\omega) = \sum_{r=1}^{n} \frac{_r\Phi_{pr}\Phi_q}{\omega_r^2 - \omega^2 + j2\xi_r\omega_r\omega} \tag{1}$$

where $H_{pq}(\omega)$ is the steady state displacement at coordinate p due to a harmonic force excitation at coordinate q, n denotes the Degrees of Freedom number (DoFs). The mass-normalized eigen-vector is defined by $_r\Phi_p$. ω_r and ξ_r represent the natural frequency and the damping ratio for mode r respectively.

2.2   Coupling Method

Liu and Ewins (2002) determined mathematically the formulation of coupling method. The receptance matrices of subsystems 'A' and 'B' are presented as in Jetmundsen et al. (1988). A general formulation of a coupled dynamic system consisting of two sub-systems 'A' and 'B' coupled by a set of rigid connector is developed according to Jetmundsen et al. (1988):

$$\begin{bmatrix} H_{aa} & H_{ac} & H_{ab} \\ H_{ca} & H_{cc} & H_{cb} \\ H_{ab} & H_{bc} & H_{bb} \end{bmatrix} = \begin{bmatrix} _AH_{ii} & _AH_{ic} & 0 \\ _AH_{ci} & _AH_{cc} & 0 \\ 0 & 0 & _BH_{jj} \end{bmatrix} - \begin{bmatrix} _AH_{ic} \\ _AH_{cc} \\ _BH_{ic} \end{bmatrix} [[_AH_{cc}] + [_BH_{cc}]]^{-1} \begin{bmatrix} _AH_{ic} \\ _AH_{cc} \\ _BH_{ic} \end{bmatrix}^T \tag{2}$$

where $[_AH]$ and $[_BH]$ represents the receptance matrices of subsystems 'A' and 'B', respectively. The internal DoFs are denoted by subscript i and j and the coupling DoFs are represented by c. The receptance matrices of the entire system where developed by Liu and Ewins (2002). The whole coupling FRFs system are calculated using Eq. (2).

3   Numerical Simulations

3.1   *Description of the Studied System*

The analytical model, studied in this chapter, is a two stages spur gear system as shown in Fig. 1. The reducer stage is composed of two subsystems. A rigid coupling connects both subsystems A and B. The wheels (1, 1) and (3, 2) characterize the motor side and the receiver side, respectively. Im and Ir present the inertia of motor and receiver, respectively. Shaft (2) is connected to shaft (3) by a rigid coupling having Ia inertia. Bearing supporting shafts are modeled by two linear spring and damping. Gears are assumed as concentrated masses.

Table 1 present the mechanical parameters of the studied mechanism.

The response of the entire system is compared by the coupled response using the substructuring method.

Practically, and whatever the precision provided during FRF measurements, it is difficult to develop FRFs that do not exhibit perturbation. Measurements of FRFs produces noise, which can affect the efficiency of the studied system. Two types of noise are artificially introduced to the exact data of the system using the modal
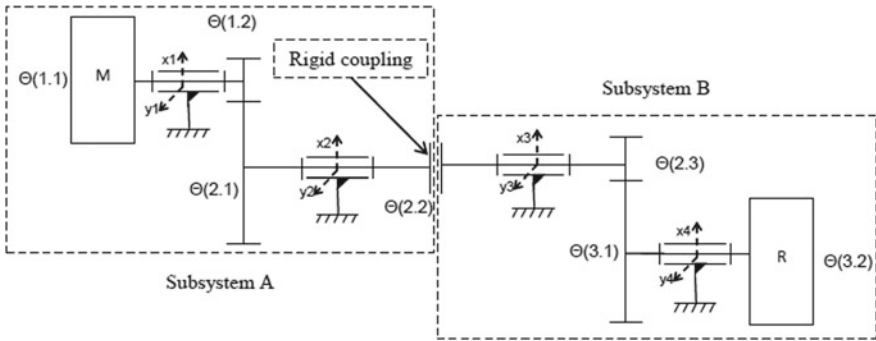

Fig. 1   A double spur gear stage with rigid coupling

Table 1   Parameters of the studied two-stage gear system

Parameters	Value
Torsional damping	$C_{\theta i} = 5.5 \bullet 10^{-2}$ (Nm s/rad)
Torsional shaft flexibilities	$K_{\theta i} = 10^5$ (Nm/rad)
Bearings stiffness (N/m)	$k_{xi} = k_{yi} = 10^8$
Bearings damping (Ns/m)	$c_{xi} = c_{yi} = 0.5$
Pressure angle	$\alpha_1 = \alpha_2 = 20°$
Teeth module	$m = 4 \bullet 10^{-3}$ (m)
Inertia coupling	$4.48 \bullet 10^{-8}$

data. The perturbation in the FRFs of the subsystems are generated and the results of these FRFs are compared to those of the exact FRFs. Using the method of modes superposition, we obtained the exact FRFs.

3.2 Effect of Pole Shifting on Subsystem Response

A fault can be modeled by a decrease or an increase in the average meshing stiffness (due respectively to a gear tooth crack or to a tooth local hardening). The presence of fault can be represented by the decreasing or increasing in the pole. In this case, to simulate measurement errors leading to perturbed pole, the perturbed FRFs are determined by modifying ω_r in Eq. (1) by ω'_r. The perturbed eigen frequency is expressed by:

$$\omega'_r = \omega_r(1 \pm 0.01) \tag{3}$$

The results illustrate the comparison of the FRFs contaminated by error added for the pole of subsystem A with the exact FRFs to analyze the effect of the perturbed eigen-frequency on the response of the coupled subsystems. Figure 2 depicts the FRFs of subsystem A and B in the radial direction x.

It appears that shifting pole affects the FRF of the coupled system A (see Fig. 2a). It is observed that the pole shifting decreased the coupled system magnitude. This perturbation affect especially the magnitude of coupling frequency. The pole corresponds to the degree of coupling is the most sensitive to the method of substructuring. It can be verified that the decreasing of magnitude is related to the expression of Eq. (1). The present result shows that the perturbation of pole introduced into the response of subsystem propagated in the FRFs of the coupled subsystem B (Fig. 2b). There is a little difference in the frequency coupling because of the perturbation of the pole. This difference is due to the perturbation in the kernel matrix expression.

3.3 Effect of Perturbed FRF on Coupled System Response

To investigate the sensitivity of the coupling method to the perturbed FRFs, the FRFs of subsystem A are perturbed and this effects on the subsystem B FRFs is discussed. To simulate the effect of noise on the FRFs of the coupled system, a stochastic perturbation is added to the exact FRF:

$$H'_{jk}(\omega) = H_{jk}(\omega) + m_{ij} + jn_{ij} \tag{4}$$

where the Gaussian distributed random variables denote by m_{ij} and n_{ij} with zero mean and a disturbance percentage of 1%. The errors in FRFs results become more
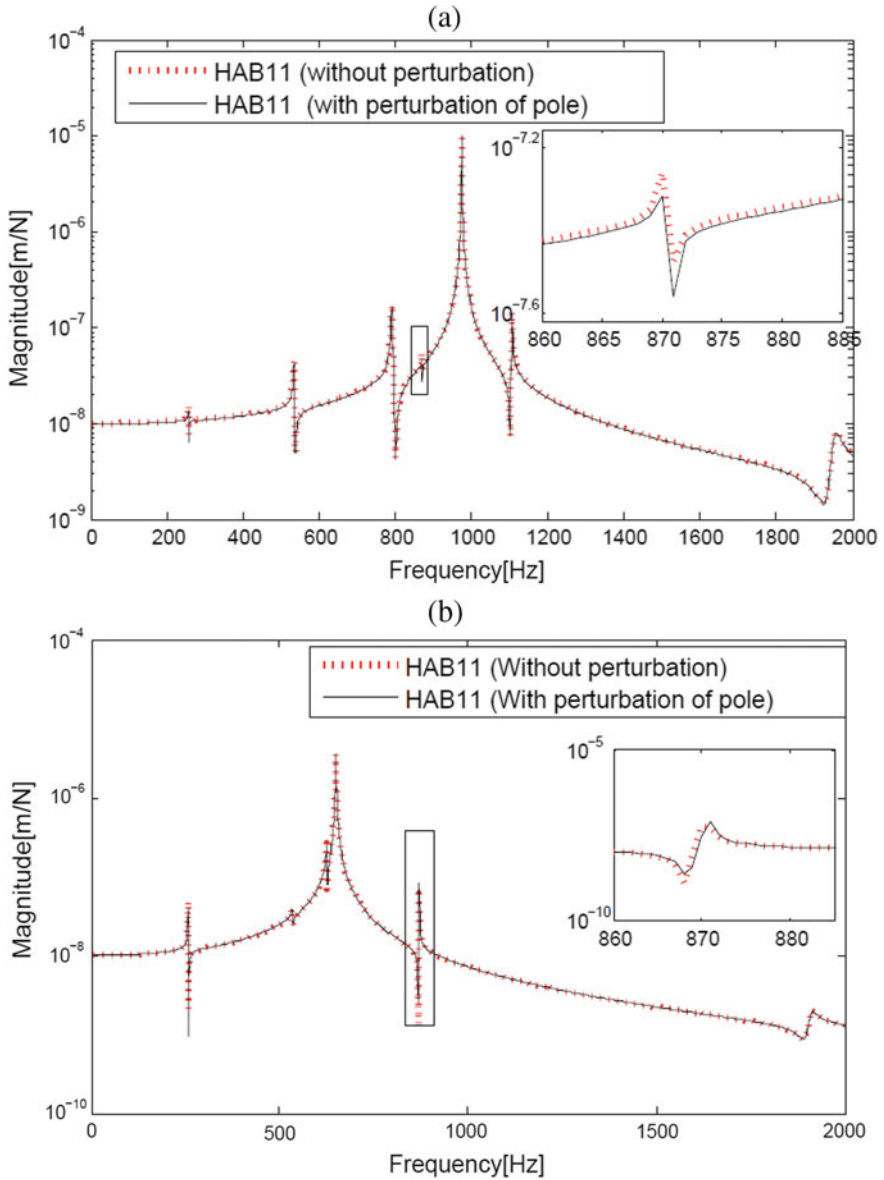
Fig. 2 Influence of shifting pole on the FRFs of subsystems in the radial direction x (H11): a Subsystem A FRF. b Subsystem B FRF

significant when the levels of noise are increased, and this is a predictable conse-
quence. Figure 3 shows the effect of perturbed FRFs on subsystem FRFs in the radial
direction of coupled system. New peaks in the band frequency appears in Fig. 3.
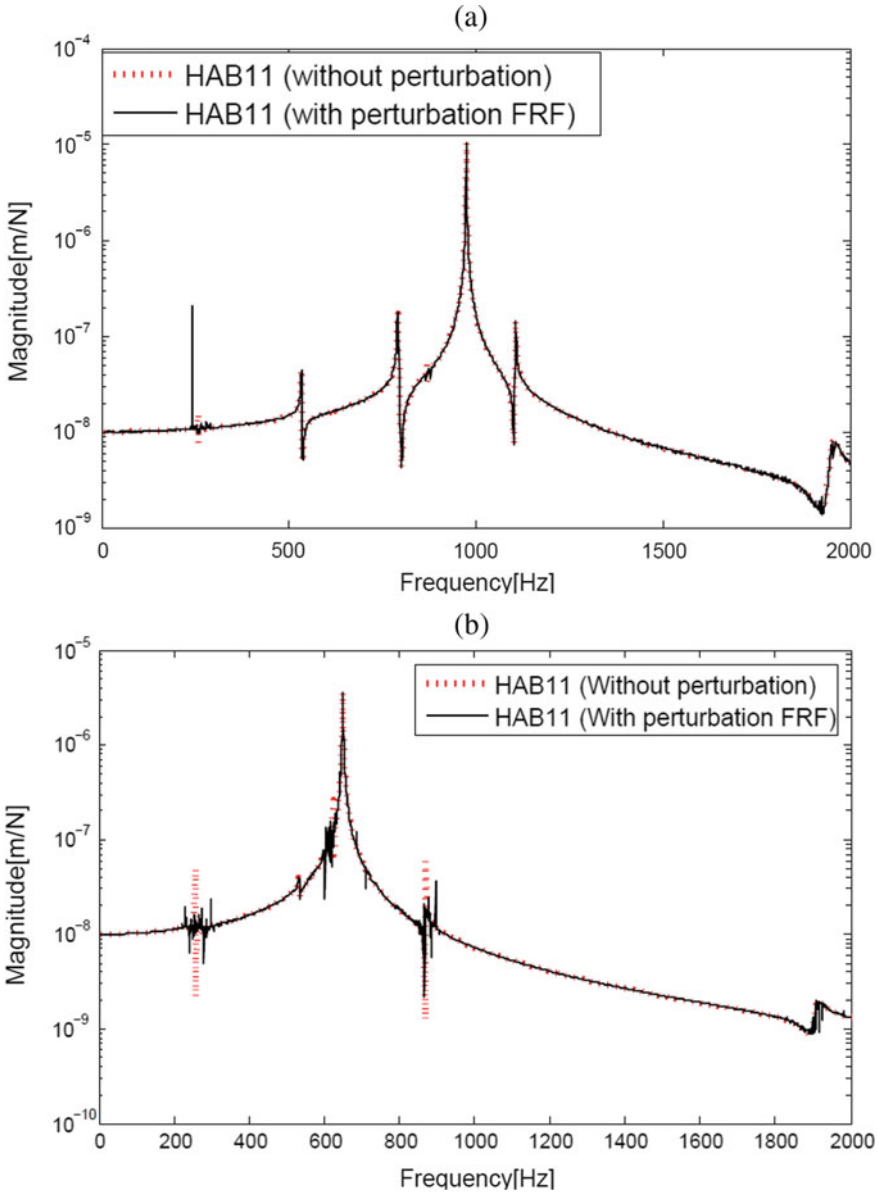
Fig. 3 Influence of subsystem disturbance FRFs on FRFs of subsystems in the radial direction x:
a Subsystem A FRFs. **b** Subsystem B FRFs

It is noted that this disturbance affects especially the coupling frequency. It can be noted that the disturbance FRFs from subsystem A show a certain level of noise, whereas, it has little influence on the FRFs of subsystems B. Moreover, it is observed that FRFs are severely modified because of this type of noise. The FRFs at anti resonances are more sensitive and severely affected by the perturbed FRF for the reason that FRFs at anti-resonances are relatively small. The measurements with offset connection DOFs are reasonably a serious problem.

It is noted that FRFs in the radial direction are less noisy than FRFs in the rotational direction because of rotational coupling.

4   Conclusion

The substructuring approach was applied to transmission system, which is the double reducer stage. The FRF based sub-structuring was presented to determine the dynamic vibration of complex system. The effect of perturbation FRF on the substructuring method is investigated. The results simulation also show that the disturbance of the subsystem FRFs can influence the subsystem coupling FRFs. It is observed that the influence of noise present a false peaks on the coupling FRFs. The perturbed FRF subsystem A can influence the FRF of neighbor subsystem. It is shown that the disturbance of FRFs subsystems can significantly influence the coupled system.

The singular decomposition values (SVD) will be the subject of the future work to examine this noise.

References

Bishop RED, Johnson DC (1960) The mechanics of vibration. Cambridge University Press, Cambridge

D'Ambrogio W, Fregolent A (2010) The role of interface DoFs in decoupling of substructures based on the dual domain decomposition. Mech Syst Signal Process 24(7):2035–2048

Jetmundsen B, Bielawa RL, Flannelly WG (1988) Generalized frequency domain substructure synthesis. J Am Helicopter Society 33(1):55–64

Liu W, Ewins D (2002) Substructure synthesis via elastic media. J Sound Vib 257(2):361–379

Urgueira APV (1989) Dynamic analysis of coupled structures using experimental data. Ph.D. thesis, University of London

Wenjie L (2000) Structural dynamic analysis and testing of coupled structures. Dissertation, Ph.D. thesis, University of London, London, London

Xiuchang H, Hongxing H, Feng C, Shiyin X (2013) Uncertainty propagation in floating raft system by FRF-based substructuring method for elastic coupling. In: Topics in model validation and uncertainty quantification, vol 5. Springer, Heidelberg, pp 165–173